

**ANALYSIS ON APPLICATION OF BIOCHAR COMPOSITES IN  
REMOVAL OF HEXAVALENT CHROMIUM FROM WASTEWATER**

**ANG ZI YING**

**A project report submitted in partial fulfilment of the  
requirements for the award of Bachelor of Engineering  
(Honours) Chemical Engineering**

**Lee Kong Chian Faculty of Engineering and Science  
Universiti Tunku Abdul Rahman**

**April 2020**

**DECLARATION**

I hereby declare that this project report is based on my original work except for citations and quotations which have been duly acknowledged. I also declare that it has not been previously and concurrently submitted for any other degree or award at UTAR or other institutions.

Signature :  \_\_\_\_\_

Name : Ang Zi Ying \_\_\_\_\_

ID No. : 1503644 \_\_\_\_\_

Date : 12.05.2020 \_\_\_\_\_

**APPROVAL FOR SUBMISSION**

I certify that this project report entitled “**ANALYSIS ON APPLICATION OF BIOCHAR COMPOSITES IN REMOVAL OF HEXAVALENT CHROMIUM FROM WASTEWATER**” was prepared by **ANG ZI YING** has met the required standard for submission in partial fulfilment of the requirements for the award of Bachelor of Engineering (Honours) Chemical Engineering at Universiti Tunku Abdul Rahman.

Approved by,

Signature

:



DR. STEVEN LIM  
ASSISTANT PROFESSOR  
LEE KONG CHIAN FACULTY OF ENGINEERING AND SCIENCE  
UNIVERSITI TUNKU ABDUL RAHMAN

Supervisor

:

Dr Steven Lim

---

Date

:

15.5.2020

---

The copyright of this report belongs to the author under the terms of the copyright Act 1987 as qualified by Intellectual Property Policy of Universiti Tunku Abdul Rahman. Due acknowledgement shall always be made of the use of any material contained in, or derived from, this report.

© 2019, Ang Zi Ying. All right reserved.

## ACKNOWLEDGEMENTS

I would like to thank any individuals who had provided assistance and support to me throughout this research. First and foremost, I would like to express my sincere gratitude and appreciation to my research supervisor, Dr Steven Lim for his advice, guidance and enormous patience, leading me to the successful completion of this project.

Next, I would also like to convey my heartfelt appreciation to my loving family and friends who had given me constant moral support and encouragement throughout this period. I would also like to extend special thanks to my course mates who had provided useful suggestions and information for me to complete my project.

## ABSTRACT

Cr(VI) contamination in wastewater is an important environmental issue to be considered with human health concern. Currently, biochar as a green and sustainable organic matter are frequently studied on its application to environmental remediation especially wastewater treatment. Experiments were conducted on biochar composites that were incorporated with various active components to improve the performance of pristine biochar. In the present study, performances of several biochar composites on Cr(VI) removal from aqueous solution were evaluated with the analysis of multiple journals. The foreign materials available for synthesis of biochar composites were categorized as carbonaceous material, nano-zerovalent iron (nZVI), metal/ metal oxide nanoparticles and polymer. Biochar composites were synthesised by either pre- or post-pyrolysis of pristine biochar treated with respective active components. The results of characterization techniques included Electron Microscope, Multipoint N<sub>2</sub>-BET Adsorption Method, Fourier Transform Infrared Spectroscopy (FTIR) and X-Ray Diffraction (XRD) of biochar composites were discussed and analysed. Results showed the successful attachment of the active components on pristine biochar with the presence of additional functional groups or the foreign materials observed on biochar surface. The mechanisms and kinetics models related to Cr(VI) removal were also discussed. Incorporation of foreign components enhanced the removal of Cr(VI) with additional surface functional groups or elements in biochar composites to react with Cr(VI). In the view of the kinetics data, pseudo-second order kinetic and Langmuir isotherm showed higher level of correlation coefficients ( $R^2$ ) where they were best fitted to describe Cr(VI) adsorption, indicated that monolayer chemisorption of Cr(VI) on homogeneous distributed active sites were significant. Based on the results of parameter study, adsorption, reduction and precipitation processes for enhanced Cr(VI) removal were affected by pH, residence time, initial Cr concentration and adsorbent dosage while pH of solution possessed greater impact on adsorption of Cr(VI). PEI/ biochar composite showed highest maximum adsorption capacity at pH 6.8 with adsorbent dosage of 1g/L and initial Cr(VI) concentration of 100 mg/L.

## TABLE OF CONTENTS

<b>DECLARATION</b>		<b>i</b>
<b>APPROVAL FOR SUBMISSION</b>		<b>ii</b>
<b>ACKNOWLEDGEMENTS</b>		<b>iv</b>
<b>ABSTRACT</b>		<b>v</b>
<b>TABLE OF CONTENTS</b>		<b>vi</b>
<b>LIST OF TABLES</b>		<b>ix</b>
<b>LIST OF FIGURES</b>		<b>xi</b>
<b>LIST OF SYMBOLS / ABBREVIATIONS</b>		<b>xiv</b>
<b>CHAPTER</b>		
<b>1</b>	<b>INTRODUCTION</b>	<b>1</b>
1.1	Biochar	1
1.2	Chromium in Wastewater	4
1.3	Problem Statement	8
1.4	Aim and Objectives	9
1.5	Scope and Limitations of the Study	9
1.6	Contribution of the Study	9
1.7	Outline of the Report	10
<b>2</b>	<b>LITERATURE REVIEW</b>	<b>11</b>
2.1	Feedstocks of Biochar	11
2.1.1	Biomass	11
2.2	Application of Biochar in Heavy Metal Removal	13
2.3	Removal Mechanisms of Cr(VI)	15
2.3.1	Adsorption	15
2.3.2	Chemical Reduction and Precipitation	21
2.3.3	Ion Exchange	21
2.4	Factors Affecting Removal Efficiency of Cr(VI)	22
2.4.1	Pyrolysis Temperature	22
2.4.2	pH	24

2.4.3	Residence Time	26
2.4.4	Initial Chromium Concentration	27
2.4.5	Amount of Adsorbent	29
2.5	Modifications on Biochar	30
2.5.1	Carbonaceous Materials	30
2.5.2	Nano-zerovalent Iron	32
2.5.3	Metal or Metal Oxide Nanoparticles	34
2.5.4	Polymers	36
<b>3</b>	<b>METHODOLOGY</b>	<b>39</b>
3.1	Synthesis of Biochar	39
3.1.1	Pyrolysis	39
3.1.2	Gasification	41
3.1.3	Hydrothermal Carbonization	43
3.1.4	Microwave Heating	46
3.2	Synthesis of Biochar Composites	48
3.2.1	Carbonaceous Material/ Biochar Composites	48
3.2.2	Nano-zerovalent Iron/ Biochar Composites	49
3.2.3	Metal or Metal Oxide Nanoparticles/ Biochar Composites	51
3.2.4	Polymer/ Biochar Composites	53
3.3	Experiments for Cr(VI) Removal	54
<b>4</b>	<b>RESULTS AND DISCUSSION</b>	<b>56</b>
4.1	Characterization of Biochar Composites	56
4.1.1	Electron Microscope	56
4.1.2	Multipoint N <sub>2</sub> -BET Adsorption Method	60
4.1.3	Fourier Transform Infrared Spectroscopy (FTIR)	62
4.1.4	X-Ray Diffraction (XRD) & X-Ray Photoelectron Spectroscopy (XPS)	67
4.2	Effects on Cr(VI) Removal	72
4.2.1	Mechanisms and Kinetics Study	72
4.2.2	Parameters Study	77

4.3	Regeneration Study	83
<b>5</b>	<b>CONCLUSIONS AND RECOMMENDATIONS</b>	<b>86</b>
5.1	Conclusions	86
5.2	Recommendations for Future Work	87
	<b>REFERENCES</b>	<b>88</b>

## LIST OF TABLES

Table 1.1:	Chromium Oxidation States and Its Compounds (Thakur, et al., n.d.)	5
Table 1.2:	Water Quality Standards (Water Environment Partnership in Asia, 2013)	6
Table 2.1:	Effect of pyrolysis temperature on elemental composition of biochar produced from different lignocellulosic biomass (Rangabhashiyam and Balasubramanian, 2019)	12
Table 2.2:	Characteristics of biochar based on different raw materials (Ippolito, et al., 2015)	13
Table 2.3:	Removal of heavy metals from water and wastewater by biochar (Wang and Wang, 2019)	15
Table 2.4:	N <sub>2</sub> physical adsorption characteristics of biochar at different carbonization temperatures (Yu, et al., 2018)	24
Table 3.1:	Average pH, surface area and cation exchange capacity (CEC) based on pyrolysis type and temperature (Ippolito, et al., 2015).	41
Table 3.2:	Elemental composition of biochar produced from canola meal via gasification process (Azargohar, et al., 2019).	43
Table 3.3:	Surface area and porosity of hydrochar and pyrolysis biochar produced from manure waste (Aguiar, et al., 2019).	44
Table 3.4:	Proximate and elemental analysis of hydrochar and pyrolysis biochar with rice husk as a raw material (Jian, et al., 2018).	45
Table 3.5:	Elemental composition, ash and biochar yield produced by microwave pyrolysis and conventional pyrolysis under different operating condition (Haeldermans, et al., 2019).	47
Table 4.1:	Specific surface area and pore volume of various biochar composites	61
Table 4.2:	Maximum adsorption capacity of biochar composites with different operating conditions	79

Table 4.3: Regeneration study carried out on biochar composites

85

## LIST OF FIGURES

Figure 1.1:	‘Terra Preta’ (left) and Oxisol (right) Sites (Glaser, et al., 2001)	2
Figure 1.2:	Annual biomass availability in Malaysia (Chan, et al., 2019)	2
Figure 1.3:	U.S. biochar market demand in kilotons by technology in 2014-2025 (Grand View Research, 2019)	4
Figure 1.4:	Spatial distribution of heavy metals in marine water along the Straits of Malacca (Ismail, et al., 2016)	7
Figure 2.1:	Adsorption mechanisms of Cr(VI) (Reyes, et al., 2019)	17
Figure 2.2:	Linear plot of adsorption kinetics for chromium removal based on different kinetic models (A) Pseudo-second order kinetic, (B) Pseudo-first order kinetic and (C) Intra-particle diffusion models (Zhu, et al., 2016)	19
Figure 2.3:	Two-parameter isotherm models studied by Cr(VI) adsorption on Eucalyptus globulus bark biochar at 323K (Choudhary and Paul, 2018)	20
Figure 2.4:	Effect of carbonization temperature of biochar on Cr(VI) removal (Yu, et al., 2018)	23
Figure 2.5:	Cr(VI) species distribution with increasing pH values (Zhang, et al., 2018)	26
Figure 2.6:	Effects of pH values on Cr(VI) removal (Zhang, et al., 2018)	26
Figure 2.7:	Effect of residence time on Cr(VI) adsorption (Yu, et al., 2018)	27
Figure 2.8:	Effect of initial concentration of Cr(VI) on Cr(VI) (A) removal efficiency and (B) removal capacity (Gao, et al., 2018)	28
Figure 2.9:	Effect of biochar dosage on removal of Cr(VI) (Choudhary and Paul, 2018)	29
Figure 2.10:	Formation of single-walled carbon nanotube (SWCNT) from graphene sheet (Sarkar, et al., 2018)	31

Figure 2.11:	Structures of g-C <sub>3</sub> N <sub>4</sub> with circled characteristic intrinsic vacancies surrounded by nitrogen atoms (Inagaki, et al., 2019)	31
Figure 4.1:	FESEM images of CNT/ activated carbon with magnification of (A) 40000x and (B) 140000x (Atieh, 2011)	57
Figure 4.2:	FESEM images of (A) g-C <sub>3</sub> N <sub>4</sub> and (B) g-C <sub>3</sub> N <sub>4</sub> nanosheets/ biochar (Li, et al., 2019)	57
Figure 4.3:	SEM-EDS images and spectra of (A) nZVI/ biochar and (B) nZVI/ biochar/ CA (Wan, et al., 2019)	58
Figure 4.4:	SEM images with magnification of 50000x of (A) S-nZVI and (B) S-nZVI/ biochar (Gao, et al., 2018)	59
Figure 4.5:	SEM images of PPy/ biochar with magnification of (A) 500x and (B) 10000x (Yang, et al., 2018)	60
Figure 4.6:	Raman spectra of CNT/ biochar composites and (Inyang, et al., 2014)	64
Figure 4.7:	FTIR spectra of g-C <sub>3</sub> N <sub>4</sub> / biochar composites (Li, et al., 2019)	64
Figure 4.8:	(A) FTIR spectra and (B) Raman spectra of nZVI/ biochar composites (Wan, et al., 2019)	65
Figure 4.9:	FTIR spectra of (A) CMC-nZVI/ biochar composites and (B) nZVI/ Si-rich biochar composites (Zhang, et al., 2019; Qian, et al., 2019)	66
Figure 4.10:	FTIR spectra of ZnO/ biochar composites (Yu, et al., 2018)	66
Figure 4.11:	FTIR spectra of PPy/ magnetic biochar composites (Yang, et al., 2018)	67
Figure 4.12:	XRD patterns of g-C <sub>3</sub> N <sub>4</sub> / biochar composites (Li, et al., 2019)	69
Figure 4.13:	XRD patterns of CA-nZVI/ biochar composite (Wan, et al., 2019)	69
Figure 4.14:	XRD pattern of CMC-nZVI/ biochar composites (Zhang, et al., 2019)	69
Figure 4.15:	XRD patterns of nZVI/ Si-rich biochar composites (Qian, et al., 2019)	70

Figure 4.16:	XRD patterns of S-nZVI/ biochar composites (Gao, et al., 2018)	70
Figure 4.17:	XRD patterns of ZnO/ biochar composites (Yu, et al., 2018)	70
Figure 4.18:	XRD patterns of $\alpha$ -Fe <sub>2</sub> O <sub>3</sub> / biochar composite (Liu, et al., 2019)	71
Figure 4.19:	XRD patterns of FeS/ biochar composites (Lyu, et al., 2017)	71
Figure 4.20:	XRD patterns of (A) magnetic biochar and (B) PPy/ magnetic biochar (Thines et al., 2017)	71
Figure 4.21:	The effect of (A) initial pH and (B) constant reaction pH on removal of Cr(VI) by CMC-nZVI/ biochar (Zhang, et al., 2019)	81
Figure 4.22:	Concentration of Cr species and dissolved ion during reaction by CMC-nZVI/ biochar (Zhang, et al., 2019)	82
Figure 4.23:	Regeneration tests carried out on Fe <sub>3</sub> O <sub>4</sub> / biochar composite and pure Fe <sub>3</sub> O <sub>4</sub> (Wang, et al., 2019)	84

**LIST OF SYMBOLS / ABBREVIATIONS**

AVP	average pore sizes
CB	conduction band
CEC	cation exchange capacity
COD	chemical oxygen demand
EDS	energy dispersive system
FESEM	field emission scanning electron microscopy
FTIR	Fourier transform infrared
ICP-AES	inductively coupled plasma-atomic emission spectrometer
$K_D$	coefficient of distribution
MVP	microwave-assisted pyrolysis
MVA	microwave absorber
$O_i$	oxygen interstices
PFO	pseudo-first order
$pH_{pzc}$	point of zero charge
PSO	pseudo-second order
$R^2$	correlation coefficient
SEM	scanning electron microscopy
TGA	thermogravimetric analysis
XPS	X-ray photoelectron spectroscopy
XRD	X-ray diffraction
UV	ultraviolet
VB	valence band
Vis	visible
$V_o$	oxygen vacancies
$V_{tot}$	total pore volumes
$V_{Zn}$	zinc vacancies
$Zn_i$	zinc interstices
C	carbon
CA	calcium alginate
Cd	cadmium
CMC	carboxymethyl cellulose

CNT	carbon nanotube
Cr	chromium
Cr(III)	trivalent chromium
Cr(VI)	hexavalent chromium
Cr <sub>2</sub> O <sub>3</sub>	chromium (III) oxide
Cr(OH) <sub>3</sub>	chromium (III) hydroxide
Cr <sub>2</sub> S <sub>3</sub>	chromium (III) sulfide
CTAB	cetyl trimethyl ammonium bromide
Cu	copper
Fe	iron
FeCl <sub>3</sub>	iron (III) chloride
FeCr <sub>2</sub> O <sub>4</sub>	chromite
Fe(NO <sub>3</sub> ) <sub>3</sub>	iron (III) nitrate
Fe <sub>2</sub> O <sub>3</sub>	iron (III) oxide
$\alpha$ -Fe <sub>2</sub> O <sub>3</sub>	hematite
Fe <sub>3</sub> O <sub>4</sub>	iron (II,III) oxide, magnetite
Fe(OH) <sub>3</sub>	ferric hydroxide
FeS	iron monosulfide
FeS <sub>2</sub>	iron disulfide
FeSO <sub>4</sub> ·7H <sub>2</sub> O	iron sulfate heptahydrate
g-C <sub>3</sub> N <sub>4</sub>	graphitic carbon nitride
H	hydrogen
H <sub>2</sub> C <sub>2</sub> O <sub>4</sub>	oxalic acid
HCl	hydrochloric acid
Hg	mercury
HNO <sub>3</sub>	nitric acid
H <sub>2</sub> SO <sub>4</sub>	sulfuric acid
K <sub>2</sub> Cr <sub>2</sub> O <sub>7</sub>	potassium dichromate
KOH	sodium hydroxide
MgCl <sub>2</sub> ·6H <sub>2</sub> O	magnesium chloride hexahydrate
MgO	magnesium oxide
Mg(OC <sub>2</sub> H <sub>5</sub> ) <sub>2</sub>	magnesium ethoxide
Mg(OH) <sub>2</sub>	magnesium hydroxide
N	nitrogen

NaOH	sodium hydroxide
Na <sub>2</sub> S.9H <sub>2</sub> O	aqueous sodium sulfide
Na <sub>2</sub> SO <sub>4</sub>	sodium sulfate
NaBH <sub>4</sub>	sodium borohydride
nZVI	nano-zerovalent iron
O	oxygen
PAHs	polycyclic aromatic hydrocarbons
Pd	lead
PEI	polyethylenimine
PPy	polypyrrole
Py	pyrrole
S	sulfide
Si	silicon
SiO <sub>2</sub>	silicon oxide
ZnCl <sub>2</sub>	zinc chloride
Zn <sub>2</sub> CrO <sub>5</sub> .H <sub>2</sub> O	zinc chromium oxide hydrate
Zn(NO <sub>3</sub> ) <sub>2</sub> .H <sub>2</sub> O	zinc nitrate hexahydrate
ZnO	zinc oxide

## CHAPTER 1

### INTRODUCTION

#### 1.1 Biochar

Biochar is one form of charcoal as combustible solid rich in carbon which is produced from biomass by thermochemical process with either limited oxygen available or total absence of oxygen. It can be produced by pyrolysis, gasification and hydrothermal carbonization processes, but optimum production of biochar can only be obtained from slow pyrolysis with lower emission of harmful gases (Elkhalifa, et al., 2019). Biochar is usually derived from biomass of sustainable sources with its widespread environmental applications especially in agriculture sector (Hagemann, et al., 2018). It is considered 'green' and low cost in the aspect of organic wastes as feedstocks and the production techniques used. Biomass is a renewable resource consists of organic matter such as wood or crop residues. Thus, it can be an effective way to manage the agricultural wastes sustainably by utilizing it as the feedstock for biochar in various applications.

The concept of biochar was inspired by the dark earth known as 'Terra Preta', discovered by James Orton in 1870 which was found in the Amazon River basin (Wayne, 2012). 'Terra Preta' soils were black and very fertile as shown in Figure 1.1, containing large amounts of nutrients and organic matters with black carbon of 70 times greater than surrounding soils persistent in the environment (Glaser, et al., 2001). The fertility of the soil was anthropogenic in nature which mainly attributed to charred biomass. Its regeneration capacity with the ability to maintain the positive properties for a long time has high potential for sustainable agricultural development (Bis, et al., 2018). Meanwhile, biochar was considered to be the primary component of the soil with similar properties.

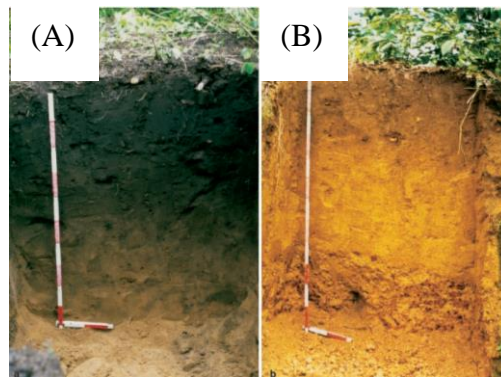


Figure 1.1: (A) 'Terra Preta' and (B) Oxisol Sites (Glaser, et al., 2001)

Biomass as the raw material in biochar production was the world's fourth largest energy sources with annual production of 220 billion oven-dry tons globally. The agricultural wastes like corn stover and wheat straw were produced in huge amounts as compared to the other available lignocellulosic biomass. The abundance and availability of agricultural wastes enabled them to be a superior source of biochar (Mary, et al., 2016). The favourable climate in Malaysia with the availability of tropical forests encouraged the agricultural activities and wood industries which contribute to large amount of waste generation. It can be observed from Figure 1.2 that most of the biomass wastes came from the palm oil trees which was found abundantly in Malaysia and palm biomass production was increasing throughout the past 10 years (Chan, et al., 2019). Therefore, there were adequate sustainable sources available for the preparation of biochar to aid in waste management and provide cheaper cost of raw materials.

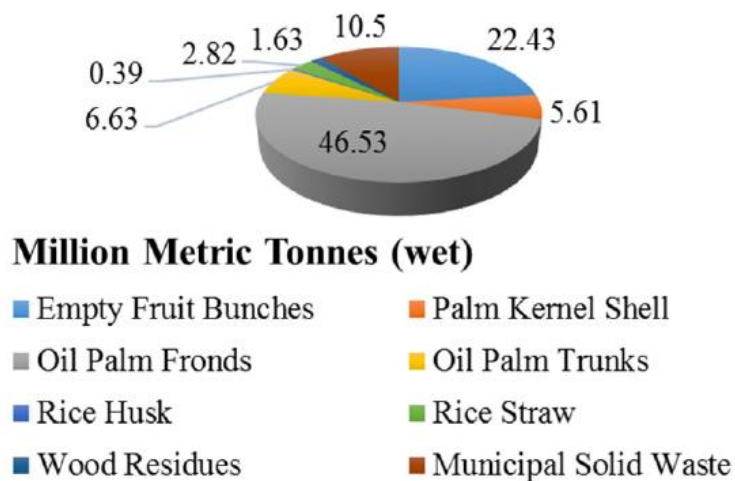


Figure 1.2: Annual biomass availability in Malaysia (Chan, et al., 2019)

The physicochemical properties of biochar are dependent on its wide variety of raw materials and pyrolysis temperature during the production process. Loss of volatile compounds from biomass allows biochar to have high porosity and surface area with lower density. The porosity of biochar mostly consists of micropores structure while porous structures contribute to greater water holding capacity. Biochar poses the ability for electromagnetic conductivity by the formation of conjugated double bonds with shared electrons. Generally, biochar has considerably high alkalinity and ability of pH buffering with the formation of functional groups upon the recipient of proton ( $H^+$ ) by unpair negative charges such as carboxyl  $-COOH$ , carbonyl  $-C=O$ , hydroxyl  $-OH$  and ester  $-COO$  groups. Therefore, it has higher capacity on cation exchange (Weber and Quicker, 2018).

Biochar was commonly known with its implementation in soil amendment, carbon sequestration and combating climate change with its high resistivity to biodegradation. The alkalinity of biochar was used to neutralize the acidified soil which is incompatible for the growth of plants in agriculture. High porosity of biochar reduced bulk density and increased soil aggregation for better retention of water and nutrients. It also helped in removal of various soil pollutants including both organic and inorganic matters with its sorption capacity (Yu, et al., 2019).  $CO_2$  adsorption was done by van der waals forces of attraction in combination of the carbamate and ammonia pairs formed by the reaction with two amine groups of biochar (Jung, Park and Kwon, 2019). Subsequent carbon capture and storage reduced the level of carbon dioxide which was the most abundant greenhouse gases which contributes to the climate change. Other than that, biochar was also used as a biorefinery catalyst for biodiesel and bio-sugar production and the processes of catalytic pyrolysis, gasification, hydrolysis, esterification and transesterification of lipids (Lee, et al., 2019).

Similar to the remediation of contaminated soil, biochar had also been applied in water and waste water decontamination. It was competitive with the commercial activated carbon which was normally used in water treatment where it provided greater adsorption capacity at high initial concentrations of COD (1200mg/L),  $PO_4^{3-}$  (18mg/L),  $NH_4^+$  (50mg/L) and lower adsorption capacity at lower concentrations of  $PO_4^{3-}$  (5mg/L) and  $NH_4^+$  (10mg/L) in batch

experiments. Their adsorption capacity was similar in the studies of packed bed column with higher removal rate by biochar at total COD above 500mg/L (Wang and Wang, 2019). However, the efficiency of removal of biochar was limited by the weak deposition of reactive materials and the reducing potential (Wan, et al., 2019).

The global market size of biochar was worth USD 1.3 billion in 2018 with the demand of 395.3 kilotons. The market demand of biochar was expected to grow continuously from 2019 to the year of 2025 as shown in Figure 1.3. It was owing to the increase of environmental awareness, low cost of production and government policies established for regulation of waste management. The application of biochar in wastewater treatment and other potential usages such as the manufacturing of building materials, fabric additive in textile industry and shielding of electromagnetic radiation in electronic industry are important in driving the biochar market growth at the future (Grand View Research, 2019).

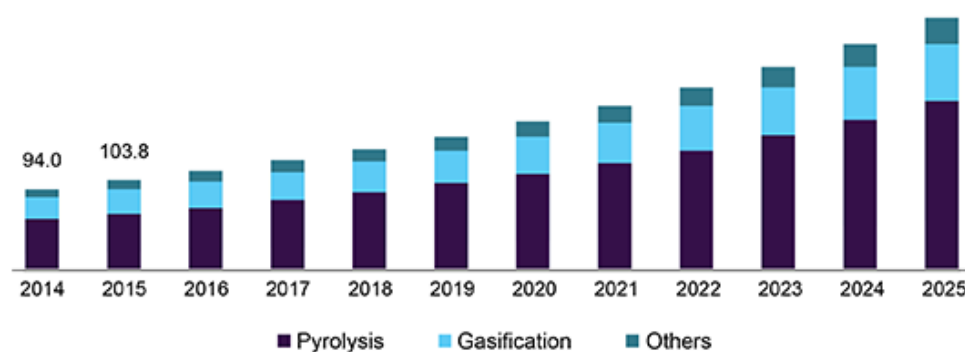


Figure 1.3: U.S. biochar market demand in kilotons by technology in 2014-2025 (Grand View Research, 2019)

## 1.2 Chromium in Wastewater

Chromium, Cr is a tasteless and odourless transition metal classified as an environmental contaminant due to its toxicity and potential adverse effects of exposure. It was found in the environment either as a naturally occurring element or released by natural processes and human activities. Natural sources of Cr included the processes of rocks weathering, soil erosion and rainwater leaching while trace amounts are found in food. It was widely used in industrial applications with its extensive hardness, chemical, electrical and corrosion

resistance for the production of alloy, leather, pigments and electroplating (Almeida, et al., 2019). Cr was then released into the environment through atmospheric emission or wastewater discharged from industrial sources.

There are seven oxidation states of Cr exist in the form of different compounds as shown in Table 1.1. The compounds in the oxidation states of 0, +1, +4 and +5 are rare and unstable while +2 compounds are more common compared to them. Nevertheless, Cr usually appears in the forms of trivalent, Cr(III) and hexavalent chromium, Cr(VI) found in the environment. Cr(III) is an essential nutrient to human for fat, glucose and protein metabolism with the daily intake of 50-200  $\mu\text{g/d}$  (Environmental Protection Agency, 2016). Compounds of Cr(III) are commonly insoluble in aqueous solution where it can be precipitated out from water easily such as  $\text{Cr(OH)}_3$  (Almeida, et al., 2019).

Table 1.1: Chromium Oxidation States and Its Compounds (Thakur, et al., n.d.)

Oxidation States	Compounds
0	$\text{Cr(CO)}_6$ , $\text{Cr(C}_6\text{H}_6)_2$
+1	$\text{K}_3(\text{Cr(CN)}_5\text{NO})$
+2	$\text{CrCl}_2$ , $\text{Cr(CH}_3\text{COO)}_4$ , $\text{CrO}$ , $\text{CrSO}_4$
+3	$\text{CrCl}_3$ , $\text{Cr}_2\text{O}_3$ , $\text{Cr}_2(\text{SO}_4)_3$
+4	$\text{K}_2\text{CrF}_6$ , $\text{CrO}_2$
+5	$\text{K}_3(\text{Cr(O}_2)_4)$ , $\text{CrF}_5$
+6	$\text{K}_2\text{Cr}_2\text{O}_7$ , $\text{K}_2\text{CrO}_4$ , $\text{CrO}_3$

The toxicity of chromium is primarily attributed to the Cr(IV) which is toxic and carcinogenic. It was mainly formed by anthropogenic sources from various industrial uses. The compounds of Cr(VI) are strong oxidizing agents and appeared to be corrosive and irritating. Cr metal can enter human body through ingestion, inhalation and dermal absorption whereby Cr(IV) can be readily absorbed by human respiratory tract and skin compared to Cr(III) which is poorly absorbed by any mechanisms (Agency for Toxic Substances and Disease Registry, 2008). In addition, Cr(VI) compounds are highly mobile and soluble in wide range of pH where specific treatment will be required for its removal from water (Almeida, et al., 2019).

As a strong oxidizing agent, Cr(VI) resulted in oxidative stress to cells, leading to DNA damage, gene mutation, abnormalities in chromosome and lethal mutations of animal or human cells (Zhang, et al., 2019). The adverse health effects created by Cr(VI) can be classified into acute and chronic effects depending on the duration of human exposure. Acute effects were mainly occurred by ingestion while chronic effects are usually induced by inhalation or dermal absorption of Cr(VI). Ingestion of Cr(VI) compounds may lead to epigastric pain, vertigo, vomit, diarrhoea, fever, organs failure, coma, death and other illnesses depending on the dosage taken (Agency for Toxic Substances and Disease Registry, 2008). Oral lethal dosage of soluble Cr(VI) compounds was about 50-70 mg/kg human body weight (Zhang, et al., 2019). Prolong inhalation and skin contact to Cr compounds may cause various respiratory and skin diseases such as bronchitis, ulcers, and cancers due to its carcinogenicity (Agency for Toxic Substances and Disease Registry, 2008).

Table 1.2 showed several water quality standards for different sources of water including drinking water, surface water, ground water and wastewater discharged obtained from Water Environment Partnership in Asia. Generally, very low concentration of Cr has to be maintained before it is released to the environment to control the level of human exposure to its toxicity. For drinking water quality, only 0.05 mg/L of Cr is allowed to be consumed by human at safety level.

Table 1.2: Water Quality Standards (Water Environment Partnership in Asia, 2013)

<b>Quality Standards</b>	<b>Concentration (mg/L)</b>
Drinking Water	0.05
Surface Water	0.05
Ground Water	0.05 Cr(VI)
Wastewater Discharge	0.1

The removal of Cr is the focus for the study because Cr is relatively hazardous to human health and higher concentration will lead to severe effects. It is a greater concern to the rural populations which is highly dependent on available surface water for the supply of water. According to Figure 1.4, Cr

concentration was highest among various heavy metals being analysed in the marine water at the states of Perlis, Kedah, Pulau Pinang, Negeri Sembilan and Johor, Malaysia. The concentrations of heavy metals were diluted along the way from point sources to the Straits of Malacca (Ismail, et al., 2016). The main source of surface water contamination attributed to the wastewater discharged from the industrial plants. Therefore, it is important to determine an effective way to control the concentration of Cr in wastewater.

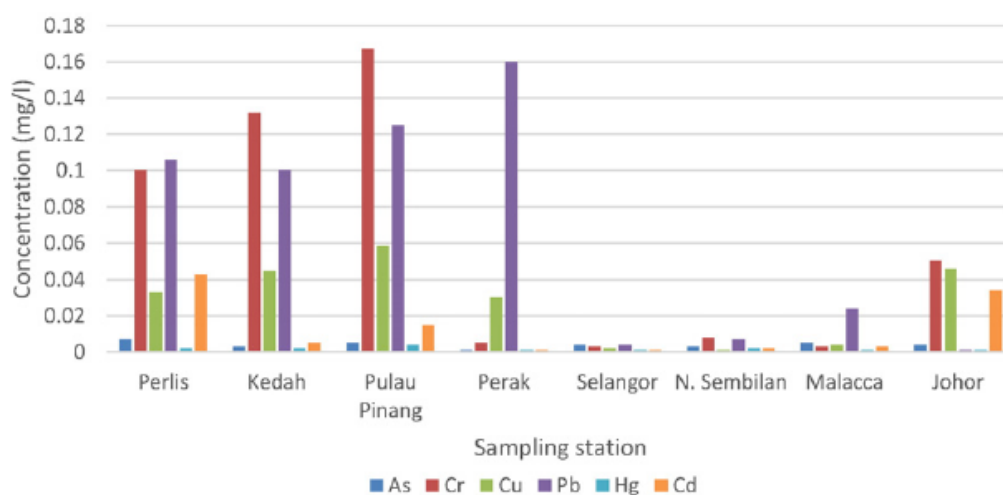


Figure 1.4: Spatial distribution of heavy metals in marine water along the Straits of Malacca (Ismail, et al., 2016)

Several techniques were commonly used for decontamination of Cr(VI) from wastewater like adsorption, membrane filtration, ion exchange and electrochemical treatment. Activated carbon was the most commonly used adsorbent for Cr removal from wastewaters attributed to its high surface area range from 500 to 1500  $m^2/g$ , internal micro-porosity structures and surface functional groups such as carboxylic group (Owlad, et al., 2008). Electrochemical techniques such as electrochemical oxidation, reduction and precipitation involved the process of eliminating or converting the pollutants into less/ non-toxic compounds (Feng, et al., 2016).

### 1.3 Problem Statement

Increasing number of industrial factories had brought to several environmental issues especially water pollution. It was unavoidable for the wastewater to be discharged from various point sources such as factories, hospitals and mining area that seep between the soils, rocks and eventually flow into the water bodies like rivers, lakes and oceans. It resulted in pollution of the surface and ground water which are the primary sources of water supply for industrial, commercial and domestic usage especially drinking water. Wastewater discharged from different industries may contain heavy metals which are persistent contaminants in wastewater with their non-biodegradable and toxicity in nature. High amounts of heavy metals enter the water bodies will give rise to serious health effects and environmental impacts (Akpoy, Ohiobor and Olaolu, 2014).

The Cr(VI) compounds are one of the toxic heavy metals with severe health effects in high concentration. Since Cr(VI) compounds poses significant risks to human health and environment, wastewater must be treated to control its concentration below the water quality standards by using effective methods. The conventional remediation technologies applied in removal of Cr(VI) from wastewater faced various challenges like economical consideration, removal at low concentration, formation of secondary pollution and the duration of treatment. Thus, adsorption process is more advantageous due to its higher removal efficiency, simplicity in operation and feasibility in large-scale remediation (Rangabhashiyam and Balasubramanian, 2019).

Biochar was a considerable cheap and non-toxic adsorbent for efficient adsorption of various contaminants due to its high surface area, porous structure and surface chemical properties. However, modification is required to be done on pristine biochar due to its limitation in reduction potential and lower surface area as compared to activated carbon which was commonly used in wastewater treatment to improve its efficiency in contaminants removal. Recently, many research studies had been carried out on the application of biochar in decontamination of wastewater with different modifications methods. In this case, various biochar composites available for Cr(VI) removal from the wastewater is studied to determine their improvements and effectiveness of removal comparing to pristine biochar.

#### **1.4 Aim and Objectives**

The main aim of the study is to review the application of biochar composites in Cr(VI) removal from wastewater with the following objectives to be achieved:

- i. To analyze the different synthesis pathways of biochar composites for removal of Cr(VI) from wastewater.
- ii. To identify the mechanism and primary factors affecting the application of biochar composites for removal of Cr(VI).
- iii. To compare the effectiveness of different biochar composites applications in the process of Cr(VI) removal.

#### **1.5 Scope and Limitations of the Study**

The scope of the study covers the synthesis process and application of biochar composites to remove Cr(VI) from wastewater. The production methods of biochar and removal mechanism of Cr(VI) by using biochar composites will be identified through literature review. Besides that, the factors affecting the removal efficiency of Cr(VI) by biochar which include pyrolysis temperature, pH of solution, concentration of Cr, amount of sorbent and the contact time will also be discussed.

The types of biochar composites to be included in the study are biochar-supported carbonaceous materials, nano-zerovalent iron, metal or metal oxides and polymers. Their methods of preparation and effects on Cr(VI) removal will be determined by carrying out information collection through journals review.

However, there are several limitations for the study to be considered. This is a review paper where all the information is based on previous research studies conducted and therefore some of the information may not be readily available. There may be some own analysis to be included in the study too.

#### **1.6 Contribution of the Study**

Wide variety of biochar composites were studied to evaluate their application on Cr(VI) removal in wastewater remediation. However, comparison on their removal efficiency was rarely found where proper modification on biochar has to be identified to obtain a powerful and cost-effective adsorbent for Cr(VI) remediation from aqueous solution. In this study, the parameters affecting adsorption capacity of biochar composites were discussed to figure out the

optimum operating condition for effective Cr(VI) removal. Nevertheless, materials incorporated on biochar was classified into carbonaceous materials, nano-zerovalent iron, metal or metal oxides and polymers while their properties affecting the mechanisms and efficiency on removal of Cr(VI) were discussed. Therefore, the practical application of biochar composites to remove Cr(VI) from wastewater can be evaluated.

### **1.7 Outline of the Report**

A general introduction on biochar included its physical and chemical properties, applications and future market demand as well as the negative impacts of Cr(VI) in wastewater are discussed in Chapter 1. In Chapter 2, the sources of biochar feedstocks and its application in heavy metal removal, mechanisms and factors affecting Cr(VI) removal are reviewed together with the categorization of modification on biochar applicable for Cr(VI) remediation. The synthesis methods of biochar and biochar composites and experiments conducted to evaluate the efficiency of biochar composites are discussed in Chapter 3. The results based on different sources are analysed and compared among selected biochar composites in Chapter 4. Conclusion on the research is made and some recommendations are provided in Chapter 5.

## CHAPTER 2

### LITERATURE REVIEW

#### 2.1 Feedstocks of Biochar

There were various kind of feedstocks for biochar synthesis which were generally biomass classified as agricultural or industrial wastes such as rice straw, sugarcane bagasse, wheat straw, sawdust and food wastes. The properties of biochar formed were dependent on the types of feedstocks with different compositions. The study was focused on various waste residues recycled to produce biochar with vary physical and chemical properties.

##### 2.1.1 Biomass

Specific type of biochar can be produced from different types of biomass as the production feedstock. This is because biochar tends to reflect the physical and chemical properties of the sources. Carbon rich material was a good source of biochar where it is mainly composed of carbon residues. There were wide variety of biomass which had been used in synthesizing biochar such as agricultural wastes, industrial by-products, animal wastes and sewage sludge. Examples of biochar feedstocks are wheat straw, rice husk, wood chips, tree bark, sugarcane bagasse, paper sludge and dairy manure. Most of the biomass used were considered as undesired materials which can be reduced by converting them into biochar for other useful applications. Biochar could also be engineered to form a product with selective physical and chemical properties beneficial for its specific application. It was controlled by selecting an appropriate feedstock and operating conditions with varying modification methods (Mylavarapu, Nair and Morgan, 2016).

Raw biomass may contain different compositions of carbon (C), hydrogen (H), nitrogen (N) and oxygen (O) which affect the elemental composition of biochar. Selected elemental composition of biochar from different biomass feedstocks at varying pyrolysis temperatures were shown in Table 2.1. Based on Table 2.1, C% increased with increasing pyrolysis temperature with the formation of more chemically and thermodynamically stable aromatic structure. The reduction of H%, O% and N% indicated the

release of CO<sub>2</sub>, CO, CH<sub>4</sub>, H<sub>2</sub>, H<sub>2</sub>O, NH<sub>3</sub> and N<sub>2</sub> during pyrolysis process while a slight increase in N% was observed by greater removal of other components. The raw biomass composed of higher lignin resulted in higher mass yield of biochar due to higher thermal stability of lignin with large number of functional groups compared to cellulose and hemicellulose (Weber and Quicker, 2018).

Table 2.1: Effect of pyrolysis temperature on elemental composition of biochar produced from different lignocellulosic biomass (Rangabhashiyam and Balasubramanian, 2019)

Type	Temperature (°C)	C (%)	H (%)	N (%)	O (%)
Sawdust	400	71.50	4.70	0.05	23.60
	475	80.40	3.80	0.10	15.70
	550	81.30	3.60	0.20	14.90
Rice straw	400	34.24	3.31	1.50	37.60
	500	47.55	1.23	1.02	34.83
	600	67.34	0.85	0.89	24.17
Sugarcane bagasse	400	55.66	5.44	0.54	28.26
	500	55.12	5.30	0.39	18.78
	600	66.86	5.18	0.47	14.88
Wheat straw	400	70.60	3.50	4.46	15.8
	500	71.50	2.35	4.54	14.6
	600	73.40	1.85	4.62	11.7

In addition, the properties such as pH, surface area and CEC of biochar will also be affected by the source of raw materials and pyrolysis temperature. The characteristics of biochar with several raw materials were observed in Table 2.2. It was observed that biochar produced from harder biomass such as shell and wood had lower pH and higher specific surface area where hazelnut shell resulted in biochar with highest specific surface area with the value of 467.5 m<sup>2</sup>/g. However, the CEC of hazelnut shell biochar was lower while biochar synthesized from corn provided highest CEC with 607 mmol/kg. The pH of biochar was in the range of pH 7.48 – 9.45 which was alkaline and the degree of alkalinity was varied with the types of feedstocks as shown in Table 2.2.

Table 2.2: Characteristics of biochar based on different raw materials (Ippolito, et al., 2015)

<b>Source</b>	<b>pH</b>	<b>Specific Surface Area, <math>m^2/g</math></b>	<b>Cation Exchange Capacity, <math>mmol/kg</math></b>
Corn	9.27	107.2	607
Wheat/ barley	8.80	26.65	103
Rice straw/ husk	9.17	42.15	212
Hazelnut shell	7.86	467.5	83.8
Bagasse	7.59	113.6	115
Food Waste	9.09	0.803	81
Other (green wastes)	8.72	119.8	290
Hardwoods	7.94	171.3	138
Softwoods	7.48	194.2	145
Papermill waste	9.13	10.08	52
Dairy manure	9.45	33.38	342

## 2.2 Application of Biochar in Heavy Metal Removal

Biochar was recognized as a highly efficient adsorbent in removal of various pollutants in the environment which include organic and inorganic contaminants. Several studies had been carried out to determine its applications in the remediation of polluted soil and water. For instance, biochar produced from wheat residues was used to remove benzene and nitrobenzene from wastewater while biochar prepared from green waste and dairy manures removed substantial amounts of atrazine from wastewater (Mylavarapu, Nair and Morgan, 2016). Other than organic contaminants, biochar played an important role in elimination of heavy metal from wastewater and soil. In this case, the application of biochar in heavy metal removal from wastewater is the main focus for the study.

Heavy metals pollution had resulted in adverse impacts to human health which was a great concern for environmental remediation. Generally, the heavy metals like Pb, Hg, Cr, As, Cd, Zn and Cu were commonly found in aqueous environment with maximum allowable limits in drinking water and wastewater

established by Environmental Protection Agency (Premarathna, et al., 2019). In addition to naturally occurring metals in the environment, various anthropogenic activities such as mining, metal smelting and electronic manufacturing discharge further increased the amounts of metals in wastewater discharged to the environment which were then being consumed by human and animals. The common methods used in remediation of metal-polluted wastewater involved electrochemical treatment membrane technologies, chemical precipitation and ion exchange (Li, et al., 2017). In the meanwhile, adsorption was the most cost-effective and environmentally friendly method to remove heavy metals from wastewater whereby biochar was potential to be applied as an effective adsorbent depending on the types of heavy metals and feedstocks (Wang and Wang, 2019). The application of biochar in removal of several metal ions was shown in Table 2.3 where the removal efficiencies were considerably high for most of the metal ions other than arsenic.

Biochar was a good adsorbent for heavy metals attributed to its high specific surface area, porosity and the presence of various surface functional groups such as carboxyl, hydroxyl and phenolic groups to provide greater affinity for heavy metals. The surface functional groups of biochar contributed to the CEC for immobilization of metal ions. The mechanisms of metal sorption by biochar involved electrostatic interactions, cation exchange, metal complexation, metal precipitation and reduction of metal species followed by adsorption of the reduced species (Li, et al., 2017). These were the interactions between metal and the species or functional groups present on the surface of biochar.

However, the adsorption capacity of pristine biochar on metal ions was lower than commercial activated carbon, for examples 2.4-147 mg/g and 0.3-39.1 mg/g for Pb and Cd as compared to 255 mg/g and 91.4 mg/g by activated carbon. Thus, the adsorption capacity on metal could be enhanced by modifying biochar which included the loading of nanoparticles, organic functional groups, reductants and minerals or activation by alkali and acid solutions (Li, et al., 2017). Modification of biochar tends to increase the adsorption sites with greater affinity to particular metal ions where the types of modification dependent on the metals to be removed.

Table 2.3: Removal of heavy metals from water and wastewater by biochar (Wang and Wang, 2019)

Heavy Metals	Initial Concentration (mg/L)	Feedstock	Pyrolysis Temperature (°C)	Applied Dose (g/L)	Removal Efficiency (%)
Cd <sup>2+</sup>	20	Rape straw	600	1.25	100
	20	Corn straw	400	20	99.24
	30	Hickory wood	600	2	95.9
Pb <sup>2+</sup>	150	Sawdust	400	0.4	100
	400	Celery	500	5	97.7
	6-233	Bagasse	~500	1	~80
Cu <sup>2+</sup>	10	Macroalga	500	0.1	~80
	50	Spartina alterniflora	400	10	100
As <sup>5+</sup>	50	Pinewood	600	2.5	~35
	0.09	Sewage sludge	300	4	53
Cr <sup>6+</sup>	200	Peanut hull	450-650	2	10-70
	100	Rice husk	450-500	1	~100

### 2.3 Removal Mechanisms of Cr(VI)

Biochar prepared from biomass via pyrolysis process was selected for removal of hexavalent chromium from wastewater. Elimination of Cr(VI) from aqueous solution by conventional methods involved several physical and chemical reactions. The removal mechanisms of Cr(VI) adopted by biochar were discussed which covered adsorption, ion exchange, chemical reduction and precipitation reactions.

#### 2.3.1 Adsorption

Adsorption is the adhesion of fluid particles to a solid surface as adsorbent when they are in contact with each other. It is also expressed as the capability of an adsorbent to attract particles and remain on their surface. Adsorption involved both physical and chemical reactions complied with the nature of adsorbent and adsorbate. The physical adsorption refers to van der waals forces of attraction

which are weak intermolecular forces resulted from fluctuating polarization of neighbouring particles. It is a reversible process whereby high pressure and low temperature made physical adsorption favourable. Adsorption was usually demonstrated by chemisorption which involved the formation of chemical bonds among adsorbent and adsorbate (E-Medical Prep, 2019).

Biochar was known as a good adsorbent in contaminants removal with its relatively high specific surface area, porosity and pH. The adsorption mechanisms of Cr(VI) by biochar comprised of pore-filling, electrostatic attraction, hydrogen bonding and complexes adsorption affected by the surface charge and functional groups of biochar (Dai, et al., 2019). Negatively charged biochar surface with sufficient oxygen containing functional groups were able to induce an electrostatic attraction of biochar to positively charged chromium compounds. Other than that, negatively charged chromate ions tend to adsorb on positively charge functional groups of biochar at lower pH. The adsorption process on porous matter was usually controlled by the mechanisms of solute transport from water onto surface of adsorbent through film diffusion, diffusion within pore spaces and adsorption of ions on the interior surface of adsorbent (Choudhary and Paul, 2018).

Adsorption of Cr(VI) on biochar surface was closely related to the ion exchange and chromium reduction which can be observed in Figure 2.1. Mechanism I provided the anion adsorption of Cr(VI) on basic functional groups associated with anion exchange while mechanism II showed the reduction of Cr(VI) to Cr(III) by contacted with acid functional groups. Combination of Cr(VI) adsorption, reduction and release of Cr(III) into the solution were observed in mechanism III. Lastly, the cation adsorption of Cr(III) on adsorbent associated with cation exchange was demonstrated in mechanism IV (Reyes, et al., 2019).

Kinetics models were employed to identify the interactions between adsorbent and adsorbate. The adsorption kinetics of Cr(VI) had been widely studied by pseudo-first order (PFO) (Eq (2.1)), pseudo-second order (PSO) (Eq (2.2)) and intraparticle diffusion (Eq (2.3)) models. The kinetics models were described by equations 2.1-2.3 (Chen, et al., 2018; Zhu, et al., 2016).

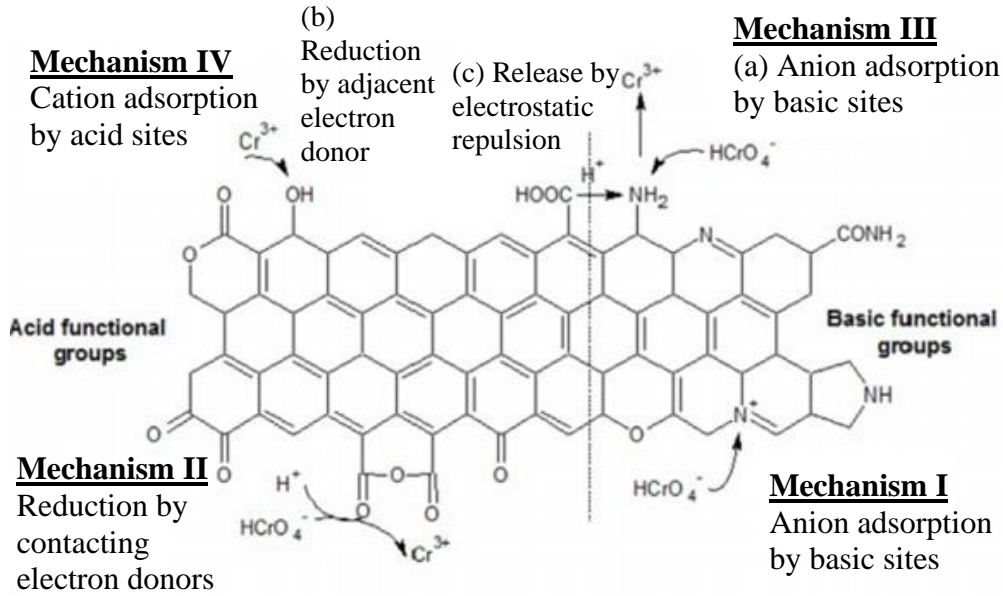


Figure 2.1: Adsorption mechanisms of Cr(VI) (Reyes, et al., 2019)

$$q_t = q_e(1 - e^{-k_1 t}) \quad (2.1)$$

$$q_t = \frac{k_2 q_e^2 t}{1 + k_2 q_e^2 t} \quad (2.2)$$

$$q_t = k_p t^{1/2} + C_i \quad (2.3)$$

where

$t$  = time,  $\text{min}$

$q_t$  = adsorption amounts of Cr(VI) at  $t$ ,  $\text{mg g}^{-1}$

$q_e$  = adsorption amounts of Cr(VI) at equilibrium,  $\text{mg g}^{-1}$

$k_1, k_2, k_p$  = adsorption rate constants of PFO,  $\text{min}^{-1}$ , PSO,  $\text{g mg}^{-1} \text{min}^{-1}$  and intraparticle diffusion,  $\text{mg g}^{-1} \text{min}^{-1/2}$  model

$C_i$  = intraparticle diffusion constant related to thickness of boundary layer,  $\text{mg g}^{-1}$

Pseudo-first order model was employed to illustrate the mechanism that the rate of adsorption was influenced by equilibrium time where it was suitable only for the initial adsorption period and incompatible for longer period. The adsorption process was usually started with an initial rapid phase followed by a slower phase and it obeyed pseudo-first order with high concentration of adsorbate at initial stage. In addition, pseudo-second order model illustrated that

the adsorption rate was directly proportional to the square of the number of active sites interacting with Cr(VI) complexes (Choudhary and Paul, 2018). Most of the adsorption kinetics of Cr(VI) was best explained by pseudo-second order model, indicating that it was a second-order reaction pathway limited by chemisorption (Zhang, et al., 2018). Intraparticle diffusion was also known as pore diffusion where it was assumed to be the rate-limiting step particularly in solid-liquid adsorption system. It was also used to determine if the adsorption process involves multi-step mechanisms (Zhu, et al., 2016). The correlation coefficients ( $R^2$ ) was evaluated to identify the model which was well-fitted with the experimental data obtained with  $>0.97$ . Based on Figure 2.2, it can be observed that the adsorption kinetics of chromium is well-defined by second order reaction with the  $R^2$  value of 0.998.

Other than kinetics study, adsorption isotherm was employed to demonstrate the adsorption of adsorbate at constant temperature and equilibrium condition. Isotherm models available for Cr(VI) removal included Langmuir isotherm (Eq (2.4)), Freundlich isotherm (Eq (2.5)) and Temkin isotherm (Eq (2.6)) models. The respective isotherm models were represented by the equations 2.4-2.6 (Choudhary and Paul, 2018).

$$q_e = \frac{Q_{max}K_L C_e}{1+K_L C_e} \quad (2.4)$$

$$q_e = K_F C_e^{1/n} \quad (2.5)$$

$$q_e = \frac{RT}{b} \ln(K_T C_e) \quad (2.6)$$

where

$q_e$  = adsorption amounts of Cr(VI) at equilibrium,  $mg g^{-1}$

$C_e$  = Cr(VI) concentration at equilibrium,  $mg L^{-1}$

$Q_{max}$  = maximum amounts of Cr(VI) adsorbed to form single layer,  $mg g^{-1}$

$K_L$  = Langmuir constant,  $L mg^{-1}$

$K_F$  = Freundlich constant related to sorption capacity,  $(mg/g)/(mg/L)^n$

$1/n$  = Freundlich constant related to sorption intensity

$R$  = gas constant,  $0.00813 kJ/mol K$

$T$  = temperature, K

$b$  = adsorption heat constant,  $kJ/mol$

$K_T$  = Temkin constant,  $L/g$

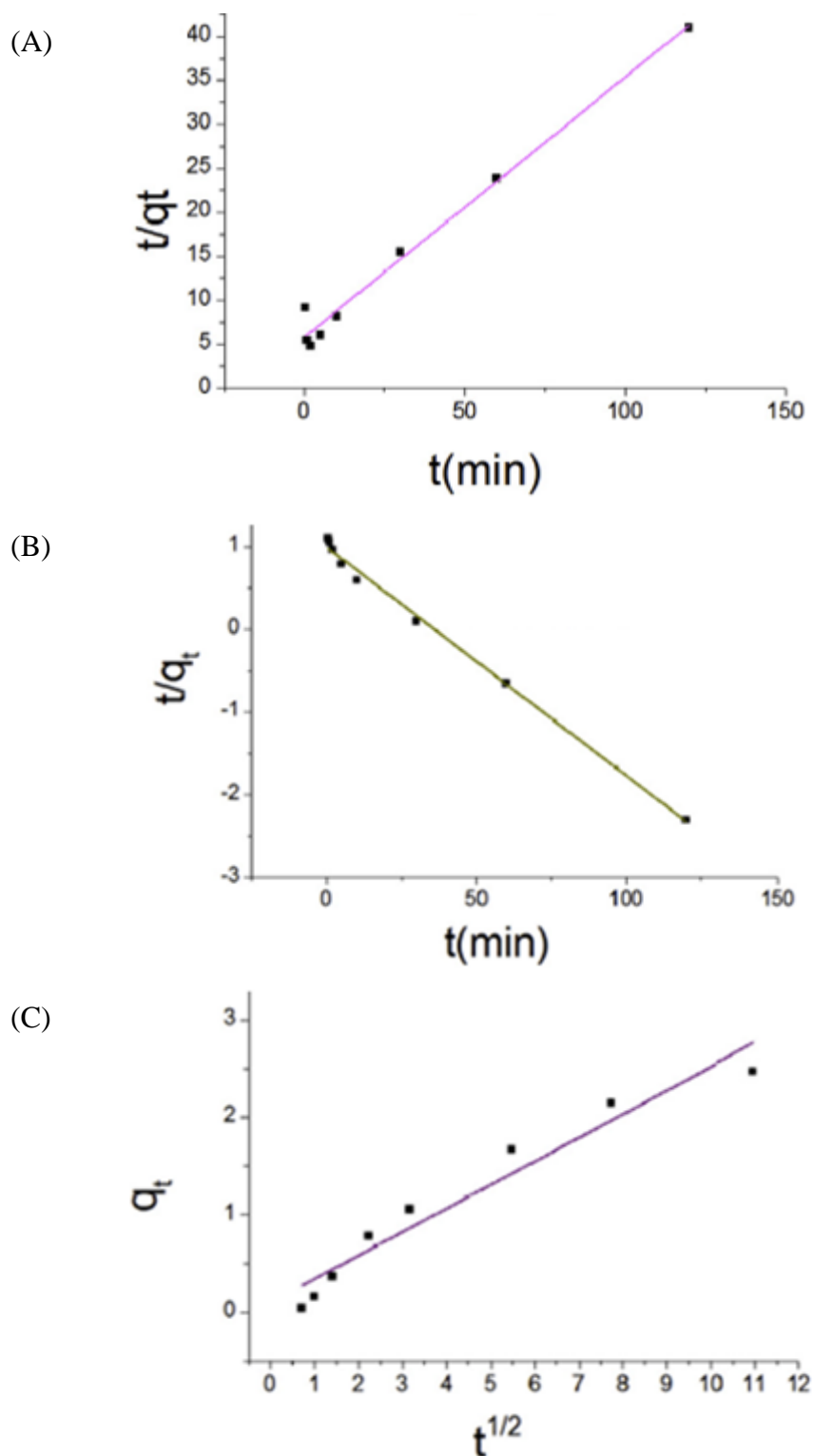


Figure 2.2: Linear plot of adsorption kinetics for chromium removal based on different kinetic models (A) Pseudo-second order kinetic, (B) Pseudo-first order kinetic and (C) Intra-particle diffusion models (Zhu, et al., 2016)

Langmuir model assumed monolayer chromium adsorption on homogeneous surface by active sites with equal affinity to adsorbate. No interaction occurred among the adsorbed substances. The  $Q_{max}$  in the Langmuir isotherm mentioned in equation (2.4) involved both adsorption and reduction processes in Cr(VI) removal. Besides, Freundlich model was derived by chemisorption on multilayer surfaces with heterogeneous heat distribution and poses varying affinity to the adsorbate. The value of  $1/n$  must be  $<1$  to show that the adsorption process was favourable. For Temkin model, the heat of adsorption was assumed to decrease linearly with surface coverage caused by the interactions between adsorbent and adsorbate with constant binding energy. Weak interaction of adsorbent and adsorbate with  $b < 8 \text{ kJ/mol}$  might lead to the release of chromium back to the solution from adsorbed surface (Choudhary and Paul, 2018). The best fitted isotherm model was vary with the experiments conducted based on the type of adsorbent used and temperature fixed whereby Langmuir isotherm usually provides a better fit for Cr(VI) removal by biochar which indicated that monolayer adsorption was relatively important and further adsorption would not occur when an active site was filled with a chromium ion. Figure 2.3 showed the comparison of several isotherm models examined for Cr(VI) adsorption.

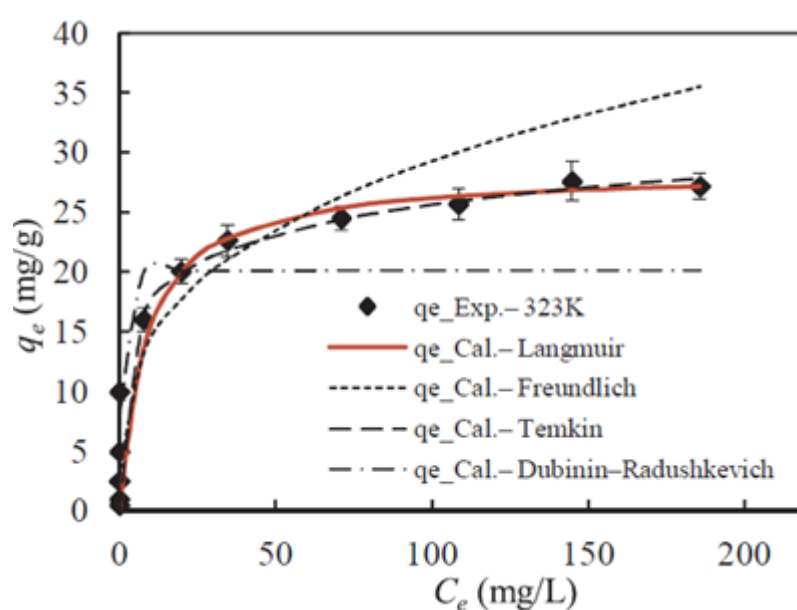


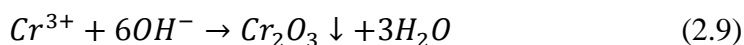
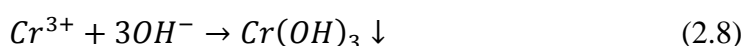
Figure 2.3: Two-parameter isotherm models in Cr(VI) adsorption on Eucalyptus globulus bark biochar at 323K (Choudhary and Paul, 2018)

### 2.3.2 Chemical Reduction and Precipitation

Chromium is commonly present in the form of Cr(VI) and Cr(III) where Cr(VI) is much more toxic and soluble in water as compared to Cr(III). Hence, Cr(VI) reduction to Cr(III) as an easily immobilized form is an effective solution for water decontamination. The Cr(VI) ions were first adsorbed onto the surface of biochar before it could be reduced into Cr(III) ions depending on the reduction capabilities of biochar based on the surface functional groups available. The Cr(III) formed was released into the water and re-adsorbed on biochar where biochar had greater affinity towards Cr(III) rather than Cr(VI) (Zhang, et al., 2018). Electron donor functional groups were required for Cr(VI) reduction by electron transfer as shown in equation (2.7) which may consist of carboxyl (-COOH), hydroxyl (-OH) and amine (-NH<sub>2</sub>) groups.



Furthermore, Cr(III) compounds are mostly insoluble in water where chemical precipitation occurred after reduction of Cr(VI). Main Cr(III) species found in water are Cr<sup>3+</sup>, Cr(OH)<sub>3</sub> and Cr(OH)<sub>4</sub><sup>-</sup>. Based on equations (2.8) and (2.9), chromium hydroxide (Cr(OH)<sub>3</sub>) and chromium oxide (Cr<sub>2</sub>O<sub>3</sub>) were precipitated by reduction of Cr(VI) as insoluble compounds. Cr(III) species were mainly positively charged in the form of Cr<sup>3+</sup>, CrOH<sup>2+</sup> and Cr(OH)<sub>2</sub><sup>+</sup> which showed higher electrostatic attraction to negatively charged biochar surface at higher pH (Li, et al., 2017). It may also form complexes with other ions available in biochar and precipitated on biochar surface.



### 2.3.3 Ion Exchange

Ion exchange was a method generally used in wastewater treatment to remove hardness and other contaminants from water including heavy metal. It is a chemical process that undesired dissolved ions are exchanged with other similarly charged ions. It was classified into cation exchange and anion exchange while the free ions have higher affinity than previously bound ions.

The elimination of Cr(VI) ions involved anion exchange processes where negatively charged chromate ions ( $\text{CrO}_4^{2-}$ ,  $\text{HCrO}_4^-$  and  $\text{Cr}_2\text{O}_7^{2-}$ ) were exchanged with other existing anions from the adsorbent (McGuire, et al., 2007). The oxygen and nitrogen functional groups of biochar contributed to the anion exchange capacity (AEC) and it was primarily attributed to the oxonium, pyridinium and amino functional groups formed during production process (Lawrinenko, 2014). The amino group tends to be protonated at lower pH which allowed Cr(VI) to be adsorbed on biochar by ionic or hydrogen bonds, reduced the nitrogen functional groups found on biochar surface (Yin, et al., 2019).

However, cation exchange was an important mechanism for removal of Cr(III) to form complexation with biochar functional groups. Biochar was known with its excellent CEC with the present of exchangeable cation including potassium ( $\text{K}^+$ ), sodium ( $\text{Na}^+$ ), calcium ( $\text{Ca}^{2+}$ ) and magnesium ( $\text{Mg}^{2+}$ ). It was observed that sorption of Cr(III) occurred with the release of cations which indicated that Cr(III) was removed by cation exchange. A slight increase in pH was noticed due to higher cation concentration in the solution with the release of calcium oxide and magnesium oxide from biochar (Li, et al., 2017). Generally, an ion with higher valence tends to have higher affinity to adsorbent. Thus,  $\text{Cr}^{3+}$  could readily exchange with  $\text{Ca}^{2+}$  and  $\text{Mg}^{2+}$  which have lower affinity on biochar.

## **2.4 Factors Affecting Removal Efficiency of Cr(VI)**

Adsorption behaviour of Cr(VI) by biochar was affected by several factors which include the pyrolysis temperature of biochar synthesis, pH of solution, residence time of adsorption process, chromium concentration in water and amount of adsorbent used. Chromium removal can be optimized by understanding the effects of each factors involved and controlling the adsorption environment.

### **2.4.1 Pyrolysis Temperature**

The pyrolysis temperature was a significant factor in biochar preparation for varying surface characteristics such as functional groups, specific surface area and pore development that would control the removal efficiency of Cr(VI) from water. It was observed that the percentage of Cr(VI) adsorbed increased with

increasing temperature up to 750°C and decreased sharply at higher temperature as shown in Figure 2.4. The difference in removal efficiency was mainly resulted from the changing in specific surface area and pore volume which affect the adsorption potential of biochar (Yu, et al., 2018). The specific surface area and pore volume were characterized by the porous structures classified into micropores, mesopores and macropores. Micropores, mesopores and macropores are pores with diameter  $< 2nm$  ,  $2 - 50nm$  and  $> 50nm$  respectively. The accessibility of active sites by Cr(VI) ions and mass transfer limitation were influenced by the pore size depending on the size of adsorbate (You, et al., 2017). The size of chromium ions was generally less than 2nm and the micropores favour the adsorption process (WebElements, 2019).

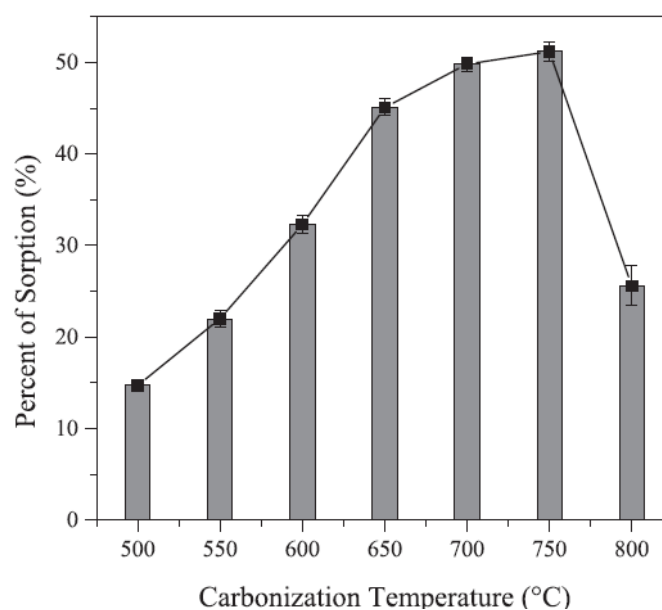


Figure 2.4: Effect of carbonization temperature of biochar on Cr(VI) removal (Yu, et al., 2018)

Based on the results studied by Yu, et al. (2018) in Table 2.4, specific surface area and pore volume of biochar increased from  $33.4 m^2/g$  to  $894.5 m^2/g$  and  $0.055 cm^3/g$  to  $0.638 cm^3/g$  respectively with temperature increased from 500-750°C. Greater tendency of volatile components to escape from biochar with increasing pyrolysis temperature generated higher specific surface area and porous structures which enhanced the adsorption process. In addition, higher temperature resulted in greater number of functional groups

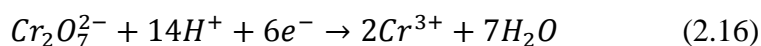
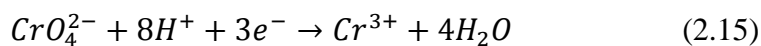
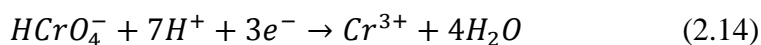
such as OH<sup>-</sup>, CHO, C=O, COO<sup>-</sup> and aromatic groups of biochar to promote the adsorption and reduction of Cr(VI) species (Xu, et al., 2018). The sharp reduction of specific surface area and pore volumes of biochar at temperature above 750°C might be due to the collapse and agglomeration of micropore structures into mesopores or macropores with larger pore size (Yu, et al., 2018). Thus, the adsorption of Cr(VI) was inhibited by biochar produced from out of range temperature with extensive heating.

Table 2.4: N<sub>2</sub> physical adsorption characteristics of biochar at different carbonization temperatures (Yu, et al., 2018)

<b>Carbonization Temperature (°C)</b>	<b>Specific Surface Area, S<sub>BET</sub> (m<sup>2</sup>/g)</b>	<b>Pore Volume (cm<sup>3</sup>/g)</b>
500	33.4	0.055
550	255.1	0.081
600	356.2	0.117
650	538.6	0.186
700	769.4	0.348
750	894.5	0.638
800	32.0	0.286

#### 2.4.2 pH

The adsorption of Cr(VI) was highly dependent on the surface charge of biochar and the types of Cr(VI) species present in water. The adsorption capacity was influenced by the pH level and point of zero charge (pH<sub>pzc</sub>) of different types of biochar. At pH < pH<sub>pzc</sub>, the surface of biochar is positively charged where the adsorption of chromium anion can be achieved by electrostatic attraction. However, the negatively charged biochar surface at pH > pH<sub>pzc</sub> leads to electrostatic repulsion of chromium anion with biochar and adsorption process will be difficult to take place (Chen, et al., 2018). Hence, the uptake of Cr(VI) anions decreased with less positively charged biochar surface at higher pH. The effects of pH on Cr(VI) species were observed in equations (2.10) - (2.13) where protonation occurs at low pH level (Zhu, et al., 2016).



Chromic acid tends to be dissociated into  $HCrO_4^-$  ions, chromate ions ( $CrO_4^{2-}$ ) and dichromate ions ( $Cr_2O_7^{2-}$ ) given by equations (2.10) to (2.13). Cr(VI) exists dominantly in the form of  $HCrO_4^-$  in acidic condition with pH 2-3 as a result of abundant  $H^+$  ions available for hydrolysis of  $Cr_2O_7^{2-}$  and  $CrO_4^{2-}$ .  $CrO_4^{2-}$  ions are predominant species at pH 4-11.  $HCrO_4^-$  had higher affinity to be adsorbed than  $CrO_4^{2-}$  and  $Cr_2O_7^{2-}$  due to the different in adsorption free energy (Yin, et al., 2019). The adsorption free energy of  $HCrO_4^-$  in the range of -2.5 to -0.6 kcal/mol was lower than  $CrO_4^{2-}$  with the values of -2.1 to -0.3 kcal/mol. This indicated that  $HCrO_4^-$  ion was more easily adsorbed than  $CrO_4^{2-}$  at same concentration (Yang, et al., 2018). The distribution of Cr(VI) species with increasing pH was shown in Figure 2.5 where  $CrO_4^{2-}$  were predominant under alkaline condition. It can be observed in equations (2.14) - (2.16) that higher acidity promoted the reduction of Cr(VI) species into Cr(III) cation (Zhang, et al., 2018). The  $Cr^{6+}$  species in the forms of  $HCrO_4^-$ ,  $CrO_4^{2-}$  and  $Cr_2O_7^{2-}$  were reduced by  $H^+$  and electron donors to produce  $Cr^{3+}$  ions and water given by equations (2.14) to (2.16).

Higher pH values indicated higher concentration of  $OH^-$  ions present in the solution which may hinder the uptake of Cr(VI) anions. This is because  $OH^-$  ions act as anions to compete with the Cr(VI) species for occupation of the adsorption sites available on biochar surface and decrease the adsorption capacity. Thus, it was observed in Figure 2.6 that the removal efficiency of Cr(VI) declined rapidly with increasing pH. In contrast, the negatively charged biochar surface at  $pH > pH_{pzc}$  favoured cation adsorption of Cr(III) (Yuan, et al., 2009). Therefore, optimum Cr(VI) removal can be achieved by lower initial pH level of solution and subsequently increased for adsorption of Cr(III) cations.

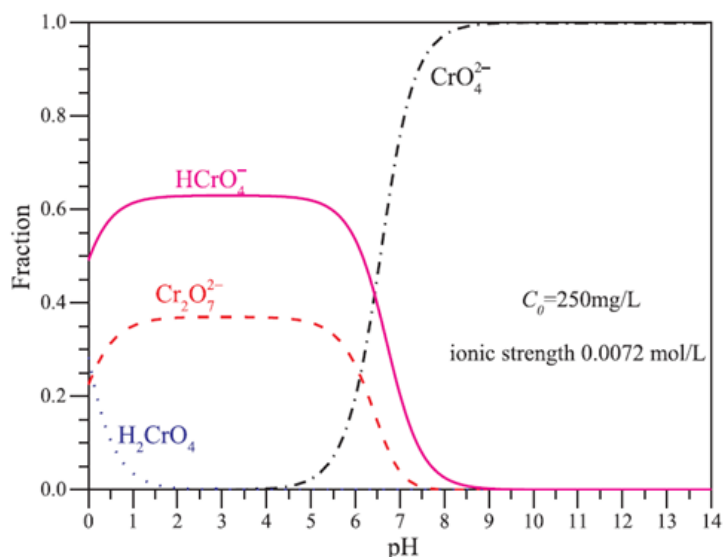


Figure 2.5: Cr(VI) species distribution with increasing pH values (Zhang, et al., 2018)

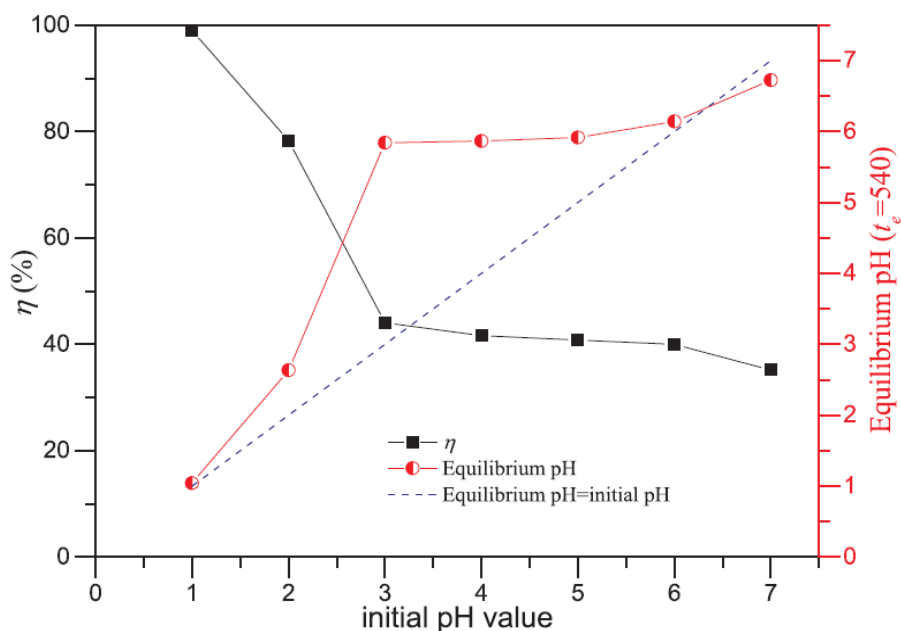


Figure 2.6: Effects of pH values on Cr(VI) removal (Zhang, et al., 2018)

### 2.4.3 Residence Time

The effects of residence time of biochar in water containing Cr(VI) was studied under constant pH, temperature, biochar dosage and initial concentration of Cr(VI). According to Figure 2.7, the initial Cr(VI) adsorption rate on biochar increased rapidly at the first 2 hours (Yu, et al., 2018). It was explained by the large amounts of vacant adsorption sites on biochar available for Cr(VI) to be adsorbed initially with stronger electrostatic attraction. Rapid adsorption

occurred on external surface of biochar with greater accessibility by Cr(VI) at initial contact time (Yuan, et al., 2009). As time proceeding, higher number of Cr(VI) species adsorbed on the surface of biochar and the number of vacancies decreased leading to a reduction in the rate of adsorption. Eventually, the percentage of Cr(VI) adsorbed reached an equilibrium level where all of the adsorption sites of biochar were fully filled.

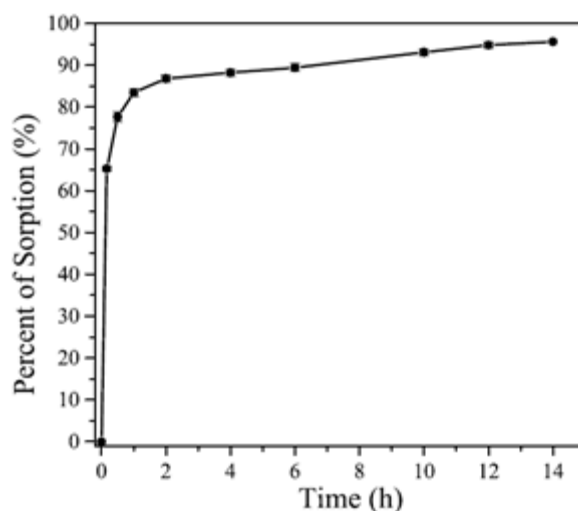


Figure 2.7: Effect of residence time on Cr(VI) adsorption (Yu, et al., 2018)

The relationship between the amounts of Cr(VI) ions adsorbed and residence time was also demonstrated by various kinetic models. As a result of previous analysis in Figure 2.2, pseudo-second order was best fitted for the adsorption kinetic of Cr(VI) ions. It was implied that chemisorption associated with the attractive forces by sharing or exchanging of electrons between biochar surface and Cr(VI) species was limiting the adsorption rate which was proportional to the availability of adsorption sites (Yuan, et al., 2009).

#### 2.4.4 Initial Chromium Concentration

The effect of initial chromium concentration was studied by the mechanism of adsorption isotherm. It was defined that the amounts of Cr(VI) adsorbed at equilibrium ( $q_e$ ) were higher with higher concentration of Cr(VI) species present in the solution until a maximum level as shown in Figure 2.3. Nevertheless, the percentage of Cr(VI) removal were lower with higher initial concentration of Cr(VI) as illustrated in Figure 2.8 (A). The phenomena was attributed to the

insufficiency of total adsorption sites of adsorbent available for Cr(VI) adsorption at particular adsorbent dosage within selected time where higher concentration of Cr(VI) required larger amounts of adsorption sites for adsorption to take place (Yuan, et al., 2009). Saturation occurred where the adsorption sites were fully utilized with higher concentration of Cr(VI) and no further adsorption was allowed (Chen, et al., 2018). On the other hand, the removal capacity of Cr(VI) increased with higher initial Cr(VI) concentration as shown in Figure 2.8 (B). Higher removal capacity was associated with higher concentration of Cr(VI) available to be removed whereby resulted in higher rate of removal at higher initial concentration of Cr(VI). However, the rate of removal decreased with increased residence time for lower removal capacity.

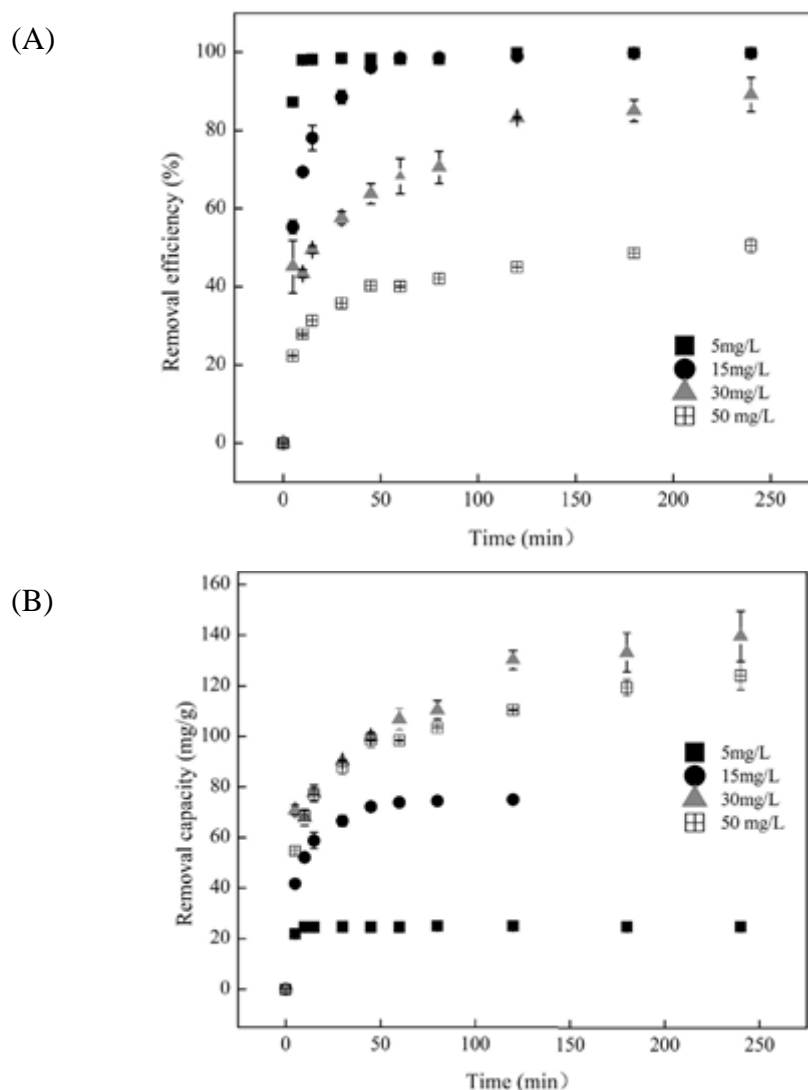


Figure 2.8: Effect of initial concentration of Cr(VI) on Cr(VI) (A) removal efficiency and (B) removal capacity (Gao, et al., 2018)

### 2.4.5 Amount of Adsorbent

The dosage of biochar was an essential factor for effective removal of Cr(VI) from water. Higher dosage of adsorbent enhanced the removal efficiency, affected by the coefficient of distribution ( $K_D$ ) which representing the binding ability of adsorbate over the surface of adsorbent. By increasing adsorbent dosage,  $K_D$  may remain constant in the case of homogeneous distribution of active sites on adsorbent surface or increase with heterogeneous adsorbent surface.  $K_D$  can be calculated by equation (2.17) (Zhu, et al., 2016).

$$K_D = \frac{C_e}{C_a} \quad (2.17)$$

where

$C_e$  = concentration of adsorbate on adsorbent,  $mg/g$

$C_a$  = concentration of adsorbate in aqueous solution,  $mg/L$

Generally, the adsorption capacity of biochar increased with higher dosage resulted by higher availability of adsorption active sites. However, higher amounts of Cr(VI) adsorbed onto the surface of biochar reduced the number of adsorption sites. Thus, the removal capacity measured in amount of Cr(VI) removed per unit mass of biochar was reduced as shown in Figure 2.9 (Choudhary and Paul, 2018). In consequence, the removal of Cr(VI) reached equilibrium level with maximum level of Cr(VI) adsorbed on biochar surface.

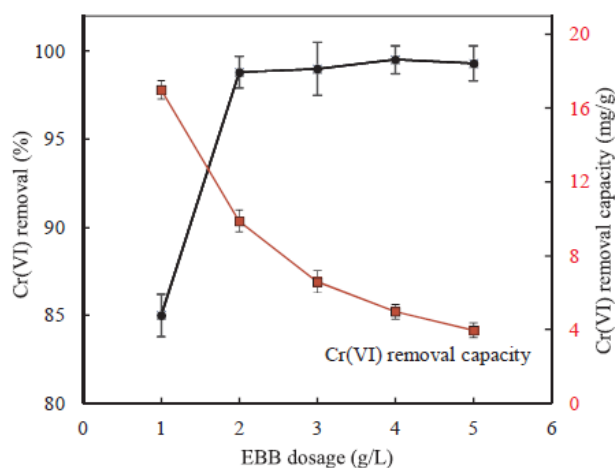


Figure 2.9: Effect of biochar dosage on removal of Cr(VI) (Choudhary and Paul, 2018)

## **2.5 Modifications on Biochar**

There are several types of compounds which were applicable for modification of biochar to enhance its physical and chemical properties in Cr(VI) removal. They were loaded on biochar to form composites where biochar commonly treated as a support for the compounds. The compounds available to form composites with biochar in the application of Cr(VI) removal included carbonaceous materials, nano-zerovalent iron, metal or metal oxides nanoparticles and polymers.

### **2.5.1 Carbonaceous Materials**

Carbonaceous materials are organic matters which were often added to increase the surface area of biochar (Wang and Wang, 2019). Besides that, carbonaceous materials contained functional groups to create strong bonds between biochar surface to the pollutants in aqueous medium and improved the adsorption capacities of biochar on different aqueous pollutants (Premarathna, et al., 2019). Carbon nanotubes (CNTs) and graphene-based materials had been extensively used in environmental remediation especially in water treatment (Sarkar, et al., 2018).

CNTs composed of enrolled cylindrical graphitic sheets where the carbon atoms were located at the corners of hexagons as shown in Figure 2.10. It was known with the basic properties of large specific surface area, high thermal and chemical stability as an effective adsorbent for decontamination of water and wastewater (Sarkar, et al., 2018). Despite that, relatively high cost of CNT and difficulty in recovery due to its nanostructures limited its usage. Biochar served as a microporous or mesoporous carrier of CNT to form an effective and recyclable adsorbent in water remediation (Rajapaksha, et al., 2016). CNTs were commonly used in composite synthesis owing to the enhanced binding affinity with hydroxide (-OH) and carboxyl (-COOH) groups by chemical oxidation methods. The porous structure of biochar with relatively high surface area functioned to distribute and stabilize the CNTs (Premarathna, et al., 2019).

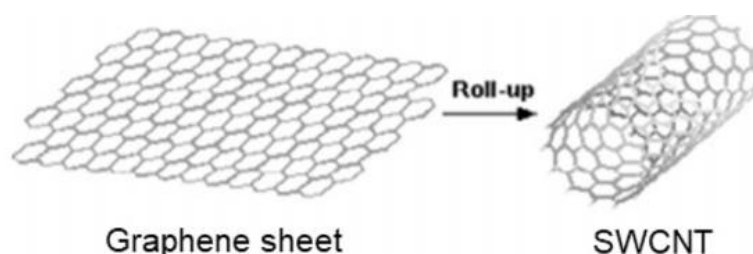


Figure 2.10: Formation of single-walled carbon nanotube (SWCNT) from graphene sheet (Sarkar, et al., 2018)

Graphitic carbon nitride ( $g\text{-C}_3\text{N}_4$ ) is a polymeric metal-free semiconductor with mild band gap of 2.7 eV in which low energy was required to activate it and it was the most stable material among  $\text{C}_3\text{N}_4$  allotropes (Magesa, et al., 2019; Mamba and Mishra, 2016). It is an organic matter composed of carbon, nitrogen and minor hydrogen atoms with high photostability and UV/visible light response (Li, et al., 2019).  $g\text{-C}_3\text{N}_4$  appeared to have layered structures with triazine-based (s-triazine) or heptazine-based (tri-s-triazine) structures which are planar as shown in Figure 2.11. Rotation at N-N bonding between the building blocks and the presence of intrinsic vacancies created amorphous  $g\text{-C}_3\text{N}_4$  structures (Inagaki, et al., 2019).  $g\text{-C}_3\text{N}_4$  that was rich in defects with N-bridged poly(tri-s-triazine) and nitrogen atoms which act as strong electron donors that provided large amounts of active sites for electron conductivity (Magesa, et al., 2019). In the view of its excellent electrical, optical, structural and physiochemical properties,  $g\text{-C}_3\text{N}_4$  was widely applied in electronic, photocatalytic and energy fields (Wen, et al., 2017).

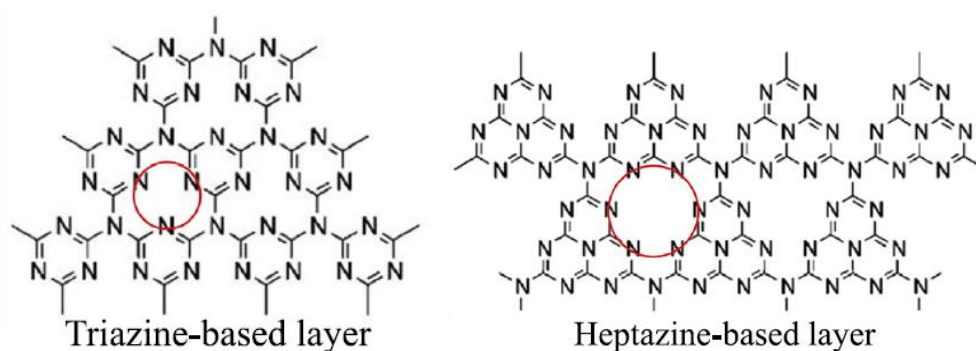


Figure 2.11: Structures of  $g\text{-C}_3\text{N}_4$  with circled characteristic intrinsic vacancies surrounded by nitrogen atoms (Inagaki, et al., 2019)

However, there were several drawbacks of bulk g-C<sub>3</sub>N<sub>4</sub> such as high electron-hole recombination rate, inefficient absorption of visible light, small specific surface area (<10 m<sup>2</sup>/g) with high degree of condensation, less photoreaction active sites and poor electrical conductivity (Wen, et al., 2017). The band gap of 2.7 eV referred to the potential difference in electron hole with a threshold wavelength of 450 nm. It was inefficient to harvest visible light with the wavelength of 380-750 nm (Mamba and Mishra, 2016). Photocatalytic activities required more photogenerated electron-hole pairs for oxidation and reduction reactions on the surface (Jeon, Lee and Baek, 2017). Larger surface area restricted the diffusion pathway of electron-hole pairs, providing higher formation of radical species as reactive sites to increase the reaction kinetics (Mamba and Mishra, 2016).

Many researches had been carried out to study on the modification of g-C<sub>3</sub>N<sub>4</sub> for improved surface area, charge separation, optical properties and photocatalytic degradation kinetics (Mamba and Mishra, 2016). For instance, conductive carbon materials served as efficient medium for electron transfer and improved the separation of electron-hole pairs to provide sufficient catalytic sites. Thus, the combination of g-C<sub>3</sub>N<sub>4</sub> and biochar was expected to have high adsorptive and photocatalytic capacities in decontamination of water. In addition, biochar supported g-C<sub>3</sub>N<sub>4</sub> tends to have light-responsive self-generation capability which has the potential to maintain a long-term decontamination capability with photocatalytic process (Pi, et al., 2015).

### **2.5.2 Nano-zerovalent Iron**

Nano-zerovalent iron (nZVI) was one of the nanoparticles extensively applied in wastewater and soil remediation due to its properties and effectiveness in removal of heavy metals and organic compounds. nZVI had high reactivity and removal capacity of heavy metals with its much smaller crystallite size than micron or millimeter-sized particles. Smaller particles size resulted in greater surface area to volume ratio with larger active sites and lower surface energy. The removal mechanisms performed by nZVI include reduction, adsorption, oxidation, surface complexation, precipitation, dichlorination and Fenton-like degradation (Wang, et al., 2019). nZVI was a strong reducing agent to remove various heavy metals by enhanced chemical reduction (Qian, et al., 2019).

In spite of the enhanced contaminants removal, smaller particles size of nZVI was unstable where rapid loss of reactivity occurred by agglomeration and precipitation reaction (Gao, et al., 2018). Thus, supporting materials such as silica, activated carbon and zeolites were used to immobilize nZVI by trapping them inside the pores while at the same time improved its physiochemical properties (Stefaniuk, Oleszczuk and Ok, 2016). Biochar was an effective supporting material for nZVI attributed to its large specific surface area, porous structure and high adsorption capacity with numerous surface functional groups (Qian, et al., 2019). Biochar improved the dispersion of nZVI particles by segregating them with a carbon skeleton barrier inside the pores. Moreover, the surface functional groups of biochar could react with the oxide shell of nZVI to form stable bonds. Surface corrosion of nZVI was controlled by immobilization of Fe ions with the formation of complexes to functional groups of biochar and resistance to oxidation in the presence of microporous, mesoporous structures, reducing and acidic functional groups of biochar. Biochar also improved the electron transfer capability of nZVI with the ability of the surface functional groups to accept or donate electrons (Wang, et al., 2019).

The aggregation of nZVI particles could also be avoided by surface coating of polymers to reduce electrostatic attraction of particles resulted from a change in surface charge (Stefaniuk, Oleszczuk and Ok, 2016). Carboxymethyl cellulose (CMC) is a non-toxic, affiliate anionic polymer which created smaller particles size of nZVI and stabilizes it by reducing its oxidation state (Zhang, et al., 2019). The leaching of Fe during the redox reaction of biochar supported nZVI could be reduced by addition of calcium alginate (CA) which contained abundant functional groups to uptake the dissolved metal ions (Wan, et al., 2019). Besides that, silicon served as support sites in promoting Fe<sup>0</sup> crystallinity and the silicon oxide (SiO<sub>2</sub>) found in biochar facilitated the oxidation of Fe<sup>0</sup> with enhanced electron transfer (Qian, et al., 2019). Sulfidation of nZVI (S-nZVI) increased the electron conductivity and controlled the corrosion rates of nZVI for higher reactivity and lifetimes in the presence of S<sup>2-</sup> species (Gao, et al., 2018).

### 2.5.3 Metal or Metal Oxide Nanoparticles

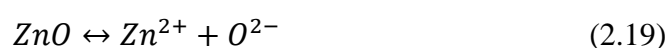
Metal oxides consist of positively charged metal ions which capable of removing other metal cations or anion species by ion exchange and electrostatic attraction. It provided more adsorption sites for biochar in heavy metal removal. Nanostructured inorganic materials had flexible physiochemical properties and large surface area while their toxicity was highly dependent on the properties (Castillo, et al., 2019). The coating of metal oxides nanoparticles on biochar improved the adsorption capacity by increased porosity, specific surface area, number of functional groups and anionic adsorption active sites of pristine biochar. The surface electrochemical properties of biochar were affected in the presence of metal oxides and changed from negatively-charged to positively-charged surface (Xiao, et al., 2018). The metal nanoparticles available for Cr(VI) removal from wastewater included magnesium oxide, zinc oxide, iron oxide and iron monosulfide.

Magnesium oxide (MgO) nanoparticles are chemically stable and non-toxic by comparing to other metal oxides (Kumar, et al., 2018). MgO consists of irreducible oxide ( $O^{2-}$ ) and a very electropositive cation ( $Mg^{2+}$ ) with a rock-salt structure where the surface of each  $Mg^{2+}$  is surrounded by five  $O^{2-}$  ions. There were many surface defects in MgO such as edges, corners and kinks that were important in breaking the chemical bonds of adsorbates to improve adsorption. The anhydrous surface of MgO provided two active sites of  $Mg^{2+}$  cation and  $O^{2-}$  anion given by equation 2.18 for adsorption reaction to take place where the oxygen vacancies resulted in anion attraction (Elkhalifa and Friedrich, 2014). The favourable properties of MgO nanoparticles such as high charge carrier diffusion length, specific surface area, surface to volume ratio and adsorption capability encouraged its application in removal of water contaminants especially anionic compounds (Li, et al., 2015).



Nanosized zinc oxide (ZnO) was also one of the non-toxic semiconductor metal oxide widely used in photocatalytic applications (Ruba, et al., 2019). ZnO possess a broad band gap of 3.37 eV and large exciton binding energy of 60 meV at room temperature. It absorbed light energy with frequency

larger than its band gap to promote electron conductivity by creating positively charged holes for electron attraction (Ubani and Ibrahim, 2019). Nanosized ZnO can be activated under UV irradiation and therefore it had been developed as nano photocatalyst with its ability to produce radicals for environmental decontamination by redox reaction (Ruba, et al., 2019). Other than that, various types of intrinsic point defects such as oxygen vacancies ( $V_O$ ), zinc ( $V_{Zn}$ ) vacancies, O interstices ( $O_i$ ) and Zn interstices ( $Zn_i$ ) presence in ZnO were responsible for its conductivity with higher electron mobility (Tu, et al., 2019). ZnO nanoparticles tends to maintain a positive charge ( $Zn^{2+}$ ) as shown in equation 2.19 and high specific surface area for electrostatic adsorption of negatively charged pollutants (Hu, et al., 2019).



Iron oxide nanoparticles included magnetite ( $Fe_3O_4$ ) and hematite ( $\alpha$ - $Fe_2O_3$ ) with unique biochemical, magnetic and catalytic properties had been applied as effective adsorbents for Cr(VI) removal. Magnetite contains both divalent and trivalent iron, differing from other iron oxides (Bhateria and Singh, 2019). Iron oxide nanoparticles were widely applied due the properties such as small particle size ranging from 10-100nm, magnetic, biocompatibility and low toxicity. The strong magnetic properties of iron oxides were owing to the presence of 4 unpair electrons in the 3d orbital (Elrahman and Mansour, 2019). The shifting of  $Fe^{2+}$  to  $Fe^{3+}$  served as active adsorption sites and facilitated the reduction of adsorbate ions. However, Fe was highly susceptible to auto-oxidation which yields a passivation layer of Fe(III) oxides like goethite ( $\alpha$ - $FeOOH$ ), affecting its reactivity and reducing potential (Yang, et al., 2019).

In addition, iron monosulfides (FeS) are highly reactive metal minerals composed of iron and sulfur found in anoxic geological environments which were formed by sulfate reducing bacteria in the presence of reducing agents such as organic carbon. Iron sulfides consist of mackinawite, pyrrhotite and greigite that are vary in forms while FeS is a less stable amorphous form of them (Choppala, et al., 2017). It was used as a sink in removal and immobilization of heavy metals and chlorinated hydrocarbons via sorption and precipitation mechanisms with its excellent adsorbent properties (Du, et al., 2016; Choppala,

et al., 2017). However, FeS was easily oxidized to insoluble disulfide, polysulfide, oxysulfur compounds or elemental sulfur under oxidizing condition and resulted in deprotonation to increase the acidity of solution. Acidic conditions stimulated the dissolution and release of toxic elements in FeS matrix such as Pb, Cd, Hg, and Cu due to the presence of H<sup>+</sup> ions and lead to contamination of aqueous media (Chirita and Schlegel, 2015). Oxidation of FeS also resulted in losing of its reductive capability (Du, et al., 2016).

FeS acts as a source of Fe<sup>2+</sup> and S<sup>2-</sup> species for electron donation to facilitate the chemical reduction of Cr(VI) species into Cr(III) ions. Chemisorption played a significant role for adsorption process of FeS in the presence of high oxidation state iron cation and reduction state sulfide anion (Chen, et al., 2019). Nanoscale FeS particles have much smaller particle size than bulk particles or natural minerals where it poses higher reactivity associated with its larger specific surface area. Despite that, tiny particles tend to be unstable and easily agglomerate in aqueous solution (Lyu, et al., 2017). The application of unmodified FeS in water remediation was restricted where it was prone to aggregation and oxidation process which results in lower chemical reactivity (Chen, et al., 2019).

In spite of the excellent adsorption properties, the nanosized particles tend to agglomerate rapidly and increase its particles size with lower specific surface area, leading to poor adsorption and difficulty in materials recovery (Kumar, et al., 2018). The reactivity was reduced by less availability of active sites on surface of metal or metal oxides owing to agglomeration. Immobilization of nanoparticles within porous carbonaceous matrix such as graphene and carbon nanotubes aids in segregation of particles (Wang, et al., 2018). Biochar is one of the sources of porous carbon matrix applicable to support the nanoparticles for better dispersion. Biochar based metal nanocomposites were widely used in water and wastewater decontamination process due to its abundant and inexpensive biomass raw materials (Gholami, et al., 2019).

#### **2.5.4 Polymers**

Polymer consists of long macromolecular backbones with plenty of functional groups which may be cationic or anionic. It can be an environmentally friendly

materials applied to the remediation of toxic heavy metals in aqueous solution. Impregnation of polymers facilitated the adsorption capacity of pristine biochar with integration of additional functional groups as active adsorption sites for heavy metal ions especially cationic functional groups for removal of anionic Cr(VI) species. The polymers used to form composites with biochar for Cr(VI) removal included polypyrrole and polyethylenimine.

Polypyrrole (PPy) is an organic conducting polymer with mechanical flexibility and charge-transport properties (Prokes, et al., 2019). It is composed of pyrrole monomers with the molecular formula of  $H(C_4H_2NH)_nH$ . Conducting polymers had flexible electroactivity and morphology with either conventional globular morphology or nanostructures such as nanotubes, nanorods and nanofibers (Minisy, et al., 2019). Nanostructured PPy exhibited better properties as compared globular PPy with large specific surface area, high conductivity, thermal stability and resistance to oxidative stress (Prokes, et al., 2019). PPy was widely used as conducting polymer due to its biocompatibility, environmental stability, high electroconductivity, flexibility and ease of preparation (Chouvy, Fakhry and Pillier, 2018). PPy was also a good adsorbent in removal of various components including anionic, aromatic and organometallic compounds by ion exchange, electrostatic attraction by positively charged nitrogen atoms (Pires, et al., 2019).

Due to the strong non-covalent interaction between aromatic rings ( $\pi - \pi$  stacking) in the polymer chain, PPy particles had high tendency to self-aggregate. Agglomeration of PPy particles leads to reduction in specific surface area with poor mass transfer properties in its applications (Fang, et al., 2018). Besides that, the conductive capability of PPy was reduced by the electrical properties resulted from structural conformation with frequent ion exchange (Thines, et al., 2017). Thus, materials with high specific surface area such as graphene and biological carbon could be used to overcome agglomeration and increase surface area of PPy (Amalraj, et al., 2016). Biochar is an effective adsorbent with high porosity and various surface functional groups of oxygen. However, its application in Cr(VI) removal was limited by negatively charged surface and low anion exchange capacity (Yang, et al., 2018). In this case, PPy was applicable to improve its adsorption capacity with synergism between the constituents (Amalraj, et al., 2016).

Other than that, polyethylenimine (PEI) is a polymer consists of many primary and secondary amine groups along its macromolecular chains (Ma, et al., 2014). Large amounts of positively charged amino groups in PEI allowed biochar surface to become positively charged for electrostatic interaction and complexation with heavy metal ions. PEI showed excellent properties with high mechanical strength, chemical stability and durability (Qi, et al., 2019). In addition, it was charged over a wide range of pH to allow the binding of heavy metal ions and enhanced the adsorption capability (Ma, et al., 2014). However, PEI was highly soluble in water whereby it cannot be used solely as an adsorbent for metal ions removal from wastewater without being incorporated into other support materials (Godiya, et al., 2019). Thus, modification of biochar by using PEI provided more binding sites for metal adsorption while biochar served as a support for PEI for enhanced stability (Ma, et al., 2014).

## CHAPTER 3

### METHODOLOGY

#### 3.1 Synthesis of Biochar

There are several techniques available for biochar production which include pyrolysis, gasification, hydrothermal carbonization and microwave processes. Different types of production techniques and the biomass feedstocks used provide variable yields and properties of biochar based on the operating conditions. Selection of optimum production technique relies on the desired product characteristics to be obtained.

##### 3.1.1 Pyrolysis

Pyrolysis is a thermochemical conversion process by heating biomass to temperature above 400 °C in the absence or low concentration of oxygen (Elkhalifa, et al., 2019). It was focused on restricting or eliminating oxygen during heating of biomass to prevent the reaction of carbon with oxygen and retain higher composition of carbon. Thus, carbon combined to form large amounts of stable aromatic carbon rings consist of mainly pure carbon (Richards, 2016). Biomass could be converted to solid biochar, liquid bio-oil and gaseous products via pyrolysis process. The gaseous products include volatile gases such as carbon dioxide, carbon monoxide, hydrogen, methane and condensable organic compounds like methanol and acetic acid (Weber and Quicker, 2018). Variation in pyrolysis conditions resulted in different proportions of solid, liquid and gaseous products.

Pyrolysis was further classified into slow pyrolysis and flash pyrolysis under different operating temperatures and residence times. Slow pyrolysis was a preferably method for biochar production with low heating rates at lower temperature and longer residence time. The operating conditions of slow pyrolysis were at temperature of 400-500°C, heating rate of 0.1-1°C/s and lasting for about 5 to 30 minutes while flash pyrolysis operated at temperature of 800-1300°C, heating rate of 10-200°C/s for only 1-10 seconds (Elkhalifa, et al., 2019). Even though higher heating rate promoted the degradation of organic compounds to form volatile components and the carbon skeleton with higher

carbon contents, lower biochar yield will be obtained (Zhu, Li and Wang, 2019). Liquid yield for flash pyrolysis could reach about 75% of dry matter in the feedstock. However, polymerization of organic compounds in vapor and gas phase might increase the solid yield by secondary char formation with increasing residence time of the gases in the pore structure (Weber and Quicker, 2018). Thus, flash pyrolysis was not feasible for biochar production since it produced higher yield of liquid bio-oil with increasing degradation of organic components (Zhu, Li and Wang, 2019). Slow heating rate and higher residence time with prolong gases and solid contact were preferable for solid biochar yield.

Higher pyrolysis temperature accelerated the degree of carbonization. This resulted in the formation of amorphous structure with the release of H, O, N containing functional groups in gaseous phase through decomposition and volatilization of moisture and labile compounds (Zhu, Li and Wang, 2019). Greater loss of volatile components with rising pyrolysis temperature ended up with a product of higher porosities, surface area and lower bulk density. Surface area was also increased with residence time but it was less effective as compared to rising temperature. Further increase in temperature ( $\sim 1000^{\circ}\text{C}$ ) might lead to decrease of surface area due to the shrinkage of solid matrix. Biochar will be more hydrophobic at higher pyrolysis temperature with large amounts of escaping polar surface functional groups and higher aromaticity. Nevertheless, loss of non-polar functional groups like aliphatic groups at temperature above  $500^{\circ}\text{C}$  merely reduced the hydrophobicity of biochar. Continuous formation of conjugated double bonds by leaving functional groups accelerated the conductivity of biochar (Weber and Quicker, 2018).

Moreover, energy yield for biochar decreased with increasing pyrolysis temperature while it was increasing for bio-oil and gases. Higher temperature provided greater degree of partial detachment of functional groups, creating unpaired negative charges which were able to accept more protons ( $\text{H}^+$ ) and suppress the rise of acidity with pH buffering. The detached functional groups were predominantly acidic in nature which include hydroxyl, carboxyl and formyl groups. Hence, biochar had higher alkalinity and pH value with increasing pyrolysis temperature due to higher ash content and removal of acidic functional groups (Ippolito, et al., 2015). It was also affected by residence time in which longer time of pyrolysis facilitated the release of acidic functional

groups and increased in pH and alkalinity. Biochar produced from lower pyrolysis temperature with lower pH tends to have higher cation exchange capacity (CEC) with higher capabilities of holding exchangeable cation like  $\text{Ca}^{2+}$ ,  $\text{Na}^+$  and  $\text{Mg}^{2+}$  (Weber and Quicker, 2018). The relationship of pH, surface area and CEC with increasing pyrolysis temperature were listed in Table 3.1.

Table 3.1: Average pH, surface area and cation exchange capacity (CEC) based on pyrolysis type and temperature (Ippolito, et al., 2015).

<b>Pyrolysis Type</b>	<b>Temperature (°C)</b>	<b>pH</b>	<b>Surface Area (<math>\text{m}^2/\text{g}</math>)</b>	<b>CEC (<math>\text{mmol}/\text{kg}</math>)</b>
Fast	300-499	8.33	44.74	28.8
	500-699	7.70	40.99	-
	700-900	10.1	178.2	-
Slow	<300	5.01	1.686	327
	300-499	7.81	81.32	268
	500-699	9.09	180.5	218
	700-900	10.1	189.8	41.5

### 3.1.2 Gasification

Gasification is a direct heating of biomass with little oxygen which is insufficient for combustion while partial oxidation takes place (Talberg, 2009). It was primarily used to convert the carbonaceous contents of feedstocks into gases such as hydrogen, carbon monoxide, carbon dioxide, nitrogen and other hydrocarbons with low molecular weight by reacting with steam, air or oxygen at temperature of 700-900°C (Elkhalifa, et al., 2019). By comparing to pyrolysis process, gasification required higher temperature ( $> 700^\circ\text{C}$ ) and limited amount of oxygen for oxidation process. Lower biochar yield will be obtained from gasification process subsequent to the targeted gaseous products (Wang and Wang, 2019). Solid biochar was considered as by-product of the process together with ash, oils, tars and harmful gases like  $\text{SO}_x$  and  $\text{NO}_x$  while the syngas produced as primary product are usually hydrogen based (Talberg, 2009). Steam reforming and water-gas shift reaction resulted in lower yield of liquid tar (Yu, et al., 2019).

Pore clogging by ash melting, tar deposition, pore collapse and expansion at high temperature of gasification process lead to smaller specific surface area and total pore volumes of biochar than that produced by pyrolysis. However, the oxidizing gases like oxygen or steam provided activation effects to increase the surface area and total pore volume which were able to offset the defects at high temperature (You, et al., 2017). Gasification may produce solid biochar containing harmful substances like polycyclic aromatic hydrocarbons (PAHs) in the presence of oxygen and high temperature (Weber and Quicker, 2018). PAHs are persistent organic pollutants with two or more aromatic rings which are carcinogenic, mutagenic and teratogenic (Wang, Wang and Herath, 2017). However, the PAHs present on biochar surface induced structures with larger surface area and higher volume of micropores. Therefore, it created more fractures and disintegrated surface morphology with larger surface area (Azargohar, et al., 2019). Shorter residence time of gasification process which was usually in seconds promoted rapid devolatilization of feedstock to give smaller particle size of biochar.

During the gasification process, carbon content in biochar slightly decreased due to the partial oxidation reaction and carbon conversion into gaseous compounds such as carbon monoxide and carbon dioxide as shown in Table 3.2. However, the atomic ratio of O/C and H/C decreased with increasing gasification temperature similarly to pyrolysis process due to the improvement of aromaticity of biochar. The O/C and H/C ratios of biochar produced by gasification process with similar raw material (canola meal) were 0.15-0.16 and 0.8-0.9 which were higher than that produced by slow pyrolysis with the ratios of 0.08-0.21 and 0.23-0.88. A greater loss of carbon in biochar with the existence of oxygen in gasification process indicated that biochar produced by pyrolysis were more aromatic compared to it. Development of highly condensed aromatic structure at higher temperature through thermal dehydrogenation, decarboxylation, deamination, thermal cracking and aromatization offered greater thermal stability of biochar (Azargohar, et al., 2019).

Table 3.2: Elemental composition of biochar produced from canola meal via gasification process (Azargohar, et al., 2019).

Temperature (°C)	O (wt%)	C (wt%)	N (wt%)	H (wt%)	Ash (wt%)
650	16.1	48.9	1.4	4.9	26.8
750	11.6	47.6	1.3	4.1	33.6
850	5.77	46.8	0.8	3.8	40.7

Formation of biochar by gasification process was restricted to maximize the energy recovery with higher yield of energy rich syngas, limited by operating conditions. Higher energy per unit mass of carbonaceous materials were formed through gasification due to its higher efficiency of carbon conversion. Gasification also resulted in greater loss of functional groups including hydroxyl, carboxyl and carbonyl groups under high temperature. For example, biochar obtained from gasification contained lower fraction (~10wt%) of aromatic C-H groups than biochar produced by slow (~30wt%) and fast pyrolysis (~23wt%). The partial oxidation at high temperature also produced to higher ash content and pH value of biochar compared to that produced by pyrolysis. The pH of gasification was in the range of pH 7-12 subject to relatively high alkalinity which was caused by the high degree of carbonization, metal salt and ash contents (You, et al., 2017).

### 3.1.3 Hydrothermal Carbonization

Hydrothermal carbonization is a process of heating the raw biomass added with deionized water at temperature below 250°C under oxygen limiting condition (Wang and Wang, 2019). The biochar obtained by hydrothermal carbonization is often referred to hydrochar. The yield of hydrochar was often less than pyrolysis biochar due to the presence of supercritical water which promotes the breaking of ether and ester bond in monosaccharides by hydrolysis and reduced the activation energy of biomass polymer. It reduced the degradation temperature of cellulose, hemicellulose and lignin to 200°C, 180-220°C and 180-220 °C respectively. Rapid decomposition of carbohydrates and lignin into simple sugar at low temperature created lower yield of hydrochar for about 28.9%

than pyrolysis biochar for 37%. Similarly, the yield of hydrochar decreased with increasing temperature by intensified decarboxylation, dehydration and aromatization processes (Jian, et al., 2018). Other than hydrochar, gaseous products consist mainly of CO<sub>2</sub> with only 1-3% of raw material and liquid products such as inorganic salts, sugars and organic acids are formed by hydrothermal carbonization (Wilk and Magdziarz, 2017).

Intensified hydrolysis reactions with the addition of water during hydrothermal carbonization enhanced the physical characteristics of hydrochar. Degradation of lignocellulosic components at lower temperature in the presence of water accelerated the destruction of biomass structure to form hydrochar with larger specific surface areas and total pore volumes. Lower lignin contents allowed hydrochar to have a structure with higher porosity. Based on Table 3.3, the surface area and total pore volumes of hydrochar were larger than pyrolysis biochar and they were increasing at higher temperature resulted from the degradation and depolymerization of cellulose and hemicellulose structures. However, further increased in reaction temperature to temperatures higher than 230°C resulted in decreasing specific surface area with the loss of fibrous structure and formation of a smooth surface (Kambo and Dutta, 2015).

Table 3.3: Surface area and porosity of hydrochar and pyrolysis biochar produced from manure waste (Aguiar, et al., 2019).

<b>Process</b>	<b>Temperature (°C)</b>	<b>S<sub>BET</sub> (m<sup>2</sup>/g)</b>	<b>V<sub>micro</sub> (cm<sup>3</sup>/g)</b>	<b>V<sub>meso</sub> (cm<sup>3</sup>/g)</b>	<b>V<sub>macro</sub> (cm<sup>3</sup>/g)</b>
Hydrothermal	190	14.2089	0.0836	0.0828	1.1948
Carbonization	240	14.9601	0.1023	0.1362	1.5375
Pyrolysis	450	4.8241	0.0002	0.0438	0.9056
	600	4.6717	0.0004	0.0371	0.6535

Biochar with higher carbon contents were produced by hydrothermal carbonization as compared to pyrolysis and gasification process (Wang and Wang, 2019). This was caused by higher retention of volatile matter that mainly composed of organic compounds during hydrothermal carbonization process at relatively low temperature as observed in Table 3.4. Dehydration and

decarboxylation processes resulted in decreasing H, O contents in hydrochar and increasing hydrophobicity. Loss of hydroxyl, carboxyl and carbonyl functional groups, hydrolysis of ester and ether bonds and condensation reactions lead to increase of aromaticity and loss of polarity at higher temperature. Therefore, pyrolysis biochar was more stable with stronger aromatic structure while hydrochar was richer in aliphatic structures (Aguiar, et al., 2019). In addition, higher amounts of inorganic compounds removal and dissolved in water reduced the ash concentration of hydrochar (Jian, et al., 2018).

Table 3.4: Proximate and elemental analysis of hydrochar and pyrolysis biochar with rice husk as a raw material (Jian, et al., 2018).

<b>Process</b>	<b>Temperature (°C)</b>	<b>C (wt%)</b>	<b>H (wt%)</b>	<b>O (wt%)</b>	<b>Volatile Matter (wt%)</b>	<b>Ash (wt%)</b>
Hydrothermal	220	66.3	5.0	26.4	55.0	3.1
Carbonization	240	71.2	5.0	21.3	51.8	2.5
	260	73.3	4.9	19.0	47.3	2.7
Pyrolysis	350	55.0	2.8	41.2	28.3	25.9
	500	58.2	1.7	39.2	14.2	33.7
	650	60.3	0.4	38.8	10.4	36.0

Hydrothermal carbonization tends to form organic acids which caused the hydrochar to be acidic with lower pH (Weber and Quicker, 2018). The organic acids produced were adsorbed onto the hydrochar surface and the pH value of hydrochar was ranged from 4.7 to 5.4 with increasing temperature according to previous work of Jian, et al. (2018). Some alkaline compounds from the feedstocks could dissolve in water and vaporize which further reduce the pH of hydrochar. Lower content of soluble salts removed by water provides lower electrical conductivity of hydrochar whereby most of the exchangeable cations such as sodium, potassium and magnesium dissolved in water during hydrothermal carbonization process. Reduction of oxygen-containing functional groups and exchangeable cations indicated a decrease of cation exchange capacity of hydrochar (Aguiar, et al., 2019).

### 3.1.4 Microwave Heating

Microwave is an alternative way of heating biomass for biochar preparation in complement to pyrolysis or gasification process. Microwave allowed rapid, uniform and selective heating of biochar through microwave irradiation without physical contact of raw biomass and energy sources. Microwave irradiation supplied even distribution of heat from the depth to the surface of feedstocks by electromagnetic wave without resistance from fluid medium that limits the heat transfer rate. A wide range of microwave power output and heating time can be applied which affecting the heating rate and properties of biochar. The most commonly applied microwave heating process was microwave-assisted pyrolysis (MWP). Biochar obtained by microwave pyrolysis composed of stable aromatic and elemental carbon, retained organic compound and polar functional groups with low density and high porous structure (Wahi, et al., 2017).

Microwave heating was a dielectric heating occurred at frequencies ranging from 1-100 GHz by converting electromagnetic energy to thermal energy. Lower microwave frequencies and higher temperature increased the depth of penetration to provide heating. The heating mechanism was affected by dipolar and interfacial polarization effects. Dipolar polarization is the rotation and alignment of polar molecules in permanent and induced dipoles at definite frequency. Thermal energy relied on the kinetic energy generated by rotational, vibrational and translational movement of valence electrons arising from the friction and collision of polar molecules. It was a cost and energy saving method where pre-treatment of biomass can be avoided (Li, et al., 2016).

It was known that high temperature favours the production of liquid and gaseous products rather than biochar. MVP occurred at lower temperature than conventional pyrolysis due to its higher energy efficiency indicating higher amounts of retained H, O and volatile components. Incomplete carbonization in MVP with higher H/C and O/C ratio resulted in biochar which was less aromatic and less stable. In contrast, MVP formed products with higher biochar yield than conventional pyrolysis and it was reduced with increasing power supplied as shown in Table 3.5. Higher microwave power removed greater amounts of volatile components by dehydration, decarboxylation and cyclization with removal of water, carboxyl group and formation of new bonds for ring compounds which resulted in higher aromaticity (Haeldermans, et al., 2019).

Table 3.5: Elemental composition, ash and biochar yield produced by microwave pyrolysis and conventional pyrolysis under different operating condition (Haeldermans, et al., 2019).

<b>Process</b>	<b>Power/ Temperature</b>	<b>C (%)</b>	<b>H (%)</b>	<b>O (%)</b>	<b>Biochar yield (%)</b>	<b>Ash (%)</b>
Microwave pyrolysis	750W	61.2	5.28	28.1	44.3	2.9
	1000W	61.0	5.27	28.1	44.5	3.0
	1250W	58.9	5.21	30.6	43.8	2.9
Conventional pyrolysis	350°C	80.88	3.40	5.60	28.4	5.2
	450°C	80.34	2.91	7.20	27.0	5.0

Biomass that contained high moisture and inorganic compounds tends to have higher microwave absorption capacity (Li, et al., 2016). High moisture contents of raw biomass were unfavourable for conventional pyrolysis where water with high heat capacity would absorb the energy and lower the heating rate. Thus, microwave heating vaporized the water and volatile organic contents to improve the porous structure of biochar. It was more energy efficient that aids in volatilization of volatile compounds at lower temperature. Higher power output of microwave provided faster heating rate to speed up the rate of dehydration. As stated by Wahi, et al. (2017), MWP increased the surface area of biochar by 70.18% after higher removal rate of volatile components. Degradation temperatures of cellulose and hemicellulose were reduced by 54% and 32% respectively compared to conventional pyrolysis (Wahi, et al., 2017).

Microwave absorbers (MVA) could be added into raw biomass to improve products yield, energy efficiency and pyrolysis temperature at lower power input. Microwave absorbers were essential because biomass was a weak microwave absorber. MVA was considered as a catalyst used to accelerate the rate of reaction by lowering the activation energy. It was classified into metal-based and carbon-based absorbers. Metal-based MVA consist of metal, metal oxides and metal hydroxides which include iron, magnesium oxide, potassium hydroxide and potassium carbonates. The vapor and gases released from biochar came into contact with heated metallic absorbers for secondary reactions by cracking to improve heating rate, affecting the product yield and quality.

Moreover, carbonaceous materials for example activated carbon, graphite and silica carbide were also used to promote heating rate and improve temperature with lower power input due to higher dielectric lost tangent parameter. Dielectric lost tangent parameter was a representation of the electromagnetic energy dissipated into heat to evaluate the microwave energy absorption capacity. Carbon-based absorbers were preferable where it can easily mix with biomass owing to similar properties such as density as well as size distribution and it brought less environmental issue than metallic elements (Li, et al., 2016).

### **3.2 Synthesis of Biochar Composites**

The preparation of biochar composites involved pre-treatment and post-treatment processes on biochar. The loading of materials could be done by either treating the raw materials of biochar before pyrolysis process or impregnation on a pre-existing biochar. There were many experiments conducted by researchers to study on the efficiency of biochar composites prepared in different conditions in removal of wastewater contaminants. The synthesis of biochar composites loaded with carbonaceous materials, nano-zero valent iron, metal or metal oxide nanoparticles and polymer were determined.

#### **3.2.1 Carbonaceous Material/ Biochar Composites**

The preparation method of CNT/ biochar nanocomposite and g-C<sub>3</sub>N<sub>4</sub>/ biochar composite under studied were different where the CNT/ biochar composite was prepared by pre-treatment of biochar feedstocks with CNT suspensions while the biochar was first prepared before the impregnation of g-C<sub>3</sub>N<sub>4</sub>. The feedstocks and pyrolysis conditions of each biochar preparation were different as well.

For the preparation of CNT/ biochar nanocomposite conducted by Inyang, et al. (2014), the feedstocks consist of dried and milled hickory chips and sugarcane bagasse biomass with 500  $\mu$ m size fraction were pre-treated by a dip-coating procedure. 10 g of each feedstocks were put in 100 ml of CNT suspensions prepared from the mixing of 20 mg (0.01 wt%) or 2 g (1 wt%) of CNT powder and 200 ml of deionized water depended on the desired weight percent that were then sonicated in ultrasound homogenizer at 20 kHz for 1 h. The mixtures were stirred at 500 rpm for 1 h before the treated feedstocks were

removed and oven-dried at 105°C. The mixtures were then pyrolyzed at 600°C for 1 h at 10 °C/min under N<sub>2</sub> environment. The biochar products were rinsed with deionized water for several times and oven-dried before it was used to conduct experiments (Inyang, et al., 2014).

According to the study conducted by Li, et al. (2019), the biochar was prepared from waste *Camellia oleifera* shells where ultrasonic crusher was used to mix 1.6 g of the feedstock powder and 0.4 g of phloroglucinol in 60 mL of water for 1 h. It was then stirred at room temperature for 6 h and heated at 230°C for 24 h with heating rate of 1°C/ min. Centrifugation and drying was done at 60°C for 24 h, followed by annealing at 650°C for 2h with heating rate of 5°C/ min. KOH was added to the annealed carbon at a ratio of 2:1 in a water-containing beaker to be stirred for 3 h and dried at 60°C in oven. Biochar was formed by calcination at 850°C for 2 h with heating rate of 5°C/ min under argon atmosphere and washed with water to obtain neutral pH.

g-C<sub>3</sub>N<sub>4</sub>/ biochar composite was prepared by 40, 80, 160 and 240 mg of biochar and 1.6 g of melamine which dispersed in 60 mL of water for 30 min and stirred for 6 h. The water was evaporated at 80°C while the mixture was calcinated at 500°C for 2 h with heating rate of 5°C/ min under argon atmosphere. The final g-C<sub>3</sub>N<sub>4</sub> nanosheets/ biochar composite were obtained by further calcination for 1 h under air atmosphere with same operating condition as demonstrated by Li, et al. (2019).

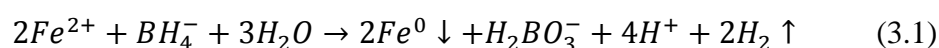
### **3.2.2 Nano-zerovalent Iron/ Biochar Composites**

The nZVI/ biochar composites applied to Cr(VI) removal involved several modifications by calcium alginate (CA), carboxymethyl cellulose (CMC), silicon (Si) and sulfide (S). Most of the nZVI/ biochar composites were prepared by impregnation method of pre-existing biochar derived from various kinds of feedstocks under different operating conditions.

The biochar was prepared from willow residues that were washed and oven dried at 80°C, followed by pyrolysis at 700°C for 2 h which was then milled and sieved to 0.154 mm according to Zhu, et al., 2018. Besides that, the powdered and 80°C oven-dried wheat bran was pyrolyzed at 500°C with a heating rate of 15 °C/min for 3 h to produce biochar in the study of Wan, et al.

(2019). The biochar was then rinsed by deionized water, dried for 8 h and filtered by a 0.25 mm sieve. Based on the study conducted by Zhang, et al. (2019), biochar was prepared from wheat straw by pyrolysis at 600°C for 2 h with limited oxygen supply. It was treated with 1M hydrochloric acid (HCl) for 12 h and washed with distilled water to obtain neutral pH. Similarly, the biochar produced from rice straw at 300, 500 and 700°C were treated in 1 mol/L HCl solution for 4 h and centrifuged to remove supernatant according to Qian, et al. (2019) while herbal residue was pyrolyzed at 400°C for 3 h before it was washed with 0.1 mol/L HCl as stated by Gao, et al. (2018). The pyrolysis processes were conducted under an inert atmosphere with in flow of N<sub>2</sub>.

Impregnation of nZVI could be done by mixing of biochar with iron sulfate or iron chloride solution. 18.9 g of biochar was dissolved in 250 mL of 0.27 mol/L FeSO<sub>4</sub> solution and 2 mL of polyethylene glycol and agitated for 60 min, followed by dropwise addition of 250 mL of 0.54 mol/L NaBH<sub>4</sub> solution and continued agitated for 40 min as demonstrated by Zhu, et al. (2018). The chemical reaction between the reagents added to biochar was shown in equation (3.1). Based on Qian, et al. (2019), 1 g of FeSO<sub>4</sub>·7H<sub>2</sub>O and 0.05 g of biochar were mixed with 50 mL of distilled water and agitated at 150 rpm and 25°C for 24 h. 100 mL of 0.5 mol/L of KBH<sub>4</sub> solution was added dropwise under stirring.



Both of the iron (II) chloride and iron (III) chloride were applicable for impregnation of nZVI on the surface of biochar. 4.41 g of FeCl<sub>3</sub>·6H<sub>2</sub>O was dissolved in 100 mL of deionized water and adjusted to pH 5.0 by using dilute 0.1 M NaOH and 0.1 M HNO<sub>3</sub>. 1.0 g of biochar was then added and agitated for 1 h at 25°C and 160 rpm with the solution. 0.05 M NaBH<sub>4</sub> solution was also added dropwise under inert atmosphere to achieve molar mass ratio of 4:3 (FeCl<sub>3</sub>·6H<sub>2</sub>O: NaBH<sub>4</sub>) and stirred vigorously to form nZVI (Wan, et al., 2019). The methods were similar to application of FeCl<sub>2</sub>·4H<sub>2</sub>O where 2 g of biochar was dispersed in the solution with continuous bubbling of N<sub>2</sub> under vigorous stirring for 2 h, followed by dropwise addition of 500 mL of 0.6 mol/L NaBH<sub>4</sub> solution (Gao, et al., 2018).

The CMC-stabilized nZVI supported by biochar (CMC-nZVI/ biochar) was prepared by which deionized water purged with purified N<sub>2</sub> for 30 min was first added to 2.74 g of FeSO<sub>4</sub>·7H<sub>2</sub>O with continuous N<sub>2</sub> purging and magnetic stirring (Zhang, et al., 2019). CMC solution was added in concentration of 0%, 0.05%, 0.1% and 0.2%. 550 mg of biochar was added after 20 min of stirring. Dropwise addition of 50 mL NaBH<sub>4</sub> solution (1.85g) allowed the deposition of CMC-stabilized nZVI particles on biochar surface. The resultant mixture with equal mass ratio of biochar and nZVI was aged for 12 h after leaving 30 min with continuous N<sub>2</sub> purging. The composite was separated and freeze-dried.

Furthermore, the nZVI/ biochar composite was embedded in calcium alginate by a modified liquid phase method. The composite was added into the solution of sodium alginate dissolved in deionized water to the mass ratio of 4:1 (nZVI/ biochar:alginate). 50 mL of the mixture was added dropwise into 200 mL 0.1 M CaCl<sub>2</sub> solution with 5 mL ethyl acetate. Slow agitation was done at 25°C for 3 h to solidify the composite and rinsed with deionized water (Wan, et al., 2019). In the case of sulfide-modified nZVI/ biochar composite, sodium dithionite solution (18.75 mmol/L) was added to obtain S/ Fe molar ratio of 0.25 (Gao, et al., 2018).

### 3.2.3 Metal or Metal Oxide Nanoparticles/ Biochar Composites

Metal compounds could be loaded on the surface of biochar by impregnation of biochar or its feedstock in a solution composed of the metal compounds. Nanoparticles were commonly studied while the preparation of biochar supported MgO, ZnO, Fe<sub>3</sub>O<sub>4</sub>,  $\alpha$ -Fe<sub>2</sub>O<sub>3</sub> and FeS nanoparticles were discussed.

Sulphuric acid treated MgO nanoparticles/ biochar composite was prepared by Xiao, et al. (2018) where the biochar was synthesized from sugarcane harvest residue (SHR) which was dried, milled and sieved into particles size <0.5 mm. 100g of the biomass was then pre-treated by 1000 mL of 0.5% sulfuric acid in a flask and shaken vigorously at 240 rpm for 2h. The solid was separated and washed with deionized water and oven-dried at 80°C for 24 h. 50g of pre-treated solid was then mixed with 1000 mL of 7.5 g/L MgCl<sub>2</sub>·6H<sub>2</sub>O and shaken for 12 h, followed by 80°C oven-dried for 48 h. Pyrolysis process was conducted at 550°C for 1 h under N<sub>2</sub> flow condition to produce MgO nanoparticles/ biochar composite.

Based on the study of Yu, et al. (2018) on ZnO/ biochar nanocomposite, the biochar was prepared from water hyacinth biomass by slow pyrolysis under argon atmosphere at different operating temperature increased from 500-800°C for 2 h with heating rate of 3°C/min. The biochar was then purified by 15% nitric acid at 40°C and stirred for 4 h. Deionized water was used to wash the biochar for neutralization and dried at 105°C for 12 h. ZnO/ biochar nanocomposite was prepared by impregnation of biochar powder into zinc nitrate ( $\text{Zn}(\text{NO}_3)_2$ ) solution and dried at 105°C for another 12 h. Calcination was done at 380°C for 3 h under  $\text{N}_2$  atmosphere to obtain ZnO/ biochar nanocomposite.

To prepare magnetite ( $\text{Fe}_3\text{O}_4$ )/ biochar composite, 25 g of rice husk was mixed with 2.5 g of solid  $\text{FeSO}_4$  powder, milled and transferred into a silicon carbide vessel as an excellent microwave absorber in a microwave oven for copyrolysis at 1 kW for 30 min under limiting oxygen condition. The biochar was pre-treated by 0.1 M HCl to remove impurities such as alkali-metal salts and washed with deionized water to obtain pH about 4.5. Then, the biochar was dried in a vacuum oven and passed through a 0.149 mm sieve (Zhong, et al., 2018).

In contrast, the  $\alpha\text{-Fe}_2\text{O}_3$  nanoparticles/ biochar composite was prepared by using rosin as the feedstock as demonstrated by Liu, et al. (2019). 6 g of  $\text{FeCl}_3 \cdot 6\text{H}_2\text{O}$  was dissolved in 15 mL of deoxygenated water while  $\text{NH}_4\text{OH}$  solution was dropped slowly into the solution to adjust the pH to value of 8. 4 g of rosin dissolved in 20 mL of anhydrous ethanol was dropped into the solution under stirring for 30 min. The solvent was first evaporated, followed by heating process at 400 °C for 15 min in the absence of air to obtain the nanocomposites (Liu, et al., 2019).

The biochar-supported CMC-stabilized FeS nanoparticles (CMC-FeS/biochar) composite was studied by Lyu, et al. (2017). The preparation process started by dissolving 1.75 g of  $\text{FeSO}_4 \cdot 7\text{H}_2\text{O}$  in 1000 mL of deionized water. It was then purged with purified nitrogen ( $\text{N}_2$ ) gas for 1 h to remove dissolved oxygen and added with 55 mL of CMC solution to form  $\text{Fe}^{2+}$  and CMC complexes. 550 mg of biochar was added into the mixture while dropwise addition of 45 mL of  $\text{Na}_2\text{S}$  solution (1.51 g of  $\text{Na}_2\text{S} \cdot 9\text{H}_2\text{O}$ ) was done with magnetic stirring for 30 min under  $\text{N}_2$  purging to allow attachment of FeS particles on the surface of biochar. The mixture was sealed and allowed to stay

for 24 h before it was freeze-dried. It was washed with N<sub>2</sub>-purged deionized water to remove sodium sulfate (Na<sub>2</sub>SO<sub>4</sub>) and freeze-dried again. The preparation method stated was referred to CMC-FeS/biochar composite with mass ratio of 1:1:1.

### 3.2.4 Polymer/ Biochar Composites

Impregnation of polymers on biochar was commonly done by mixing a pre-existing biochar into a solution composed of the polymers. The preparation methods of biochar supported polypyrrole and polyethylenimine composites were identified.

Based on the study conducted by Yang, et al. (2018), the biochar was synthesised from corncobs magnetically treated by iron. 5g of corncob powder was mixed with 50 mL solution of 1 mol/L iron nitrate (Fe(NO<sub>3</sub>)<sub>3</sub>) and 20 wt% of nitric acid (HNO<sub>3</sub>) at room temperature. It was magnetically stirred for 12 h and dried at 105 °C before pyrolysis process at 600 °C for 2h. Oxidative polymerization of Py monomers was conducted in the presence of the biochar by FeCl<sub>3</sub>. 1.2 g of biochar was mixed with 0.867 mL of Py and 100 mL of deionized water at 30°C for 0.5 h and shaken at the rate of 150 r/min. The FeCl<sub>3</sub> solution was added dropwise by uniform shaking and continuous shaken for 24 h. The product was separated magnetically, washed and dried at 60°C to obtain magnetic PPy/ biochar composite. According to Thines, et al. (2017), the PPy/ biochar composite could also be obtained by dissolving biochar and pyrrole monomer into HCl solution while a HCl solution containing ammonium persulfate was slowly added to the suspension with constant stirring.

The pristine biochar for preparation of PEI/ biochar composite was derived from rice husk by pyrolysis at 450-500°C and treated by acid or alkali solution to remove impurities. 200 mL of 70% HNO<sub>3</sub> or 3 mol/L KOH was added to 20 g of biochar and stirred at 160 rpm for 1 h. Deionized water was used to rinse the biochar to obtain neutral pH while the biochar was then dried at 80°C for 12 h. For impregnation of PEI, the biochar was mixed with 100 mL of 10% (w/v) PEI/ methanol solution, stirred at 160 rpm and 30°C for 24 h. Then, the biochar was transferred to 200 mL of 1% (w/v) glutaraldehyde solution and agitated for 30 min for cross-linking. The PEI/ biochar composite was obtained and washed with deionized water (Ma, et al., 2014).

### 3.3 Experiments for Cr(VI) Removal

To determine the efficiency of various biochar composites on Cr(VI) removal from wastewater, batch experiments were usually carried out at room temperature. Certain amounts of adsorbents were added into the Cr(VI) solution prepared with known initial concentration and uniformly mixed by shaking. The Cr(VI) solution could be prepared by dissolving certain amounts of potassium dichromate ( $K_2Cr_2O_7$ ) into deionized water (Liu, et al., 2019). Dilution method was applied to prepare the solutions with various Cr(VI) concentrations. The operating conditions such as adsorbent dosage, initial concentration of Cr(VI), pH and residence time were also controlled to determine their effects on the removal efficiency of Cr(VI) by different biochar composites.

The pH of the solution was adjusted by acid or alkaline solutions such as nitric acid ( $HNO_3$ ), sulfuric acid ( $H_2SO_4$ ), hydrochloric acid (HCl) and sodium hydroxide (NaOH). The  $HNO_3$  was selectively applied due to its little effects on reduction of Cr(VI) (Zhang, et al., 2018). The concentrations of Cr(VI) after some time intervals were determined to identify to removal efficiency of the adsorbents by UV-Vis spectrophotometer after complexation with 1,5-diphenylcarbazide at the maximum wavelength of 540 nm (Wan, et al., 2019). Besides that, the total concentration of chromium was determined by an inductively coupled plasma-atomic emission spectrometer (ICP-AES) while the concentration of Cr(III) was calculated by the difference between the concentration of chromium and Cr(VI) (Xiao, et al., 2018).

The removal efficiency or percent of sorption (%) and adsorption capacity,  $q$  of Cr(VI) could be calculated from the equations (3.2)-(3.4) (Yu, et al., 2018; Yang, et al., 2018).

$$Removal\ Efficiency\ (\%) = \frac{(C_0 - C_t)}{C_0} \times 100\% \quad (3.2)$$

$$q_e = \left( \frac{C_0 - C_e}{m} \right) V \quad (3.3)$$

$$q_e = \left( \frac{C_0 - C_t}{m} \right) V \quad (3.4)$$

where

$C_0$  = initial concentration of Cr(VI), mg/g

$C_t$  = concentration of Cr(VI) at time, t, mg/g

$C_e$  = concentration of Cr(VI) at equilibrium, mg/g

V = volume of Cr(VI) solution, L

m = mass of adsorbent, g

Several characterization techniques were also applied to determine the characteristic of biochar composites and the mechanisms involved in Cr(VI) removal. Scanning electron microscopy (SEM), SEM-Energy Dispersive X-ray spectroscopy (SEM-EDS) and field emission scanning electron microscopy (FESEM) was used to observed the microscopic features and surface morphology of materials. The specific surface area, pore size and pore volume were measured by multipoint N<sub>2</sub>-BET (Brunauer-Emmett-Teller) adsorption method (Lyu, et al., 2017). The surface functional groups of biochar composites before and after adsorption process could be measured by Fourier transform infrared (FTIR) spectroscopy with wavenumber in the range of 400-4000 cm<sup>-1</sup>. X-ray diffraction (XRD) with Cu-  $K\alpha$  radiation and X-ray photoelectron spectroscopy (XPS) were applied to determine the crystallinity and surface elemental compositions of the composites before and after the removal process (Lyu, et al., 2017). Thermogravimetry analysis (TGA) could also conducted at a heating rate of 20 °C/min under air atmosphere to determine the thermal stability of the composites (Wan, et al., 2019).

## CHAPTER 4

### RESULTS AND DISCUSSION

#### 4.1 Characterization of Biochar Composites

The biochar composites under study were synthesized by using different methods and characterization of the composites was required to determine their physical and chemical properties that would affect the removal of Cr(VI). The results of characterization techniques such as electron microscope, multipoint N<sub>2</sub>-BET adsorption method, FTIR and XRD of different biochar composites were discussed. These were the main characterization techniques carried out on evaluation of biochar composites for Cr(VI) removal with different functions.

##### 4.1.1 Electron Microscope

The electron microscopes involved scanning electron microscopy (SEM), SEM-Energy Dispersive X-ray spectroscopy (SEM-EDS), field emission scanning electron microscopy (FESEM) and transmission electron microscope (TEM). It was the most commonly used characterization technique where fourteen among the fifteen journals being reviewed that studied about the application of biochar composites on Cr(VI) removal involved characterization by electron microscope. Electron microscopes were used to examine the morphological features of biochar composites and identify the porosity of composites that were representing the adsorption sites available for Cr(VI).

Generally, the nanostructures incorporated on biochar were observed to be distributed and dispersed on the surface of biochar where aggregation was inhibited and more adsorption sites were provided for Cr(VI) removal. Agglomeration of particles on biochar surface would result in decreased of specific surface area and the adsorption capacity. However, uptake of Cr(VI) was not limited to physical adsorption where electrostatic interaction between surface functional groups, ion exchange and magnetic properties of biochar composites very much contributed to Cr(VI) remediation too. Hence, Energy Dispersive X-Ray Spectroscopy as a chemical microanalysis technique was often used in conjunction with SEM to determine the elemental distribution of samples (Chia, et al., 2012).

The FESEM images of activated carbon supported CNT were observed to substitute the CNT/ biochar composite as shown in Figure 4.1. It can be observed that the CNTs were completely dispersed on the surface of activated carbon with diameters of 16-19 nm. The CNTs were not aligned but clumped to each other on the surface of activated carbon (Atieh, 2011). Based on Figure 4.2 (A), multi-layered of bulk  $g\text{-C}_3\text{N}_4$  which might obstruct the exposure of Cr(VI) with photogenerated electrons on the photocatalyst surface was observed. The presence of biochar aided in the dispersion of  $g\text{-C}_3\text{N}_4$  structures on the surface and the formation of bulk layered  $g\text{-C}_3\text{N}_4$  was inhibited as shown in Figure 4.2 (B) (Li, et al., 2019).

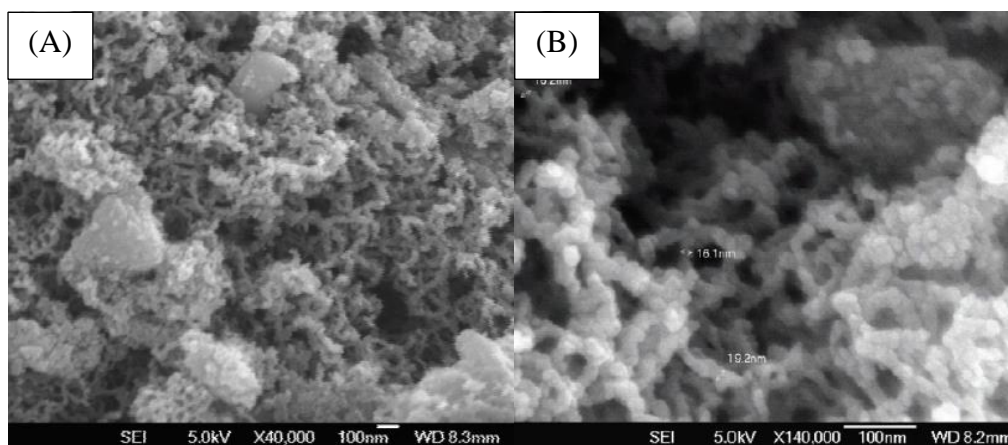


Figure 4.1: FESEM images of CNT/ activated carbon with magnification of (A) 40000x and (B) 140000x (Atieh, 2011)

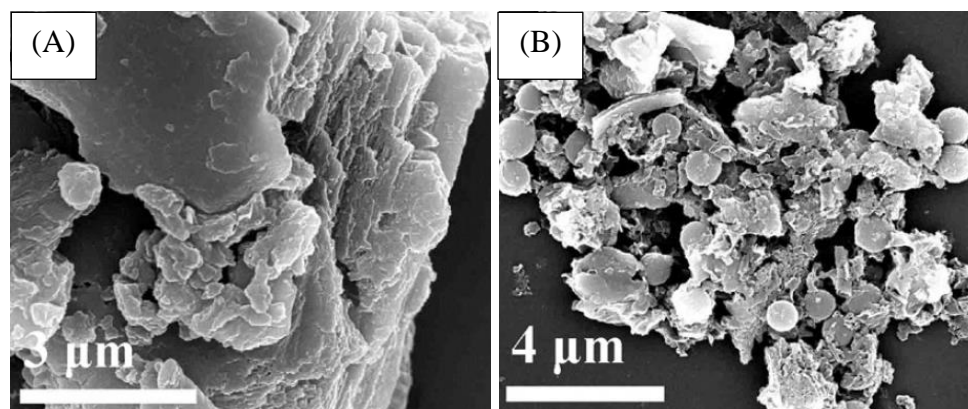


Figure 4.2: FESEM images of (A)  $g\text{-C}_3\text{N}_4$  and (B)  $g\text{-C}_3\text{N}_4$  nanosheets/ biochar (Li, et al., 2019)

nZVI/ biochar composites were modified by addition of calcium alginate (CA), carboxymethyl cellulose (CMC), silicon (Si) and sulfide (S). The SEM-EDS images in Figure 4.3 showed that the nZVI/ biochar composite was embedded in the CA beads with the Fe element detected in the composite. The nZVI/ biochar/ CA composite showed a relatively rough surface morphology as compared to the nZVI/ biochar composite which was contributed by the structure of CA. Greater amounts of Fe element was found in the inner structure of CA (18.34 wt%) than that on the outer layer (7.6 wt%) as shown in Spectrum 4 and 5 from Figure 4.3 where nZVI/ biochar was mostly entrapped inside the CA. It might be resulted from the aggregation of CA molecules on the surface with its polarity and hydrophilicity properties (Wan, et al., 2019).

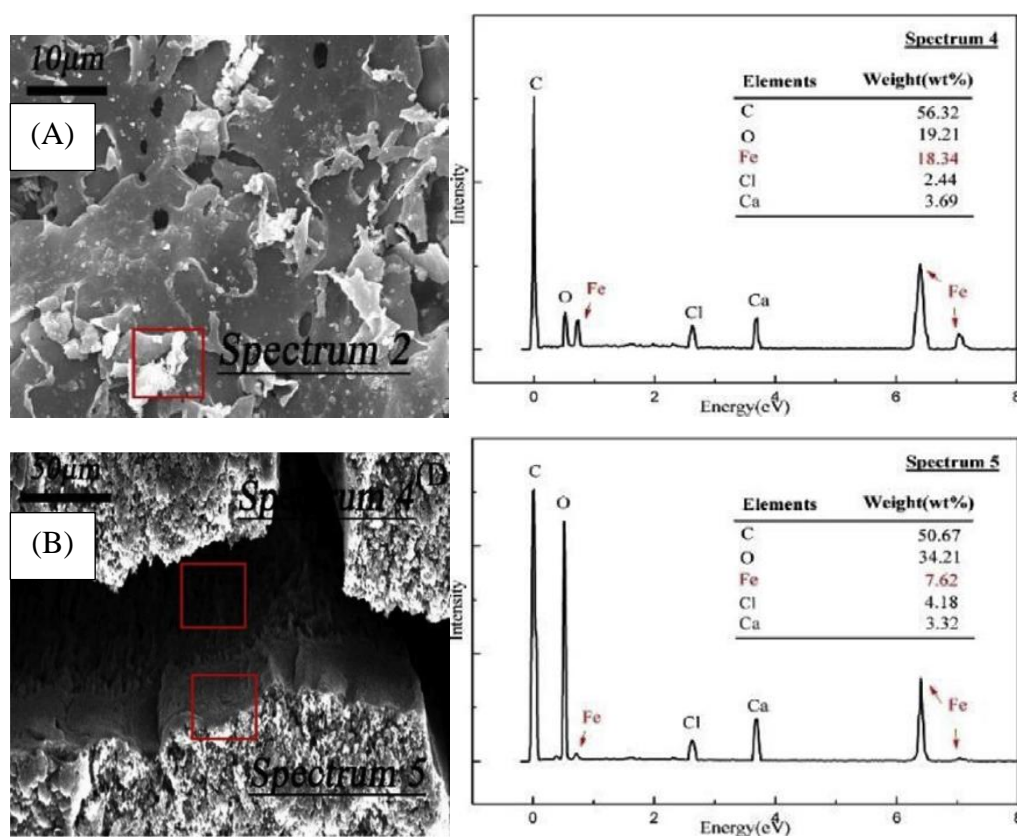


Figure 4.3: SEM-EDS images and spectra of (A) nZVI/ biochar and (B) nZVI/ biochar/ CA (Wan, et al., 2019)

Based on the experiments conducted by Zhang, et al. (2019), the addition of CMC covered the surface of nZVI particles and created smaller particles size which was less than 100 nm. This indicated that the nZVI particles were

stabilized by the CMC to prevent agglomeration. Sheet-like structures were also determined on the surface of CMC-nZVI/ biochar composite as the  $\alpha$ -Fe<sub>2</sub>O<sub>3</sub> resulted from the oxidation of nZVI other than the spherical nZVI particles (Zhang, et al., 2019). According to Qian, et al. (2019), Si served as an effective carrier for nZVI which enhanced the grafting of nZVI on biochar surface. Based on Figure 4.4, core-shell structure was observed in S-nZVI/ biochar composite with the main components of FeOOH and FeS<sub>x</sub> while the biochar segregated its structure (Gao, et al., 2018).

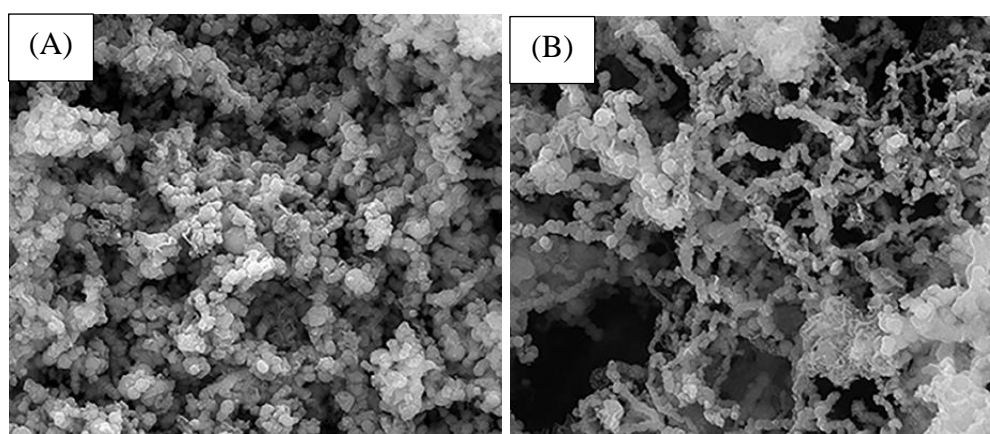


Figure 4.4: SEM images with magnification of 50000x of (A) S-nZVI and (B) S-nZVI/ biochar (Gao, et al., 2018)

The MgO particles in the experiments carried out by Zhang, et al. (2012) were in the form of nanoflakes and uniformly deposited on the surface of biochar with the thickness of 10-25 nm which allowed the surface to appear rough and porous. Besides that, ZnO nanoparticles were observed as white spots that were evenly distributed on the biochar surface with the average diameter of 28.3 nm (Yu, et al., 2018). Similarly, Fe<sub>3</sub>O<sub>4</sub>,  $\alpha$ -Fe<sub>2</sub>O<sub>3</sub> and FeS nanoparticles attached on biochar surface to give irregular surface of Fe<sub>3</sub>O<sub>4</sub>/ biochar,  $\alpha$ -Fe<sub>2</sub>O<sub>3</sub>/ biochar and FeS/ biochar composites (Wang, et al., 2019; Liu, et al., 2019; Lyu, et al., 2012). According to Liu, et al. (2019), the diameter of  $\alpha$ -Fe<sub>2</sub>O<sub>3</sub> ranged from 20-50 nm. These rough and porous surfaces tend to result in more adsorption sites. However, the PPy/ biochar particles were agglomerated with sizes ranged from 180-500 nm and appeared as loose sponge-like structure as shown in Figure 4.5.

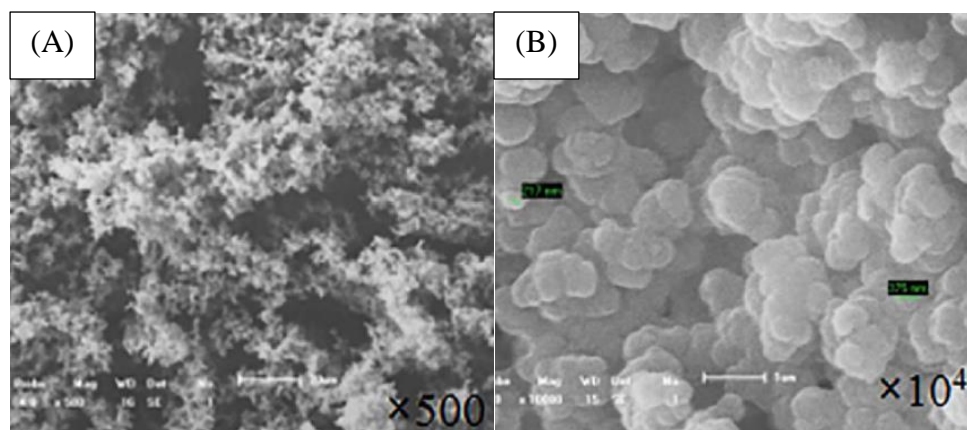


Figure 4.5: SEM images of PPy/ biochar with magnification of (A) 500x and (B) 10000x (Yang, et al., 2018)

#### 4.1.2 Multipoint N<sub>2</sub>-BET Adsorption Method

The specific surface area, total pore volume and pore size distribution of the biochar composites were determined by the multipoint N<sub>2</sub>-BET adsorption method. It was found to be conducted in twelve journals being reviewed that studied the application of biochar composites in Cr(VI) remediation. It was an important characterization technique to be conducted to determine the specific surface area of an adsorbent which was one of an significant factor contribute to Cr(VI) removal. However, the removal of Cr(VI) was affected but not limited to the specific surface area of biochar composites. Higher specific surface area favoured Cr(VI) adsorption by providing more adsorption sites on the surface of biochar composites. Table 4.1 showed the summarization on the results of BET method carried out on various biochar composites. Besides than the addition of foreign particles, the specific surface area was also affected by the raw biochar used in composites synthesis.

Generally, the specific surface area of biochar decreased by entrapment of other active components within its porous structures where pore blockage of biochar occurred. In turn, biochar aided in segregation of nanoparticles within its carbon matrix to increase their specific surface area by inhibiting agglomeration. However, CNT and MgO modified biochar composites showed an increased in surface area which might be resulted by the attachment of the nanosized particles on biochar surface and gave rise to a rough surface. The small g-C<sub>3</sub>N<sub>4</sub> particles blocking the pores of biochar significantly reduced its specific surface area from 1413 m<sup>2</sup>/g to 327 m<sup>2</sup>/g while substantial occupation

of  $\alpha$ -Fe<sub>2</sub>O<sub>3</sub> nanoparticles created smooth surface with low specific surface area of 5.03 m<sup>2</sup>/g (Li, et al., 2019; Liu, et al., 2019). The pore volume of the acid treated MgO/ biochar composite was relatively high due to the loss of impurities such as K, Ca, P and S to form more cracks and erratic structures (Xiao, et al., 2018).

Table 4.1: Specific surface area and pore volume of various biochar composites

Composite	Specific surface area		Pore volume	References
	(m <sup>2</sup> /g)			
	Biochar	Composite	(cm <sup>3</sup> /g)	
CNT/ biochar	289	352	0.138	Inyang, et al. (2014)
g-C <sub>3</sub> N <sub>4</sub> / biochar	1413	327	-	Li, et al. (2019)
Si-nZVI/biochar	97.8	34.1	-	Qian, et al. (2019)
MgO/ biochar	27.9	136.2	0.120	Xiao, et al. (2018)
• H <sub>2</sub> SO <sub>4</sub> -treated		147.6	3.680	
ZnO/ biochar	769.4	469.6	0.187	Yu, et al. (2018)
Fe <sub>3</sub> O <sub>4</sub> / biochar	162.3	92.8	0.112	Wang, et al. (2019)
$\alpha$ -Fe <sub>2</sub> O <sub>3</sub> / biochar	-	5.03	-	Liu, et al. (2019)
FeS/ biochar	215.7	51.5	-	Lyu, et al. (2017)
PPy/ biochar	835	474.8	-	Thines, et al. (2017)

Although pristine biochar had higher specific surface area, biochar composites showed better performance on Cr(VI) removal than that of pristine biochar. This indicated that the active components loaded on biochar had greater contribution in Cr(VI) adsorption as compared to specific surface area. For instance, biochar composite loaded with 30 wt% ZnO achieved 87.1% of Cr(VI) adsorption with lower specific surface area of 469.6 m<sup>2</sup>/g which was greater than that of pristine biochar with only 50% of sorption with higher specific surface area of 769.4 m<sup>2</sup>/g (Yu, et al., 2018). The results suggested that the interactions between ZnO and Cr(VI) ions were more effective than the adsorption of Cr(VI) on adsorption sites provided by specific surface area of biochar.

### 4.1.3 Fourier Transform Infrared Spectroscopy (FTIR)

FTIR was also carried out to characterize biochar composites for Cr(VI) removal in thirteen journals under reviewed. The results of FTIR analysis were analysed to determine the surface functional groups of biochar composites which might contribute to Cr(VI) removal. In addition, Raman spectroscopy serves as a complementary technique to FTIR which is used to identify the chemical structure of a material. As discussed previously, interactions between adsorbent surface functional groups and chromium compounds were fundamental to the adsorption process while the removal mechanisms were also dependent on the functional groups available. Basically, cations were responsible for electrostatic attraction of Cr(VI) anions and Cr(III) cations exchange where anions contributed to the uptake of Cr(VI) by anion exchange. Besides, oxygen-containing functional groups tend to form complexation with chromium compounds and aided in the removal process too.

According to the Raman spectra in Figure 4.6, the disorder mode D-band at about  $1350\text{ cm}^{-1}$  was originated from defects and functional groups such as OH, C=O, COOH while the tangential mode G-band at  $1500\text{-}1600\text{ cm}^{-1}$  was induced by the carbon stretching in crystalline graphitic materials. The Raman intensity,  $I_D/I_G$  ratio increased from 1.11 to 1.30 upon incorporation of CNTs with increased functionalities (Inyang, et al., 2014). The FTIR spectra in Figure 4.7 showed that g- $\text{C}_3\text{N}_4$  provided more functional groups to biochar surface with several additional peaks. The sharp peak at  $815\text{ cm}^{-1}$  represented the bending of s-triazine units of g- $\text{C}_3\text{N}_4$  structures while the peaks in between  $845\text{-}1904\text{ cm}^{-1}$  were attributed to the C-N and C=N stretching. The broad absorption peak centred at  $3185\text{ cm}^{-1}$  represented the stretching of  $\text{-NH}_2$  and  $\text{=NH}$  amine groups (Li, et al., 2019).

For biochar impregnated with nZVI as shown in Figure 4.8 (A), the peaks at  $3412$ ,  $1683$  and  $1045\text{ cm}^{-1}$  were decreased due to the bonding of nZVI with -OH. Addition of CA into the nZVI/ biochar composites resulted in greater peaks at  $3412$ ,  $1683$  and  $1045\text{ cm}^{-1}$  which were assigned to the higher amounts of OH, C-O and COOH groups. The Raman spectrum of nZVI/ biochar in Figure 4.8 (B) showed several peaks at  $223$ ,  $292$ ,  $398$ ,  $486$  and  $682\text{ cm}^{-1}$  which referred to  $\alpha\text{-Fe}_2\text{O}_3$ ,  $\text{Fe}_3\text{O}_4$  and the consumption of -OH to form FeOOH (Wan, et al., 2019).

Similarly, the absorption band of Fe-O bond was identified at around  $465\text{ cm}^{-1}$  for CMC-nZVI/ biochar composite given by Figure 4.9 (A). The oxygen-containing functional groups from CMC were discovered on the composites surface with the absorption bands at  $1060, 1320, 1590\text{ cm}^{-1}$  that were assigned to C-O, O-C=O, C=O and OH stretching (Zhang, et al., 2019). The absorption bands of Si-O-Si at  $1100-1000, 880-780$  and  $470\text{ cm}^{-1}$  disappeared after incorporation of nZVI proved that Si is responsible for the uptake of nZVI as shown in Figure 4.9 (B) (Qian, et al., 2019).

According to Xiao, et al. (2018), stronger peak of FTIR spectra was observed at  $3326\text{ cm}^{-1}$  corresponding to the Mg-OH stretching. Additional peaks at around  $443\text{ cm}^{-1}$  was observed in FTIR spectrum of ZnO/ biochar in Figure 4.10 which were denoted to the stretching of Zn-O bonds (Yu, et al., 2018). There existed a characteristic peak at  $560\text{ cm}^{-1}$  in the FTIR spectrum of  $\text{Fe}_3\text{O}_4$ / biochar composite that was associated with Fe-O stretching mode (Wang, et al., 2019). Based on the experiments conducted by Lyu, et al. (2017), the absorption peaks of CMC-FeS/ biochar composite occurred at  $3424, 1611, 1447, 1148$  and  $817\text{ cm}^{-1}$  were attributed to -OH, C=O, O=C-O, C-O and Si-O groups which involved in incorporation of FeS onto biochar surface due to the shifting of absorption bands.

For PPy/ magnetic biochar, the peaks at  $611$  and  $3421\text{ cm}^{-1}$  represented the Fe-O and -OH groups on the surface of  $\text{Fe}_3\text{O}_4$  while the peaks at  $875, 1045, 1180$  and  $1348\text{ cm}^{-1}$  were assigned to the C-H deformation, stretching vibration, in-plane vibration and C-N stretching of PPy respectively given by Figure 4.11 (Yang, et al., 2018). New peaks were observed for FTIR spectrum PEI/ biochar composite at  $2930, 2849, 1653, 1439$  and  $1379\text{ cm}^{-1}$  that were represented to C-H stretching in -CH and - $\text{CH}_2$ , C=N or C=O bonds stretching and C-N stretching respectively (Ma, et al., 2014).

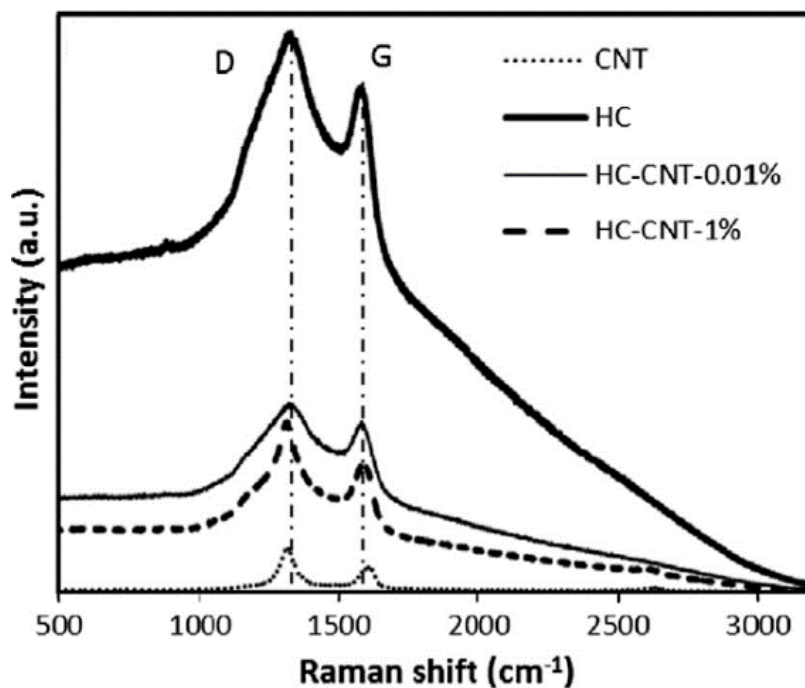


Figure 4.6: Raman spectra of CNT/ biochar composites and (Inyang, et al., 2014)

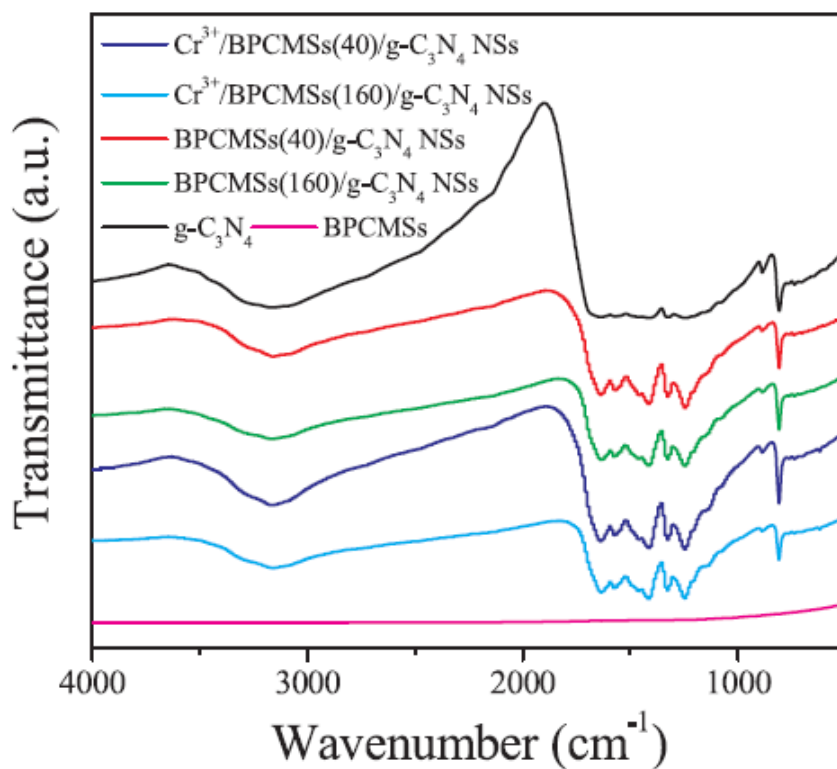


Figure 4.7: FTIR spectra of g-C<sub>3</sub>N<sub>4</sub>/ biochar composites (Li, et al., 2019)

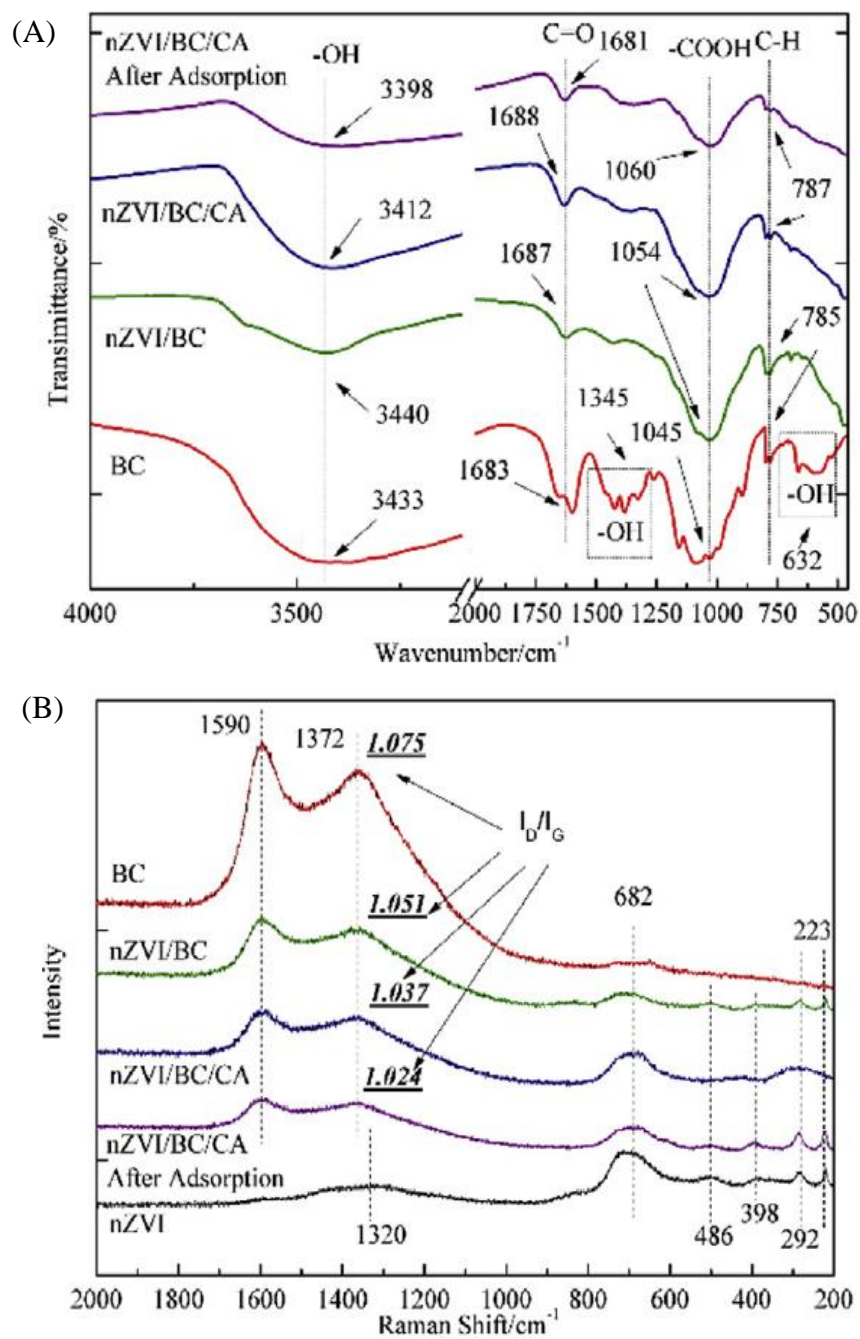


Figure 4.8: (A) FTIR spectra and (B) Raman spectra of nZVI/ biochar composites (Wan, et al., 2019)

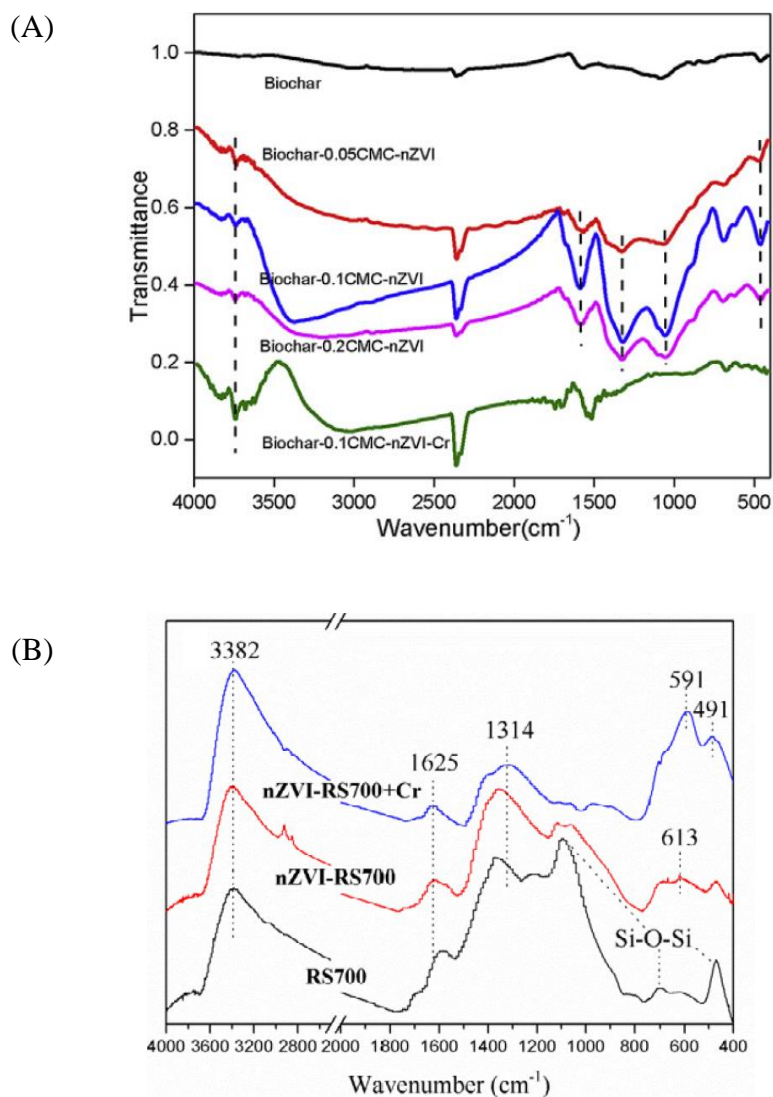


Figure 4.9: FTIR spectra of (A) CMC-nZVI/ biochar composites and (B) nZVI/ Si-rich biochar composites (Zhang, et al., 2019; Qian, et al., 2019)

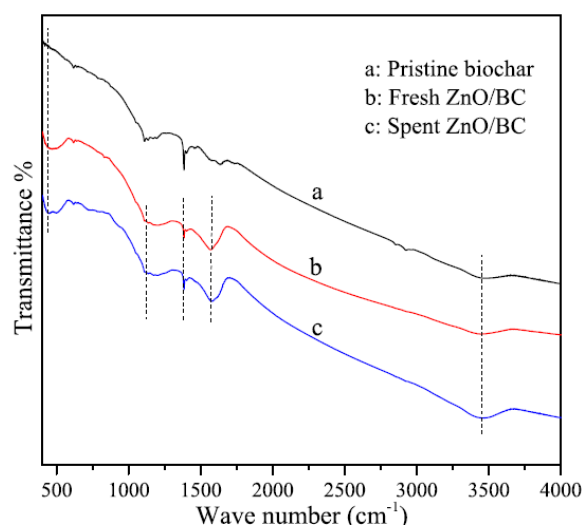


Figure 4.10: FTIR spectra of ZnO/ biochar composites (Yu, et al., 2018)

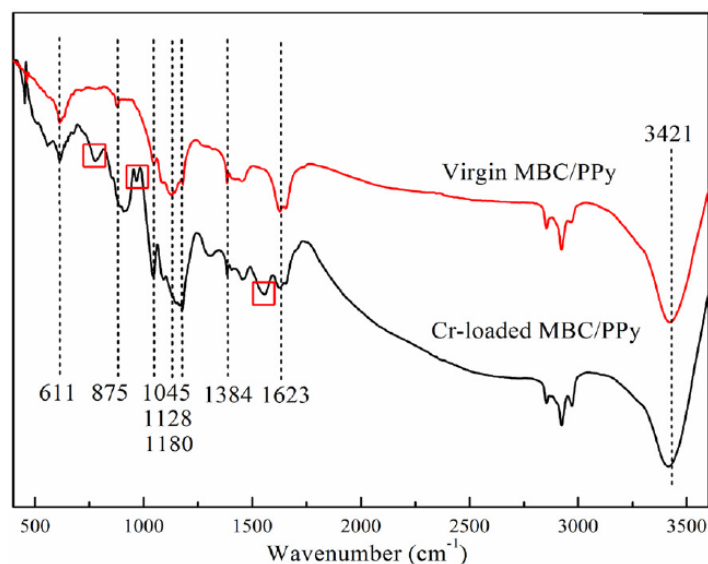


Figure 4.11: FTIR spectra of PPy/ magnetic biochar composites (Yang, et al., 2018)

#### 4.1.4 X-Ray Diffraction (XRD) & X-Ray Photoelectron Spectroscopy (XPS)

XRD characterization was conducted in eleven out of fifteen journals reviewed on evaluation of biochar composites in Cr(VI) remediation. The results of XRD were discussed to identify the crystallinity and composition of the composites. Since the XRD is only applicable to crystalline sample, thus the XRD peaks of amorphous biochar cannot be observed. XRD was suggested to be carried out with FTIR where such combination was able to reveal exact composition of samples with adequate accuracy. In contrast, XPS was often conducted in complementary to XRD to examine the chemical composition on the adsorbents surface.

The interlayer distance of  $g\text{-C}_3\text{N}_4$  was 0.33 nm and the reduction of diffraction peaks by introduction of biochar in  $g\text{-C}_3\text{N}_4$ /biochar composite in Figure 4.12 showed that the formation of bulk layered  $g\text{-C}_3\text{N}_4$  was inhibited (Li, et al., 2019). Based on Figure 4.13, the peak at  $44.7^\circ$  was attributed to nZVI and the peaks at  $31.76^\circ$ ,  $45.52^\circ$ ,  $57.08^\circ$  and  $62.72^\circ$  were attributed to  $\text{Fe}_3\text{O}_4$ . The increased of intermolecular spacing and non-crystallinity were determined by the decreased diffraction peaks after incorporation of biochar and CA (Wan, et al., 2019).

For XRD pattern of CMC-nZVI/ biochar composite in Figure 4.14, the peaks at  $22.8^\circ$  and  $44.6^\circ$  were attributed to cellulose and  $\alpha\text{-Fe}^0$  respectively (Zhang, et al., 2019). In contrast, narrower and sharper peak of nZVI is observed in Figure 4.15 whereby the Si-rich biochar increased the crystallinity of  $\text{Fe}^0$  due to the release of  $\text{SiO}_2$  by biochar (Qian, et al., 2019). The intensity of the XRD peak corresponded to Fe as shown in Figure 4.16 was insignificant due to the shielding effects of FeS on the surface of S-nZVI/ biochar composite (Gao, et al., 2018).

The MgO crystallite formed in MgO-coated biochar was identified by the peak at  $37.1^\circ$ ,  $43.1^\circ$ ,  $62.5^\circ$ ,  $74.7^\circ$  and  $78.6^\circ$  in the XRD spectrum (Xiao, et al., 2018). The diffraction peaks of ZnO and  $\text{SiO}_2$  were observed in the XRD spectrum of ZnO/ biochar composite as demonstrated in Figure 4.17 (Yu, et al., 2018). Besides, several peaks attributed to  $\alpha\text{-Fe}_2\text{O}_3$  as labelled were found in the XRD spectrum of  $\alpha\text{-Fe}_2\text{O}_3$ / biochar composite given by Figure 4.18 (Liu, et al., 2019). Based on Figure 4.19, biochar exhibited a diffraction peak at  $22^\circ$  with interlayer distance of 0.41 nm corresponding to -OH, O=C-O and C-O groups. The presence of FeS in biochar composite was determined by the diffraction peaks at  $27.0^\circ$ ,  $31.9^\circ$ ,  $34.3^\circ$ ,  $38.0^\circ$ ,  $46.4^\circ$ ,  $52.8^\circ$ ,  $59.2^\circ$  and  $64.1^\circ$  while the presence of  $\text{Fe}_3\text{O}_4$  with peaks at  $18.7^\circ$ ,  $22.8^\circ$ ,  $23.6^\circ$  and  $25.8^\circ$  was attributed to the partial oxidation of FeS (Lyu, et al., 2017).

Figure 4.20 (A) shows the diffraction peaks of  $\text{Fe}_3\text{O}_4$  presence in the magnetic biochar while the addition of PPy with amorphous phase exhibited a broad peak at  $23^\circ$  in Figure 4.20 (B) associated with the peaks of  $\text{Fe}_3\text{O}_4$  (Thines, et al., 2017). It was observed that the atomic ratio of C:N:O of biochar surface which was measured by XPS shifted from 90:2.3:6.7 to 54:28:17 after incorporation of PEI. The significant increased of N and O and decreased of C contents was denoted to the crosslinking reaction of PEI with biochar surface (Ma, et al., 2014).

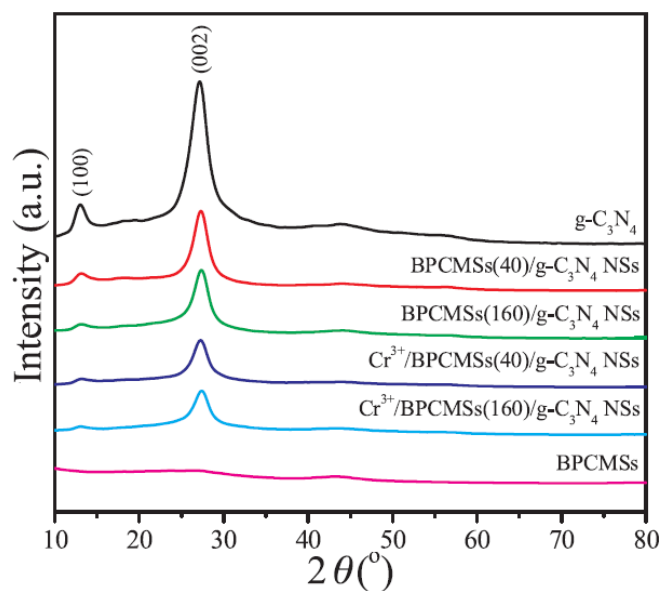


Figure 4.12: XRD patterns of  $g\text{-C}_3\text{N}_4$ / biochar composites (Li, et al., 2019)

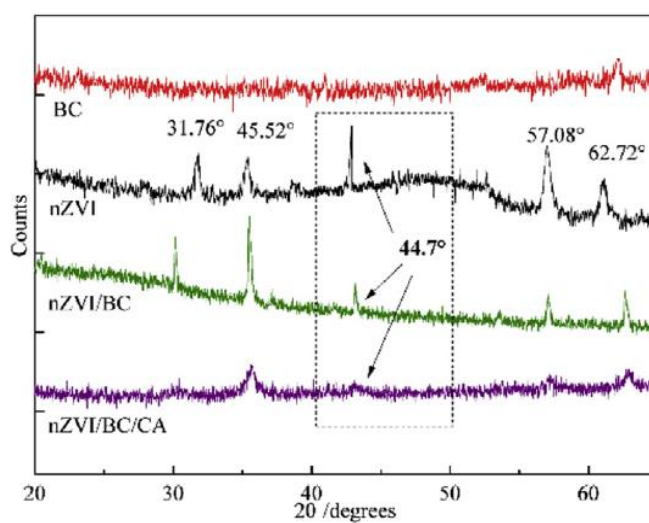


Figure 4.13: XRD patterns of CA-nZVI/ biochar composite (Wan, et al., 2019)

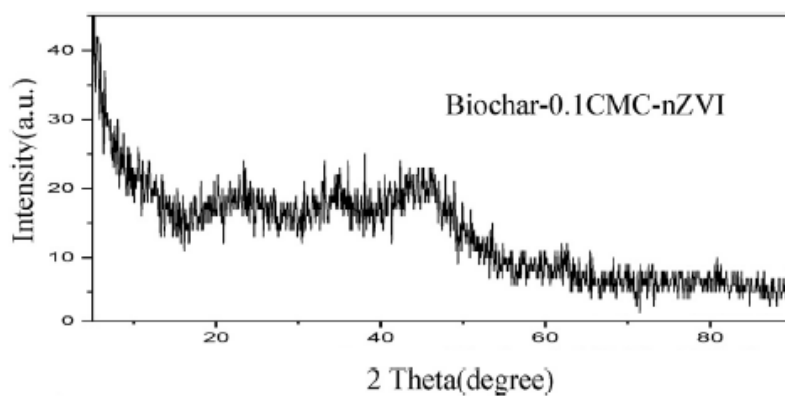


Figure 4.14: XRD pattern of CMC-nZVI/ biochar composites (Zhang, et al., 2019)

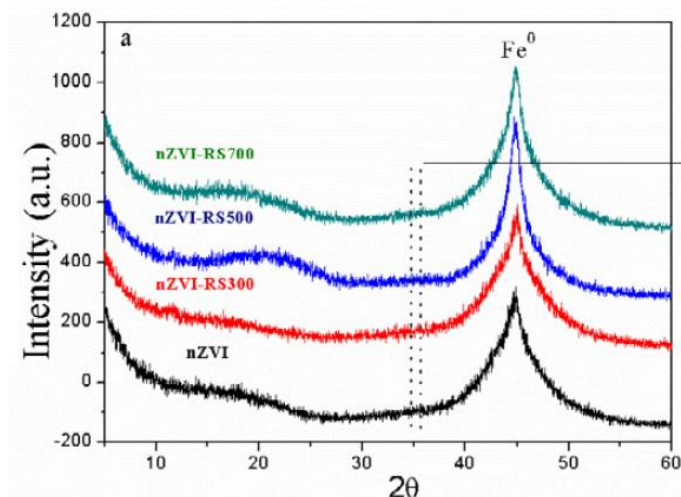


Figure 4.15: XRD patterns of nZVI/ Si-rich biochar composites (Qian, et al., 2019)

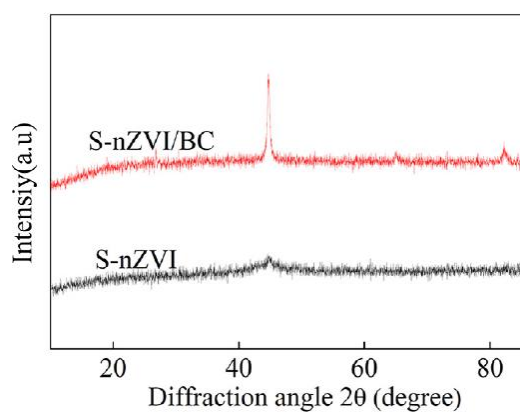


Figure 4.16: XRD patterns of S-nZVI/ biochar composites (Gao, et al., 2018)

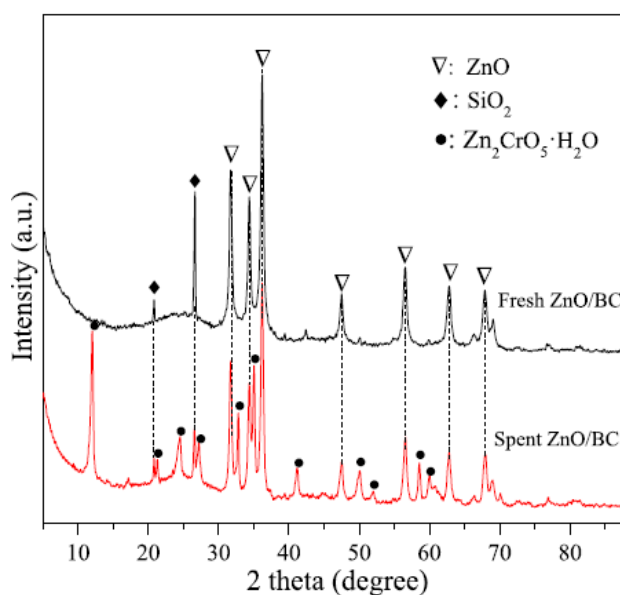


Figure 4.17: XRD patterns of ZnO/ biochar composites (Yu, et al., 2018)

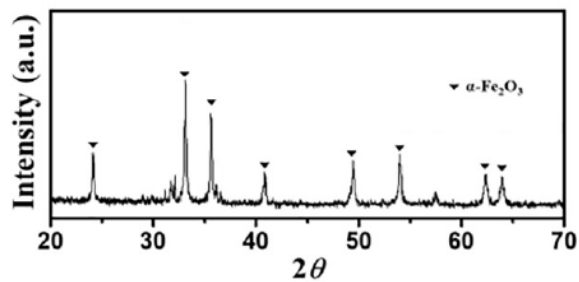


Figure 4.18: XRD patterns of  $\alpha$ -Fe<sub>2</sub>O<sub>3</sub>/ biochar composite (Liu, et al., 2019)

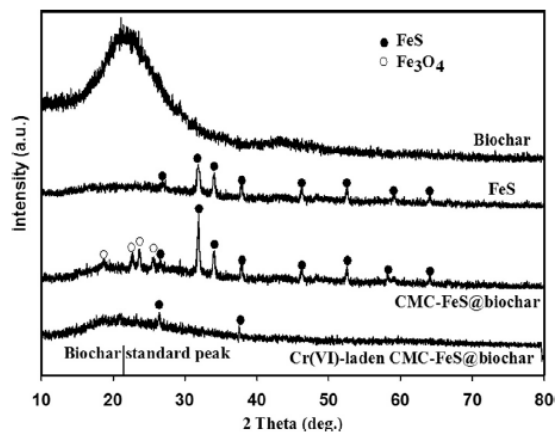


Figure 4.19: XRD patterns of FeS/ biochar composites (Lyu, et al., 2017)

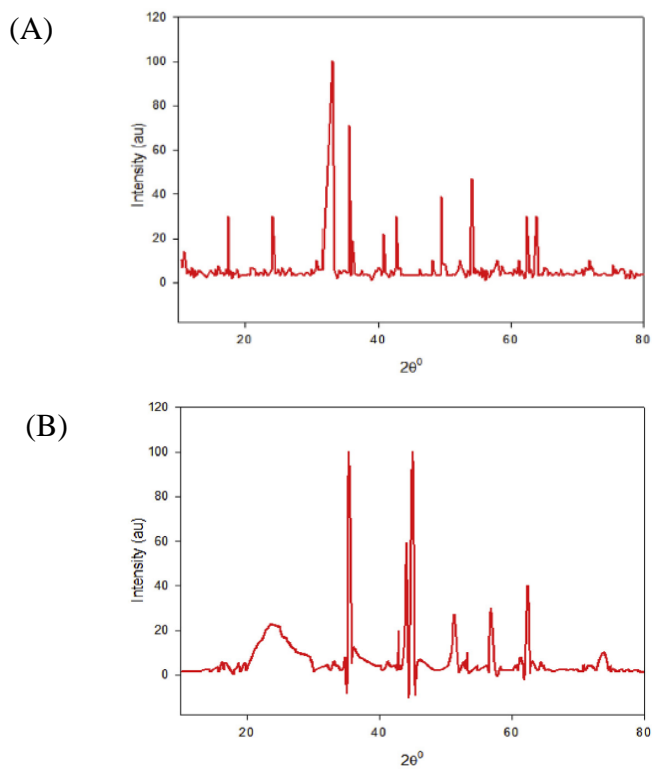


Figure 4.20: XRD patterns of (A) magnetic biochar and (B) PPy/ magnetic biochar (Thines et al., 2017)

## 4.2 Effects on Cr(VI) Removal

The efficiency of various biochar composites on Cr(VI) removal are the main focus under study. It is fundamental to understand the behaviour of the biochar composites in the process of removal by identifying the removal mechanisms and kinetics. Besides, the parameters such as pH, residence time, initial chromium concentration and amount of composites used might have different impacts on Cr(VI) removal by different composites.

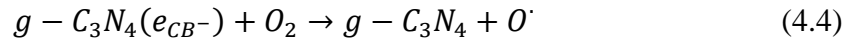
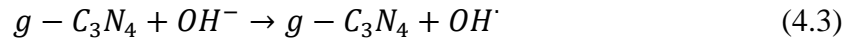
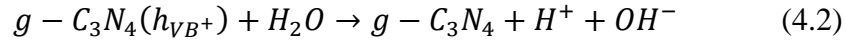
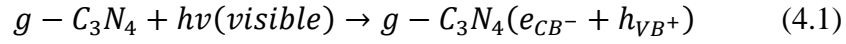
### 4.2.1 Mechanisms and Kinetics Study

The common Cr(VI) removal process by pristine biochar can be divided into two pathways as discussed previously which included adsorption and redox reaction. These involved the processes where Cr(VI) was first adsorbed onto the biochar surfaces, chemically reduced to form Cr(III) species which were then released to the water bodies or exchanged with other positive ions on the biochar surface. The incorporation of other active species onto the biochar surface to form biochar composites might tend to result in additional functional groups aided in the removal of Cr(VI) species.

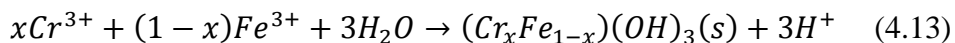
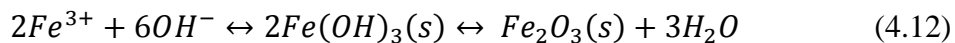
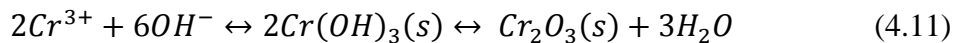
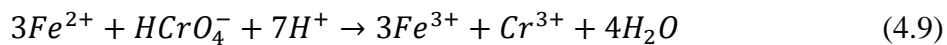
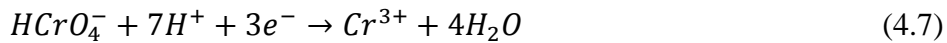
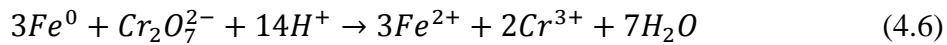
Basically, incorporation of carbonaceous materials such as CNTs and g-C<sub>3</sub>N<sub>4</sub> increased the surface area of biochar for adsorption process to take place. The natures of the carbonaceous materials were similar to biochar where they are organic materials consist mainly of carbon. The edge carbons of CNTs were reported to react with Cr(VI) ions in the form of HCrO<sub>4</sub><sup>-</sup> for the development of more oxygen-containing functional groups on carbon surface such as esters, amides, anhydrides, hydroxyls and esters (Huang, et al., 2019). Moreover, the oxygen-containing functional groups might form surface complexation with Cr(VI) ions and further contributed to the adsorption and redox reactions which enhanced the removal processes.

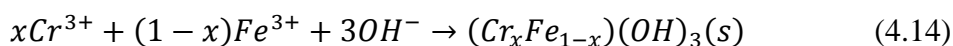
Removal of Cr(VI) by g-C<sub>3</sub>N<sub>4</sub> nanosheets/ biochar composite involved photocatalytic where the photogenerated electrons also involved in the chemical reduction of Cr(VI) species adsorbed on the surface of composite which further enhanced the photocatalytic activities. The conduction band (CB) potential of photocatalyst had to be more negative than the reduction potential of Cr(VI) for Cr(VI) to be reduced by photogenerated electrons (Li, et al., 2019). Photogenerated electrons and radicals were produced by g-C<sub>3</sub>N<sub>4</sub> nanosheets

under excitation of visible light and transferred to biochar via electron conductivity as shown in equations 4.1-4.5 (Jeon, Lee and Baek, 2017). The Cr(VI) was then reduced by photogenerated electrons to Cr(III) and stably fixed to the biochar by electrostatic attraction with the surface functional groups of biochar (Li, et al., 2019).

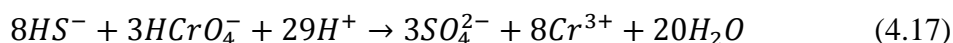
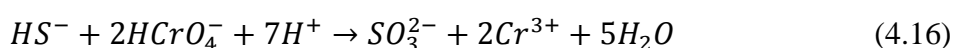


Heterogeneous reduction of attached Cr(VI) species to Cr(III) occurred by direct electron transfer from nZVI and functional groups exist on biochar surface with the involvement of  $H^+$  ions and the electron donors given by equations 4.6 and 4.7. Redox reactions took place where  $Fe^0$  was oxidized into  $Fe^{2+}$  at low pH (equation 4.8) which can be further oxidized into  $Fe^{3+}$  with the reduction of  $HCrO_4^-$  (equation 4.9). Reduction of  $Cr_2O_4^{2-}$  by  $Fe^{2+}$  ions resulted in the precipitation of  $FeCr_2O_4$  as demonstrated by equation 4.10. The release of  $Cr^{3+}$  and  $Fe^{3+}$  ions into the solution allowed the precipitation of  $Cr(OH)_3$ ,  $Cr_2O_3$ ,  $Fe(OH)_3$ ,  $Fe_2O_3$  and  $(Cr_xFe_{1-x})(OH)_3$  with increasing pH as shown in equations 4.11-4.14 (Zhang, et al., 2019). The precipitated products could deposit on the surface of biochar composite and inhibit the passivation of nZVI (Zhang, et al., 2019).

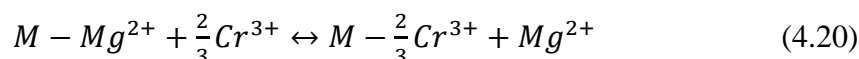




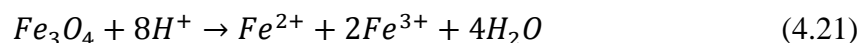
The leaching of Fe ions could be prevented by exchange of Fe ions with Ca ions found in the gel beads of CA while the uptake of Cr(VI) was promoted by complexation with Fe ions trapped inside the matrix (Wan, et al., 2019). Addition of CMC up to the concentration of 0.1% enhanced stabilization by dispersing the nZVI on biochar and maintaining the reactivity of nZVI (Zhang, et al., 2019). The presence of Si particles in biochar served as support and adsorption sites for Fe ions while SiO<sub>2</sub> promoted iron oxidation to enhance Cr(VI) removal (Qian, et al., 2019). Removal mechanisms of Cr(VI) by S-nZVI/biochar composite was similar to the FeS/ biochar composite with the presence of FeS. Chemical reduction of Cr(VI) species was facilitated by electron transfer from partial dissolution of FeS into Fe<sup>2+</sup> and HS<sup>-</sup> ions (equations 4.15-4.17 and 4.9). The resulted Cr(III) ions formed complexes with other species by ion exchange (equation 4.13) and also resulted in precipitation of Cr<sub>2</sub>S<sub>3</sub> and Cr<sub>2</sub>O<sub>3</sub> (Lyu, et al., 2017).



Enhanced removal of Cr(VI) and Cr(III) species was observed in biochar supported MgO and ZnO nanoparticles by adsorption coupled reduction, precipitation and cation exchange mechanisms (Xiao, et al., 2018). The removal of Cr(VI) by the composites was dominated by the interaction of Cr(VI) ions and MgO or ZnO coated on biochar surface. Based on equations 4.18 and 4.19, the MgO tends to dissolve in water to form Mg<sup>2+</sup> and OH<sup>-</sup> ions where OH<sup>-</sup> involved in the precipitation process of Cr<sup>3+</sup> while Mg<sup>2+</sup> was available for cation exchanged with Cr<sup>3+</sup> given by equation 4.20 (Chen, et al., 2015). It was similar to the removal of Cr(VI) by ZnO/ biochar composite in addition to surface complexes. The presence of zinc chromium oxide hydrate (Zn<sub>2</sub>CrO<sub>5</sub>.H<sub>2</sub>O) was identified after adsorption process indicated the precipitation reaction between ZnO and Cr ions involved in the removal mechanisms (Yu, et al., 2018).

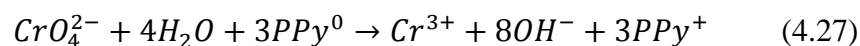
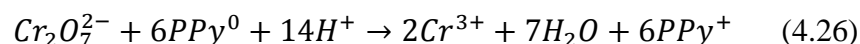
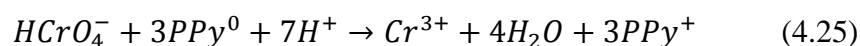


The iron oxides ( $Fe_3O_4$  and  $\alpha$ - $Fe_2O_3$ ) incorporated with biochar contributed to the reduction of Cr(VI) as shown in equations 4.21 and 4.22.  $Fe_3O_4$  was first dissociated into  $Fe^{2+}$  and  $Fe^{3+}$  ions (equation 4.21) and followed by chemical reduction of  $Cr^{6+}$  (equation 4.22) (Wang, et al., 2019). The  $Fe^{3+}$  in iron trioxide ( $\alpha$ - $Fe_2O_3$ ) and hydrous ferric oxide ( $FeOOH$ ) found in  $\alpha$ - $Fe_2O_3$ /biochar composite also provided active chemisorption and reduction sites for Cr(VI). Iron oxyhydroxide groups of  $\alpha$ - $Fe_2O_3$  attracted the remaining Cr(VI) ions and the newly formed Cr(III) for coprecipitation (Liu, et al., 2019). The  $Cr^{3+}$  was easily precipitated on the surface of biochar similar to nZVI/biochar composites.



PPy found in PPy/biochar composite facilitated the adsorption of Cr(VI) species by anions exchange and electrostatic attraction. Negatively charged chromate ions exchanged with the doped  $Cl^-$  ions of PPy on biochar surface (equation 4.23) together with electrostatic attraction of positively charged N atoms ( $N^+$ ) of PPy (Wang, et al., 2019). High electron concentration of PPy enhanced the chemical reduction of Cr(VI) while amine groups ( $-NH-$ ) played an important role as electron donors. The reduction mechanisms of Cr(VI) species in the presence of PPy are demonstrated in equations 4.24-4.27. The Cr(III) ions formed were immobilized on biochar surface by reacting with amine, hydroxyl and carboxyl groups by precipitation and surface complexes while part of them were released by electrostatic repulsion of  $N^+$  and  $Cr^{3+}$  ions (Yang, et al., 2018). Similarly, amine or amino groups were introduced on PEI/ biochar surface for enhanced Cr(VI) adsorption and reduction.





Several kinetic models were applied to analyse the adsorption kinetics of Cr(VI) such as PFO, PSO, intraparticle diffusion and Elovich models. It was known that PFO model was employed to describe physical adsorption and PSO model was applicable to system involved both physical and chemical adsorption while intraparticle diffusion model was performed to analyse the surface adsorption reaction where physical adsorption by pore diffusion was dominant and Elovich model was adopted for multi-mechanism adsorption on heterogeneous surface (Wan, et al., 2019; Zhang, et al., 2019). Based on the kinetics data of Cr(VI) removal by various biochar composites, pseudo-second order models generally achieved higher level of correlation coefficients ( $R^2$ ) with values more than 0.99 indicated that the adsorption process of Cr(VI) involved both physical adsorption and chemisorption by porous structure, surface functional groups and reduction sites (Wan, et al., 2019).

The PSO model with higher value of  $R^2$  compared to PFO model further indicated that chemical adsorption which involved covalent interaction by electrons sharing or transfer between Cr(VI) ions and adsorbent was the rate-limiting step in Cr(VI) adsorption rather than physical diffusion (Zhang, et al., 2019; Xiao, et al., 2018). The process was affected by the availability of active adsorption sites instead of adsorbate concentration (Yang, et al., 2018). For intraparticle diffusion, the plot of data was divided into two stages where the rate of adsorption was high at initial stage and slowed down at the second stage with the increased in boundary layer thickness that decreased the possibility of external mass transfer. Hence, the adsorption process was associated with surface adsorption and intraparticle diffusion processes (Yu, et al., 2018).

For adsorption isotherm, Langmuir, Freundlich and Redlich-Peterson models were commonly performed to fit the data obtained for Cr(VI) adsorption by biochar composites. The Cr(VI) adsorption isotherms showed an increasing adsorption with increasing temperature which represented an endothermic process (Wan, et al., 2019). Langmuir model assumed monolayer adsorption

while Freundlich model was derived by adsorption on heterogeneous surfaces. Redlich-Peterson model combined elements from both Langmuir and Freundlich equations that was applicable to a hybrid process of physical and chemical adsorption (Wan, et al., 2019; Lyu, et al., 2017).

Langmuir isotherm model was well-fitted ( $R^2 > 0.98$ ) to the adsorption data of Cr(VI) as compared to Freundlich isotherm model indicated that monolayer surface coverage was significant to the adsorption of Cr(VI) on biochar composites (Xiao, et al., 2018). It was contributed by homogeneous distribution of active sites with monolayer adsorption (Ma, et al., 2014). However, the Redlich-Peterson model also showed optimum fitting results for nZVI/ biochar composite, suggested that both physical and chemical adsorption took place which coincided with the implication of kinetics data (Wan, et al., 2019).

#### **4.2.2 Parameters Study**

Generally, the effects of several parameters included pyrolysis temperature, pH, residence time, initial chromium concentration and amount of adsorbent applied on removal of Cr(VI) were discussed. The optimum operating conditions for different types of biochar composites used to remove Cr(VI) were also determined based on the studies conducted previously.

Basically, the biochar composites applied to study on Cr(VI) removal were synthesized by pyrolysis at temperature from 400-700 °C. Although increased in temperature improved the properties of composites, further increased in temperature beyond optimum temperature would cease the function of the composites as effective adsorbents. Based on the studies conducted by Qian, et al. (2019) and Yu, et al. (2018), the properties of biochar composites were enhanced by pyrolysis temperature up to 700°C and 750°C respectively where the optimum pyrolysis temperature was around 700°C. Further increased in temperature to 800°C conducted by Yu, et al. (2018) resulted in the collapsed of pore structures which was undesired as an effective adsorbent as shown in Table 2.4.

The optimum pH for effective removal of Cr(VI) was within the range of acidic condition (pH 2-3) where Cr(VI) exists predominantly in the form of  $\text{HCrO}_4^-$  which had greater affinity to be adsorbed with lower adsorption free

energy. Besides that, pH also affected the surface charge of the composites where the surfaces of composites were positively charged at lower pH that favoured the adsorption of negatively charged chromium anion by electrostatic attraction. In addition, the solubility of FeS in FeS/ biochar composite increased significantly at pH below 6 where more  $\text{Fe}^{2+}$  and  $\text{S}^{2-}$  ions were provided for reduction of Cr(VI) (Lyu, et al., 2017). Acidic conditions also promoted the breakdown of passivating oxide layer of iron on nZVI surface that could inhibit the process of removal and increased removal efficiencies (Zhang, et al., 2019; Gao, et al., 2018). Generally, the optimum initial solution pH for removal of Cr(VI) was at about pH 2. However, the optimum pH for Cr(VI) removal by nZVI-CA/ biochar composite was at about pH 4 by taking in consideration of increased leaching of Fe ions with decreased pH of solution (Wan, et al., 2019).

In the case of PPy/ biochar composite, desirable Cr(VI) removal ability was achieved by acidic to neutral and weak alkaline solutions from pH 2-8 where its  $\text{pH}_{\text{pzc}}$  was about 7 which indicated that the surface was positively charged and highly protonated at lower pH. In the meanwhile, further increased of pH from 8-10 only slightly decreased the removal efficiency from 100% to 94%. Therefore, PPy/ biochar composite was able to remove Cr(VI) from solutions in wide pH range (Yang, et al., 2018). Similarly, the removal efficiencies of Cr(VI) by PEI/ biochar composite could be maintained at wider pH ranged from 2 to 7 where the Cr(VI) was efficiently removed in both acidic and neutral conditions. However, the removal efficiencies decreased sharply as pH further increased to alkaline condition (Ma, et al., 2014).

The maximum adsorption capacities of biochar composites under different operating conditions are shown in Table 4.2. It was observed that the maximum adsorption capacities of most biochar composites were obtained in acidic pH of 2-4 included biochar incorporated with carbonaceous materials, nZVI and metal oxides. Despite that, CMC-nZVI/ biochar composites obtained maximum adsorption capacity at pH 5.6 which was in less acidic condition. It was similar to FeS/biochar composite where the optimum pH was found to be pH 5.5. For biochar incorporated with polymer, the pH for maximum adsorption capacity were found to be 5.3 and 6.8 for PPy/ biochar and PEI/ biochar composites respectively where they could be applied in wider pH range.

Table 4.2: Maximum adsorption capacity of biochar composites with different operating conditions

<b>Composites</b>	<b>pH</b>	<b>Initial Cr Concentration (mg/L)</b>	<b>Adsorbent Dosage (g/L)</b>	<b>Residence Time (h)</b>	<b>Maximum Adsorption Capacity (mg/g)</b>	<b>Reference</b>
CNT/ biochar	2	0.5	0.04	0.5	9.0	Atieh (2011)
g-C <sub>3</sub> N <sub>4</sub> / biochar	2	10	1	3	120.0	Li, et al. (2019)
CA-nZVI/ biochar	4	150	1	24	86.4	Wan, et al. (2019)
CMC-nZVI/ biochar	5.6	100	1.25	24	112.5	Zhang, et al. (2019)
Si-nZVI/ biochar	3.5	30	0.2	8	111.9	Qian, et al. (2019)
S-nZVI/ biochar	2.5	50	0.2	4	126.1	Gao, et al. (2018)
FeS/ biochar	5.5	100	0.72	72	130.5	Lyu, et al. (2017)
MgO/ biochar	2	100	1	24	62.3	Xiao, et al. (2018)
ZnO/ biochar	-	100	4	2	24.0	Yu, et al. (2018)
Fe <sub>3</sub> O <sub>4</sub> / biochar	3	200	12	4	47.6	Wang, et al. (2019)
$\alpha$ -Fe <sub>2</sub> O <sub>3</sub> / biochar	-	100	0.21	0.33	167.0	Liu, et al. (2019)
PPy/ biochar	5.3	10	1	-	27.6	Yang, et al. (2018)
PEI/ biochar	6.8	100	1	24	435.7	Ma, et al. (2014)

The residence time, initial chromium concentration and adsorbent dosage are closely related factors. Most of the experiments under reviewed for Cr(VI) removal were carried out with 100 mg/L of initial chromium concentration and 1 g/L of adsorbent dosage. Greater initial chromium concentration required longer residence time and higher amounts of adsorbent dosage for effective removal. In the meanwhile, longer residence time was required when lower amounts of adsorbent applied at constant initial chromium concentration. For example, FeS/ biochar composite took longer time of 72 h to obtain the maximum adsorption capacity of 130.5 mg/g with lower adsorbent dosage of 0.72 g/L as compared to CMC-nZVI/ biochar composites which achieve maximum adsorption capacity of 112.5 mg/L in 24 h with 1.25 g/L of adsorbent used as shown in Table 4.2. Generally, the removal rate of Cr(VI) started with a rapid initial rate and slowed down until equilibrium was reached.

In spite of that, high initial Cr(VI) concentration ( $\geq 50$  mg/L) promoted the formation of Cr-Fe oxide/hydroxide precipitates on the surface of iron-containing biochar composites which would accelerate passivation of Fe<sup>0</sup> or FeS that inhibit the formation of an diffusion layer of solid/water interphases and electron transfer processes (Qian, et al., 2019; Gao, et al., 2018). As a result, major Cr(VI) removal mechanism was limited to Cr(VI) adsorption. Among nZVI/ biochar composites, S-nZVI/ biochar achieved the highest maximum adsorption capacity of 126.1 mg/g with initial Cr(VI) concentration of 50 mg/L and adsorbent dosage of 0.2 g/L as shown in Table 4.2. Besides,  $\alpha$ -Fe<sub>2</sub>O<sub>3</sub>/ biochar obtained maximum adsorption capacity of 167 mg/g at natural pH.

Based on Table 4.2, g-C<sub>3</sub>N<sub>4</sub>/ biochar achieved higher maximum adsorption capacity of 120 mg/g with initial Cr(VI) concentration of 10 mg/L and adsorbent dosage of 1g/L at pH 2 compared to CNTs/ biochar composite with adsorption capacity of 9 mg/g. In the meanwhile, the maximum adsorption capacity of MgO/ biochar composite was 62.3 mg/g with lower adsorbent dosage and higher residence time than the study of ZnO/ biochar composite with adsorption capacity of 24 mg/g. The highest maximum adsorption capacity was obtained by PEI/ biochar composite with 435.7 mg/g at relatively high pH of 6.8 with initial Cr(VI) concentration of 100 mg/L and adsorbent dosage of 1 g/L.

According to Figure 4.21 (A), the removal of Cr(VI) decreased significantly from 117.4 mg/g to 16.2 mg/g with initial pH increased from 3 to

9. For constant reaction pH as shown in Figure 4.21 (B), Cr(VI) removal remained at 132.8 mg/g from pH 2-4 and decreased to 21.8 mg/g from pH 4-9. It was noted that higher uptakes of Cr(VI) were resulted by maintaining constant pH throughout the reaction. In consideration of reaction time as shown in Figure 4.22, it was observed that the concentration of total Cr and Cr(VI) decreased while Cr(III) increased in the first 45 minutes due to chemical reduction of Cr(VI). It was then proceeded with decreasing total Cr, Cr(VI) and Cr(III) with reaction time where the reduced Cr(III) was exchanged with ions or complexed with functional groups found in biochar composites.

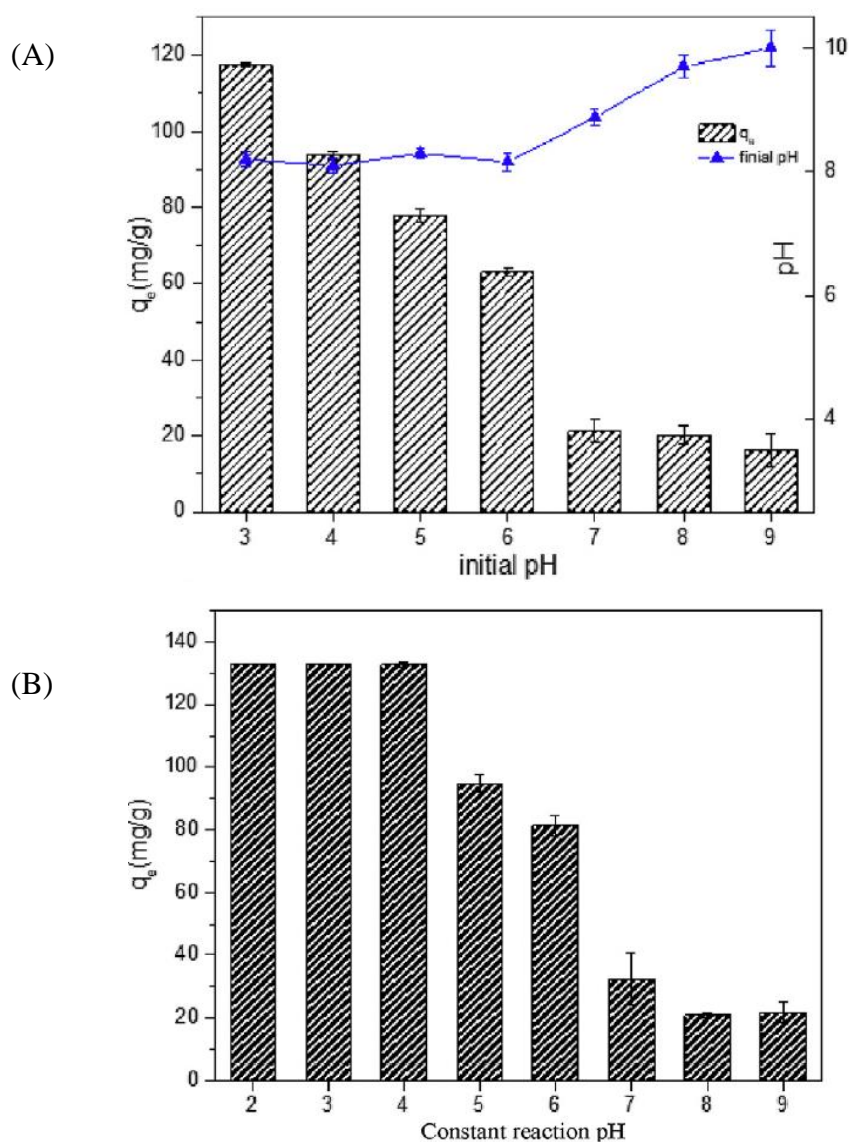


Figure 4.21: The effect of (A) initial pH and (B) constant reaction pH on removal of Cr(VI) by CMC-nZVI/biochar (Zhang, et al., 2019)

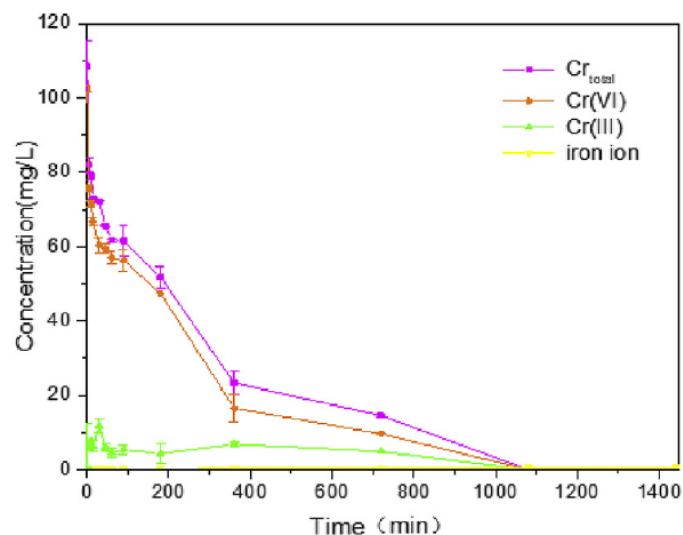


Figure 4.22: Concentration of Cr species and dissolved ion during reaction by CMC-nZVI/ biochar (Zhang, et al., 2019)

The uptake of Cr(VI) was rapid at the first 100 minutes and gradually decreased with reaction time attributed to the decreased of adsorption sites and adsorbate as time proceeding. Therefore, the impacts of time on removal of Cr(VI) was only significant at the initial state of reaction. It was similar to the initial chromium concentration and adsorbent dosage where the significance of their impacts on removal of Cr(VI) were limited to the early stage of reaction. However, greater initial chromium concentration and adsorbent dosage allowed rapid Cr(VI) removal to be last for longer time where sufficient adsorption sites and adsorbates were available in longer residence time. The increased in initial chromium concentration must be followed by increasing adsorbent dosage as the adsorption of adsorbate was subjected to the availability to adsorption sites.

Therefore, pH of the solution showed greater significant impacts on the efficiency of Cr(VI) removal among the parameters under discussion. This is because the removal of Cr(VI) was mainly depending on the surface charges of composites and the affinity of Cr<sup>6+</sup> compounds present at respective pH to be adsorbed. The removal mechanisms included chemical adsorption, chemical reduction and ions exchange were dependent on the electrical charges of biochar composites and Cr<sup>6+</sup> compounds which were affected by pH while physical adsorption was depending on the adsorption sites and adsorbate which were mostly affected by residence time, initial chromium concentration and the adsorbent dosage.

### 4.3 Regeneration Study

The reusability of adsorbent is one of the important factors to be considered for the actual application of biochar composites in Cr(VI) removal. Recyclable adsorbent that can be easily regenerated while maintaining reasonable adsorption efficiency is preferable as a cost-effective adsorbent. Application of acid or alkaline solution such as HCl or NaOH was often used to examine the regeneration capacity of biochar composite on Cr(VI). Biochar treated with HCl showed higher regeneration ability compared to NaOH at equal concentration (Shakya and Agarwal, 2019). Generally, the adsorption capacity decreased gradually after each cycle of adsorption-desorption process and the degree of reduction determined its reusability.

Selvaraj, et al. (2020) stated that oxidized CNT material could be easily regenerated by NaOH solution to be reused effectively. However, desorption of Cr(VI) from pristine g-C<sub>3</sub>N<sub>4</sub> was difficult to occur where it was hardly regenerated due to its strong complexation with Cr(VI) anions (Xiao, et al., 2019). The reusability of nZVI/ biochar composite was tested by Fan, et al. (2019) with three adsorption-desorption cycle where it showed that the Cr(VI) removal capacity was significantly damaged from 25.04 to 8.04 and 7.46 mg/g where it lost its reductive nature after each regeneration. Despite that, post-adsorption nZVI/ biochar composite showed stable magnetic properties with precipitation of Fe<sub>3</sub>O<sub>4</sub> present with both Fe<sup>2+</sup> and Fe<sup>3+</sup> ions for easy separation (Fan, et al., 2019). Thus, magnetic biochar like Fe<sub>3</sub>O<sub>4</sub>/ biochar composite showed a good reusability due to its easy separation property in regeneration studies for dye removal by Ma, et al. (2015).

MgO/ biochar composite possessed high reusability where it maintained a high Cr(VI) removal efficiency of >57% after 4 cycles of regeneration (Xiao, et al., 2018). According to Yu, et al. (2018), ZnO/ biochar composite was regenerated by repeated adsorption and dilute ammonia water desorption processes where 67.1% of the initial removal capacity was remained in the fifth runs. The regeneration of Fe<sub>3</sub>O<sub>4</sub>/ biochar composite by NaOH was studied by Wang, et al. (2019) and a removal ratio of 78.56% at the seventh cycle was noted. The capacity of Fe<sub>3</sub>O<sub>4</sub>/ biochar composite to be reused was also determined by its magnetic properties where the saturated magnet intensity only

decreased slightly by 20.83% after seven generations and magnetic separation was applicable. However, the removal efficiency of pure  $\text{Fe}_3\text{O}_4$  decreased dramatically after 7 cycles of regeneration from about 96% to 66% as shown in Figure 4.23. The results indicated that organic coating was required to improve the stability of nano-iron in treating wastewater (Wang, et al., 2019). In addition, PEI/ biochar composite maintained a stable performance on removal of Cr(VI) after six cycles of adsorption-desorption processes by NaOH with high adsorption capability (Ma, et al., 2014). These implied that the biochar composites possessed good recyclability as a low cost adsorbent to remove Cr(VI).

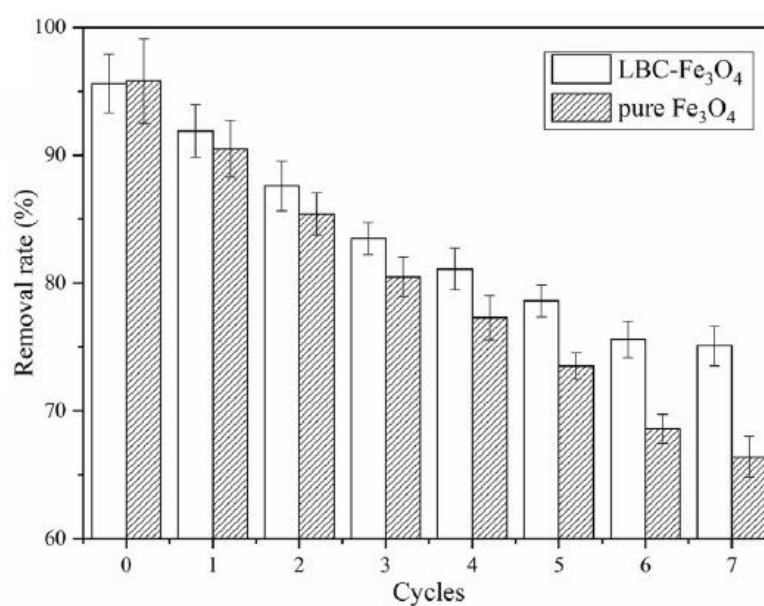


Figure 4.23: Regeneration tests carried out on  $\text{Fe}_3\text{O}_4$ / biochar composite and pure  $\text{Fe}_3\text{O}_4$  (Wang, et al., 2019)

The regeneration study for biochar composites were conducted with various number of cycles to determine their reusability as shown in Table 4.3. A minimum of three adsorption-desorption cycles should be carried out to obtain better understanding on the adsorption efficiency of biochar composites after regeneration. The results of first cycle showed the effects of regeneration on the removal capacity of recycled biochar composites where it was generally declined due to the consumption of active components. Furthermore, second and subsequent cycles of regeneration was conducted to observe the degree of

reduction in removal capacity of biochar composites after each cycle. It allowed the determination of the trend in reduction of removal capacity and evaluation of the regeneration capacity of the composites. Higher retention of removal efficiency possessed greater stability and reusability of the biochar composites which presented as a potential low-cost and high efficiency adsorbent for Cr(VI) removal. Therefore, regeneration study was important to be conducted on biochar composites as one of the important considerations for effective removal of Cr(VI).

Table 4.3: Regeneration study carried out on biochar composites

<b>Composites</b>	<b>Eluent</b>	<b>Number of Cycles</b>	<b>Reference</b>
nZVI/ biochar	-	3	Fan, et al. (2019)
MgO/ biochar	-	4	Xiao, et al. (2018)
ZnO/ biochar	Dilute NH <sub>3</sub>	5	Yu, et al. (2018)
Fe <sub>3</sub> O <sub>4</sub> / biochar	0.01M NaOH	7	Wang, et al. (2019)
PEI/ biochar	1M NaOH	6	Ma, et al. (2014)

## CHAPTER 5

### CONCLUSIONS AND RECOMMENDATIONS

#### 5.1 Conclusions

For characterization results, SEM images showed that nanoparticles were dispersed on biochar surface to form rough and porous surface while entrapment of foreign particles within porous structure decreased the surface area of pristine biochar where biochar served to segregate nanoparticles. ZnO/ biochar and PPy/ biochar had considerably high specific surface area. The presence of respective adsorption bands or diffraction peaks in FTIR spectra and XRD patterns proved that all of the active components were successfully attached on biochar.

Special findings in this research were the photocatalytic action of g-C<sub>3</sub>N<sub>4</sub>/ biochar and the presence of amine group in PPy/ biochar and PEI/ biochar for enhanced Cr(VI) reduction while metal cations like Fe<sup>2+</sup>, Fe<sup>3+</sup>, Mg<sup>2+</sup> and Zn<sup>2+</sup> promoted the precipitation of Cr<sup>3+</sup> ions. Generally, pH of solution showed greater influence on Cr(VI) adsorption where it was optimally removed in acidic condition at pH 2-4 while PPy/ biochar and PEI/ biochar composites showed excellent adsorption capacity at wide range of pH up to 8 and 7 respectively.

Based on the results of analysis, the highest maximum adsorption capacity of 435.7 mg/g was achieved by PEI/ biochar composite at pH 6.8. g-C<sub>3</sub>N<sub>4</sub>/ biochar, S-nZVI/ biochar,  $\alpha$ -Fe<sub>2</sub>O<sub>3</sub>/ biochar and PEI/ biochar composites were suggested out of each category for effective Cr(VI) removal based on their maximum adsorption capacity achieved at optimum operating conditions. In regeneration study, biochar composites possessed good recyclability apart from g-C<sub>3</sub>N<sub>4</sub>/ biochar that formed strong complexation with Cr(VI) anions where desorption process was difficult to take place.

As a conclusion, the objectives were achieved where it was identified that biochar composites were synthesized by either pre- or post-pyrolysis of biochar treated with foreign active compounds. Adsorption, chemical precipitation and ions exchange aided in Cr(VI) removal which was affected by pH of solution, residence time, initial Cr concentration and adsorbent dosage. In summary, PEI/ biochar composite was outstanding from other biochar

composites under study due to its excellent adsorption capacity at wide range of pH up to pH 7 and good reusability. However, the preparation methods and operating conditions that would affect the results were varied in experiments conducted by the sources of journals. Therefore, future research is required to ensure the accuracy of results and comparison.

## **5.2 Recommendations for Future Work**

Since the research analysis was conducted based on the data obtained from various journals review, the comparison of results was affected by different operating conditions. In addition, limited published data was available to provide adequate evidences for the effectiveness of biochar composites for the removal of Cr(VI). Therefore, improvements can be taken in future research study to improve the accuracy and reliability of the results. Several recommendations for future related study are listed as followed.

- i. Preparation of pristine biochar should be the same for all of the composites with same raw materials and pyrolysis temperature for effective comparison on the results of modification.
- ii. The characterization techniques and removal processes of biochar composites should be carried out under same operating conditions to show the accuracy in results comparison.
- iii. Any equipment used should be consistent to reduce the diversity of results.
- iv. The ratio of modifying agents added to pristine biochar should be determined to ensure effective removal of Cr(VI).
- v. Experiments can be carried out on water contaminated with various substances to determine the practicability of biochar composites in wastewater treatment which usually do not contain only Cr(VI).
- vi. Further study on reusability of biochar composites are required with a minimum of three cycles of adsorption-desorption process.
- vii. Pilot-scale testing can be done to determine the stability of biochar composites to cope with the continuous fluctuations in pH and temperature of natural environment.

## REFERENCES

- Agency for Toxic Substances and Disease Registry, 2008. *Chromium toxicity*. [online] Available at: < <https://www.atsdr.cdc.gov/csem/chromium/docs/chromium.pdf> > [Accessed 11 June 2019]
- Aguiar, E. C., Gasco, G., Ferreiro, J. P. and Mendez, A., 2019. Thermogravimetric analysis and carbon stability of chars produced from slow pyrolysis and hydrothermal carbonization of manure waste. *Journal of Analytical and Applied Pyrolysis*, 140, pp. 434-443.
- Akpor, O. B., Ohiobor, G. O. and Olaolu, T. D., 2014. Heavy metal pollutants in wastewater effluents: Sources, effects and remediation. *Advances in Bioscience and Bioengineering*, 2(4), pp. 37-43.
- Almeida, J. C., Cardoso, C. E. D., Tavares, D. S., Freitas, R., Trindade, T., Vale, C. and Pereira, E., 2019. Chromium removal from contaminated waters using nanomaterials – A review. *Trends in Analytical Chemistry*, 118, pp. 277-291.
- Amalraj, A., Selvi, M. K., Rajeswari, A. and Pius, A., 2016. Preparation and characterization of aspartic acid doped polypyrrole for the efficient removal of Cr(VI) from aqueous solution. *Journal of Water Process Engineering*, 11, pp. 162-173.
- Atieh, M. A., 2011. Removal of chromium (VI) from polluted water using carbon nanotubes supported with activated carbon. *Procedia Environmental Sciences*, 4, pp. 281-293.
- Azargohar, R., Nanda, S., Dalai, A. K. and Kozinski, J. A., 2019. Physico-chemistry of biochars produced through steam gasification and hydro-thermal gasification of canola hull and canola meal pellets. *Biomass and Bioenergy*, 120, pp. 458-470.
- Bhateria, R. and Singh, R., 2019. A review on nanotechnological application of magnetic iron oxides for heavy metal removal. *Journal of Water Process Engineering*, 31, pp. 100845.
- Bis, Z., Kobylecki, R., Scislowska, M. and Zarzycki, R., 2018. Biochar – Potential tool to combat climate change and drought. *Ecohydrology and Hydrobiology*, 18(4), pp. 441-453.
- Castillo, I. F., Matteis, L. D., Marquina, C., Guillen, E. G., Fuente, J. M. D. L. and Mitchell, S. G., 2019. Protection of 18th century paper using antimicrobial nano-magnesium oxide. *International Biodeterioration & Biodegradation*, 141, pp. 79-86.

Chan, Y. H., Cheah, K. W., How, B. S., Loy, A. C. M., Shahbaz, M., Singh, H. K. G., Yusuf, N. R., Shuhaili, A. F. A., Yusup, S., Ghani, W. A. W. A. K., Rambli, J., Kansha, Y., Lam, H. L., Hong, B. H. and Ngan, S. L., 2019. An overview of biomass thermochemical conversion technologies in Malaysia. *Science of the Total Environment*, 680, pp. 105-123.

Chen, T., Zhou, Z., Xu, S., Wang, H. and Lu, W., 2015. Adsorption behavior comparison of trivalent and hexavalent chromium on biochar derived from municipal sludge. *Bioresource Technology*, 190, pp. 388-394.

Chen, Y., Liang, W., Li, Y., Wu, Y., Chen, Y., Xiao, W., Zhao, L., Zhang, J. and Li, H., 2019. Modification, application and reaction mechanisms of nano-sized iron sulfide particles for pollutant removal from soil and water: A review. *Chemical Engineering Journal*, 362, pp. 144-159.

Chen, Y., Wang, B., Xin, J., Sun, P. and Wu, D., 2018. Adsorption behavior and mechanism of Cr(VI) by modified biochar derived from *Enteromorpha prolifera*. *Ecotoxicology and Environmental Safety*, 164, pp. 440-447.

Chia, C. H., Gong, B., Joseph, S. D., Marjo, C. E., Munroe, P. and Rich, A. M., 2012. Imaging of mineral-enriched biochar by FTIR, Raman and SEM-EDX. *Vibrational Spectroscopy*, 62, pp. 248-257.

Chirita, P. and Schlegel, M. L., 2015. Oxidative dissolution of iron monosulfide (FeS) in acidic conditions: The effect of solid pretreatment. *International Journal of Mineral Processing*, 135, pp. 57-64.

Choppala, G., Bush, R., Moon, E., Ward, N., Wang, Z., Bolan, N. and Sullivan, L., 2017. Oxidative transformation of iron monosulfides and pyrite in estuarine sediments: Implications for trace metals mobilisation. *Journal of Environmental Management*, 186, pp. 158-166.

Choudhary, B. and Paul, D., 2018. Isotherms, kinetics and thermodynamics of hexavalent chromium removal using biochar. *Journal of Environmental Chemical Engineering*, 6(2), pp. 2335-2343.

Chouvy, C. D., Fakhry, A. and Pillier, F., 2018. Electrosynthesis of polypyrrole nano/micro structures using an electrogenerated oriented polypyrrole nanowire array as framework. *Electrochimica Acta*, 268, pp. 66-72.

Dai, Y., Zhang, N., Xing, C., Cui, Q. and Sun, Q., 2019. The adsorption, regeneration and engineering applications of biochar for removal organic pollutants: A review. *Chemosphere*, 223, pp. 12-27.

Du, J., Bao, J., Lu, C. and Werner, D., 2016. Reductive sequestration of chromate by hierarchical FeS@Fe<sub>0</sub> particles. *Water Research*, 102, pp. 73-81.

E-Medical Prep, 2019. *Adsorption*. [online] Available at: <<https://www.emedicalprep.com/study-material/chemistry/surface-chemistry/adsorption/>> [Accessed 20 June 2019]

Elkhalifa, E. A. and Friedrich, H. B., 2014. Magnesium oxide as a catalyst for the dehydrogenation of n-octane. *Arabian Journal of Chemistry*, 11, pp. 1154-1159.

Elkhalifa, S., Ansari, T. A., Mackey, H. R. and McKay, G., 2019. Food waste to biochars through pyrolysis: A review. *Resources, Conservation and Recycling*, 144, pp. 310–320.

Ebrahim, A. A. A. and Mansour, F. R., 2019. Targeted magnetic iron oxide nanoparticles: Preparation, functionalization and biomedical application. *Journal of Drug Delivery Science and Technology*, 52, pp. 702-712.

Environmental Protection Agency, 2016. *Chromium compounds*. [online] Available at: <<https://www.epa.gov/sites/production/files/2016-09/documents/chromium-compounds.pdf>> [Accessed 8 June 2019]

Fan, Z., Zhang, Q., Gao, B., Li, M., Liu, C. and Qiu, Y., 2019. Removal of hexavalent chromium by biochar supported nZVI composite: Batch and fixed-bed column evaluations, mechanisms, and secondary contamination prevention. *Chemosphere*, 217, pp. 85-94.

Fang, W., Jiang, X., Luo, H. and Geng, J., 2018. Synthesis of graphene/SiO<sub>2</sub>@polypyrrole nanocomposites and their application for Cr(VI) removal in aqueous solution. *Chemosphere*, 197, pp. 594-602.

Feng, Y., Yang, L., Liu, J. and Logan, B. E., 2016. Electrochemical technologies for wastewater treatment and resource reclamation. *Environmental Science: Water Research & Technology*, 2(5), pp. 800-831.

Gao, J., Yang, L., Liu, Y., Shao, F., Liao, Q. and Shang, J., 2018. Scavenging of Cr(VI) from aqueous solutions by sulfide-modified nanoscale zero-valent iron supported by biochar. *Journal of the Taiwan Institute of Chemical Engineers*, 91, pp. 449-456.

Gholami, P., Dinpazhoh, L., Khataee, A. and Orooji, Y., 2019. Sonocatalytic activity of biochar-supported ZnO nanorods in degradation of gemifloxacin: Synergy study, effect of parameters and phytotoxicity evaluation. *Ultrasonics – Sonochemistry*, 55, pp. 44-56.

Glaser, B., Haumaier, L., Guggenberger, G. and Zech, W., 2001. The ‘Terra Petra’ phenomenon: A model for sustainable agriculture in the humid tropics. *Naturwissenschaften*, 88, pp. 37-41.

Godiya, C. B., Cheng, X., Deng, G., Li, D. and Lu, X., 2019. Silk fibroin/polyethylenimine functional hydrogel for metal ion adsorption and upcycling utilization. *Journal of Environmental Chemical Engineering*, 7, pp. 102806.

Grand View Research, 2019. *Biochar Market Size, Share & Trends Analysis Report By Technology (Gasification, Pyrolysis), By Application (Agriculture (Farming, Livestock)), By Region, And Segment Forecasts, 2019 – 2025*. [online] Available at: < <https://www.grandviewresearch.com/industry-analysis/biochar-market> > [Accessed 24 June 2019]

Haeldermans, T., Claesen, J., Maggen, J., Carleer, R., Yperman, J., Adriaensens, P., Samyn, P., Vandamme, D., Cuypers, A., Vanreppelen, K. and Schreurs, S., 2019. Microwave assisted and conventional pyrolysis of MDF – Characterization of the produced biochars. *Journal of Analytical and Applied Pyrolysis*, 138, pp. 218-230.

Hagemann, N., Spokas, K., Schmidt, H. P., Kagi, R., Bohler, M. A. and Bucheli, T. D., 2018. Activated carbon, biochar and charcoal: Linkages and synergies across pyrogenic carbon's ABCs. *Water* 2018, 10, pp. 182.

Hu, Y., Zhu, Y., Zhang, Y., Lin, T., Zeng, G., Zhang, S., Wang, Y., He, W., Zhang, M. and Long, H., 2019. An efficient adsorbent: Simultaneous activated and magnetic ZnO doped biochar derived from camphor leaves for ciprofloxacin adsorption. *Bioresource Technology*, 288, pp. 121511.

Huang, J., Cao, Y., Qin, B., Zhong, G., Zhang, J., Yu, H., Wang, H. and Peng, F., 2019. Highly efficient and acid-corrosion resistant nitrogen doped magnetic carbon nanotubes for the hexavalent chromium removal with subsequent reutilization. *Chemical Engineering Journal*, 361, pp. 547-558.

Inagaki, M., Tsumura, T., Kinumoto, T. and Toyoda, M., 2019. Graphitic carbon nitrides (g-C<sub>3</sub>N<sub>4</sub>) with comparative discussion to carbon materials. *Carbon*, 141, pp. 580-607.

Inyang, M., Gao, B., Zimmerman, A., Zhang, M. and Chen, H., 2014. Synthesis, characterization, and dye sorption ability of carbon nanotube–biochar nanocomposites. *Chemical Engineering Journal*, 236, pp. 39-46.

Ippolito, J. A., Spokas, K. A., Novak, J. M., Lentz, R. D. and Cantrell K. B., 2015. Biochar elemental composition and factors influencing nutrient retention. *Biochar for Environmental Management: Science, Technology and Implementation*, 7, pp.137-161.

Ismail, A., Toriman, M. E., Juahir, H., Zain, S. M., Habir, N. L. A., Retnam, A., Kamaruddin, M. K. A., Umar, R. and Azid, A., 2016. Spatial assessment and source identification of heavy metals pollution in surface water using several chemometric techniques. *Marine Pollution Bulletin*, 106(1–2), pp. 292–300.

Jeon, P., Lee, M. E. and Baek, K., 2017. Adsorption and photocatalytic activity of biochar with graphitic carbon nitride (g-C<sub>3</sub>N<sub>4</sub>). *Journal of the Taiwan Institute of Chemical Engineers*, 77, pp. 244-249.

Jian, X., Zhuang, X., Li, B., Xu, X., Wei, Z., Song, Y. and Jiang, E., 2018. Pyrolysis vs. hydrothermal carbonization: Understanding the effect of biomass structural components and inorganic compounds on the char properties. *Environmental Technology & Innovation*, 10, pp. 27-35.

Jung, S., Park, Y. and Kwon, E. E., 2019. Strategic use of biochar for CO<sub>2</sub> capture and sequestration. *Journal of CO<sub>2</sub> Utilization*, 32, pp. 128–139.

Kumar, T. H. V., Sivasankar, V., Fayoud, N., Oualid, H. A. and Sundramoorthy, A. K., 2018. Synthesis and characterization of coral-like hierarchical MgO incorporated fly ash composite for the effective adsorption of azo dye from aqueous solution. *Applied Surface Science*, 449, pp. 719-728.

Lawrinenko, M., 2014. *Anion exchange capacity of biochar*. Master. Iowa State University.

Lee, H. W., Lee, H., Kim, Y. M., Park, R. S. and Park, Y. K., 2019. Recent application of biochar on the catalytic biorefinery and environmental processes. *Chinese Chemical Letters*, 1(1), pp. 2–5.

Li, H., Dong, X., Silva, E. B. D., Oliveira, L. M. D., Chen, Y. and Ma, L. Q., 2017. Mechanisms of metal sorption by biochars: Biochar characteristics and modifications. *Chemosphere*, 178, pp. 466-478.

Li, H., Li, M., Qiu, G., Li, C., Qu, C. and Yang, B., 2015. Synthesis and characterization of MgO nanocrystals for biosensing applications. *Journal of Alloys and Compounds*, 632, pp. 639-644.

Li, J., Dai, J., Liu, G., Zhang, H., Gao, Z., Fu, J., He, Y. and Huang, Y., 2016. Biochar from microwave pyrolysis of biomass: A review. *Biomass and Bioenergy*, 94, pp. 228-244.

Li, K., Huang, Z., Zhu, S., Luo, S., Yan, L., Dai, Y., Guo, Y. and Yang, Y., 2019. Removal of Cr(VI) from water by a biochar-coupled g-C<sub>3</sub>N<sub>4</sub> nanosheets composite and performance of a recycled photocatalyst in single and combined pollution systems. *Applied Catalysis B: Environmental*, 243, pp. 386-396.

Li, X., Qian, X., An, X. and Huang, J., 2019. Preparation of a novel composite comprising biochar skeleton and “chrysanthemum” g-C<sub>3</sub>N<sub>4</sub> for enhanced visible light photocatalytic degradation of formaldehyde. *Applied Surface Science*, 487, pp. 1262-1270.

Liu, Y. L., Li, Y. T., Huang, J. F., Zhang, Y. L., Ruan, Z. H., Hu, T., Wang, J. J., Li, W. Y., Hu, H. J. and Jiang, G. B., 2019. An advanced sol–gel strategy for enhancing interfacial reactivity of iron oxide nanoparticles on rosin biochar substrate to remove Cr(VI). *Science of the Total Environment*, 690, pp. 438-446.

- Lyu, H., Tang, J., Huang, Y., Gai, L., Zeng, E. Y., Liber, K. and Gong, Y., 2017. Removal of hexavalent chromium from aqueous solutions by a novel biochar supported nanoscale iron sulfide composite. *Chemical Engineering Journal*, 322, pp. 516-524.
- Ma, H., Li, J. B., Liu, W. W., Miao, M., Cheng, B. J. and Zhu, S. W., 2015. Novel synthesis of a versatile magnetic adsorbent derived from corncob for dye removal. *Bioresource Technology*, 190, pp. 13-20.
- Ma, Y., Liu, W. J., Zhang, N., Li, Y. S., Jiang, H. and Sheng, G. P., 2014. Polyethylenimine modified biochar adsorbent for hexavalent chromium removal from the aqueous solution. *Bioresource Technology*, 169, pp. 403-408.
- Magesa, F., Wu, Y., Tian, Y., Vianney, J. M., Buza, J., He, Q. and Tan, Y., 2019. Graphene and graphene like 2D graphitic carbon nitride: Electrochemical detection of food colorants and toxic substances in environment. *Trends in Environmental Analytical Chemistry*, 23, pp. e00064.
- Mamba, G. and Mishra, A. K., 2016. Graphitic carbon nitride (g-C<sub>3</sub>N<sub>4</sub>) nanocomposites: A new and exciting generation of visible light driven photocatalysts for environmental pollution remediation. *Applied Catalysis B: Environmental*, 198, pp. 347-377.
- Mary, G. S., Sugumaran, P., Niveditha, S., Ramalakshmi, B., Ravichandran, P. and Seshadri, S., 2016. Production, characterization and evaluation of biochar from pod (*Pisum sativum*), leaf (*Brassica oleracea*) and peel (*Citrus sinensis*) wastes. *International Journal of Recycling of Organic Waste in Agriculture*, 5(1), pp. 43-53.
- McGuire, M. J., Blute, N. K., Qin, G., Kavounas, P., Froelich, D. and Fong, L., 2007. *Hexavalent chromium removal using ion exchange and reduction with coagulation and filtration*. [online] Available at: <<https://www.glendaleca.gov/home/showdocument?id=14798>> [Accessed 23 June 2019]
- Minisy, I. M., Bober, P., Acharya, U., Trchova, M., Hromadkova, J., Pflieger, J. and Stejskal, J., 2019. Cationic dyes as morphology-guiding agents for one-dimensional polypyrrole with improved conductivity. *Polymer*, 174, pp. 11-17.
- Mylavarapu, Nair and Morgan, 2016. *An Introduction to Biochars and Their Uses in Agriculture*. [online] Available at: <<https://edis.ifas.ufl.edu/pdf/files/SS/SS58500.pdf>> [Accessed 24 June 2019]
- Owlad, M., Aroua, M. K., Daud, W. A. W. and Baroutian, S., 2008. Removal of hexavalent chromium-contaminated water and wastewater: A review. *Water, Air, and Soil Pollution*, 200(1), pp. 59-77.
- Pi, L., Jiang R., Zhou, W., Zhu, H., Xiao, W., Wang, D. and Mao, X., 2015. g-C<sub>3</sub>N<sub>4</sub> modified biochar as an adsorptive and photocatalytic material for decontamination of aqueous organic pollutants. *Applied Surface Science*, 358, pp. 231-239.

- Pires, B. C., Nascimento, T. A. D., Dutra, F. V. A. and Borges, K. B., 2019. Removal of a non-steroidal anti-inflammatory by adsorption on polypyrrole/multiwalled carbon nanotube composite—Study of kinetics and equilibrium in aqueous medium. *Colloids and Surfaces A*, 578, pp. 123583.
- Premarathna, K. S. D., Rajapaksha, A. U., Sarkar, B., Kwon, E. E., Bhatnagar, A., Ok, Y. S. and Vithanage, M., 2019. Biochar-based engineered composites for sorptive decontamination of water: A review. *Chemical Engineering Journal*, 372, pp. 536-550.
- Prokes, J., Varga, M., Vrnata, M., Valtera, S., Stejskal, J. and Kopecky, D., 2019. Nanotubular polypyrrole: Reversibility of protonation/deprotonation cycles and long-term stability. *European Polymer Journal*, 115, pp. 290-297.
- Qi, Y., Zhu, L., Shen, X., Sotto, A., Gao, C. and Shen, J., 2019. Polyethyleneimine-modified original positive charged nanofiltration membrane: Removal of heavy metal ions and dyes. *Separation and Purification Technology*, 222, pp. 117-124.
- Qian, L., Shang, X., Zhang, B., Zhang, W., Su, A., Chen, Y., Ouyang, D., Han, L., Yan, J. and Chen, M., 2019. Enhanced removal of Cr(VI) by silicon rich biochar-supported nanoscale zero-valent iron. *Chemosphere*, 215, pp. 739-745.
- Rajapaksha, A. U., Chen, S. S., Tsang, D. C. W., Zhang, M., Vithanage, M., Mandal, S., Gao, B., Bolan, N. S. and Ok, Y. S., 2016. Engineered/designer biochar for contaminant removal/immobilization from soil and water: Potential and implication of biochar modification. *Chemosphere*, 148, pp. 276-291.
- Rangabhashiyam, S. and Balasubramanian, P., 2019. Industrial Crops & Products. The potential of lignocellulosic biomass precursors for biochar production : Performance , mechanism and wastewater application — A review. *Industrial Crops & Products*, 128, pp. 405–423.
- Reyes, J. V., Reyes, R. B. G., Gonzalez, A. G., Regalado, E. S. and Cordova, F. C., 2019. Adsorption mechanisms of hexavalent chromium from aqueous solutions on modified activated carbons. *Journal of Environmental Management*, 236, pp. 815-822.
- Richards, T., 2016. Biochar production opportunities for South East Asia: An overview of the many different ways in which biochar can be created. *UTAR Agricultural Science Journal*, 2(1), pp. 12-20.
- Ruba, A. A., Johny, L. M., Jothi, N. S. N. and Sagayaraj, P., 2019. Solvothermal synthesis, characterization and photocatalytic activity of ZnO nanoparticle. *Materials Today: Proceedings*, 8, pp. 94-98.
- Sarkar, B., Mandal, S., Tsang, Y. F., Kumar, P., Kim, K. H. and Ok, Y. S., 2018. Designer carbon nanotubes for contaminant removal in water and wastewater: A critical review. *Science of the Total Environment*, 612, pp. 561-581.

Selvaraj, M., Hai, A., Banat, F. and Haija, M. A., 2020. Application and prospects of carbon nanostructured materials in water treatment: A review. *Journal of Water Process Engineering*, 33, pp. 100996.

Shakya, A. and Agarwal, T., 2019. Removal of Cr(VI) from water using pineapple peel derived biochars: Adsorption potential and re-usability assessment. *Journal of Molecular Liquids*, 293, pp. 111497.

Sharma, H. B., Panigrahi, S. and Dubey, B. K., 2019. Hydrothermal carbonization of yard waste for solid bio-fuel production: Study on combustion kinetic, energy properties, grindability and flowability of hydrochar. *Waste Management*, 91, pp. 108-119.

Stefaniuk, M., Oleszczuk, P. and Ok, Y. S., 2016. Review on nano zerovalent iron (nZVI): From synthesis to environmental applications. *Chemical Engineering Journal*, 287, pp. 618-632.

Talberg, A., 2009. The basics of biochar. *Science, Technology, Environment, and Resources*, 10(7), p. 582.

Thakur, R., Sharma, G. D., Dwivedi, B. S. and Khatik, S. K., n.d. *Chromium: As a pollutant*. [online] Available at: <<http://www.icontrolpollution.com/article/s/chromium--as-a-polluant-.php?aid=45697>> [Accessed 8 June 2019]

Thines, K. R., Abdullah, E. C., Mubarak, N. M. and Ruthiraan, M., 2017. In-situ polymerization of magnetic biochar e polypyrrole composite: A novel application in supercapacitor. *Biomass and Bioenergy*, 98, pp. 95-111.

Tu, N., Bui, H. V., Trung, D. Q., Duong, A. T., Thuy, D. M., Nguyen, D. H., Nguyen, K. T. and Huy, P. T., 2019. Surface oxygen vacancies of ZnO: A facile fabrication method and their contribution to the photoluminescence. *Journal of Alloys and Compounds*, 791, pp. 722-729.

Ubani, C. A. and Ibrahim, M. A., 2019. Complementary processing methods for ZnO nanoparticles. *Materials Today: Proceedings*, 7, pp. 646-654.

Wahi, R., Zuhaidi, N. F. Q., Yusof, Y., Jamel, J., Kanakaraju, D. and Ngaini, Z., 2017. Chemically treated microwave-derived biochar: An overview. *Biomass and Bioenergy*, 107, pp. 411-421.

Wan, Z., Cho, D. W., Tsang, D. C. W., Li, M., Sun, T. and Verpoort F., 2019. Concurrent adsorption and micro-electrolysis of Cr ( VI ) by nanoscale zerovalent iron/ biochar/ Ca-alginate composite \*. *Environmental Pollution*, 247, pp. 410-420.

Wang, C., Tan, H., Liu, H., Wu, B., Xu, F. and Xu, H., 2019. A nanoscale ferromagnetic oxide coated biochar derived from mushroom waste to rapidly remove Cr(VI) and mechanism study. *Bioresource Technology Reports*, 7, pp. 100253.

Wang, C., Wang, Y. and Herath, H. M. S. K., 2017. Polycyclic aromatic hydrocarbons (PAHs) in biochar – Their formation, occurrence and analysis: A review. *Organic Geochemistry*, 114, pp. 1-11.

Wang, J. and Wang, S., 2019. Preparation, modification and environmental application of biochar: A review. *Journal of Cleaner Production*, 227, pp. 1002–1022.

Wang, S., Zhao, M., Zhou, M., Li, Y. C., Wang, J., Gao, B., Sato, S., Feng, K., Yin, W., Igalavithana, A. D., Oleszczuk, P., Wang, X. and Ok, Y. S., 2019. Biochar-supported nZVI (nZVI/BC) for contaminant removal from soil and water: A critical review. *Journal of Hazardous Materials*, 373, pp. 820-834.

Wang, S., Zhou, Y., Han, S., Wang, N., Yin, W., Yin, X., Gao, B., Wang, X. and Wang, J., 2018. Carboxymethyl cellulose stabilized ZnO/biochar nanocomposites: Enhanced adsorption and inhibited photocatalytic degradation of methylene blue. *Chemosphere*, 197, pp. 20-25.

Wang, Y., Huang, L., Wang, Z., Wang, L., Han, Y., Liu, X. and Ma, T., 2019. Application of Polypyrrole flexible electrode for electrokinetic remediation of Cr(VI)-contaminated soil in a main-auxiliary electrode system. *Chemical Engineering Journal*, 373, pp. 131-139.

Water Environment Partnership in Asia, 2013. *Ambient & emission standards*. [online] Available at: <<http://www.wepa-db.net/policies/law/laos/standards.htm>> [Accessed 8 June 2019]

Wayne, E., 2012. *A brief history of biochar*. [online] Available at: <<http://www.pronatura.org/wp-content/uploads/2012/07/History-of-biochar.pdf>> [Accessed 29 May 2019]

WebElements, 2019. *Chromium: radii of atoms and ions*. [online] Available at: <[https://www.webelements.com/chromium/atom\\_sizes.html](https://www.webelements.com/chromium/atom_sizes.html)> [Accessed 30 June 2019]

Weber, K. and Quicker, P., 2018. Properties of biochar. *Fuel*, 217, pp. 240–261.

Wen, J., Xie, J., Chen, X. and Li, X., 2017. A review on g-C<sub>3</sub>N<sub>4</sub>-based photocatalysts. *Applied Surface Science*, 391, pp. 72-123.

Wilk, M. and Magdziarz, A., 2017. Hydrothermal carbonization, torrefaction and slow pyrolysis of *Miscanthus giganteus*. *Energy*, 140, pp. 1292-1304.

Xiao, G., Wang, Y., Xu, S., Li, P., Yang, C., Jin, Y., Sun, Q. and Su, H., 2019. Superior adsorption performance of graphitic carbon nitride nanosheets for both cationic and anionic heavy metals from wastewater. *Chinese Journal of Chemical Engineering*, 27, pp. 305-313.

- Xiao, R., Wang, J. J., Li, R., Park, J., Meng, C. Y., Zhou, B., Pensky, S. and Zhang, Z., 2018. Enhanced sorption of hexavalent chromium [Cr(VI)] from aqueous solutions by diluted sulfuric acid-assisted MgO-coated biochar composite. *Chemosphere*, 208, pp. 408-416.
- Xu, J., Yin, Y., Tan, Z., Wang, B., Guo, X., Li, X. and Liu, J., 2018. Enhanced removal of Cr(VI) by biochar with Fe as electron shuttles. *Journal of Environmental Sciences*, 78(6), pp. 109-117.
- Yang, X., Liu, L., Zhang, M., Tan, W., Qiu, G. and Zheng, L., 2019. Improved removal capacity of magnetite for Cr(VI) by electrochemical reduction. *Journal of Hazardous Materials*, 374, pp. 26-34.
- Yang, Y., Chen, N., Feng, C., Li, M. and Gao, Y., 2018. Chromium removal using a magnetic corn cob biochar/polypyrrole composite by adsorption combined with reduction: Reaction pathway and contribution degree. *Colloids and Surfaces A*, 556, pp. 201-209.
- Yin, W., Guo, Z., Zhao, C. and Xu, J., 2019. Removal of Cr(VI) from aqueous media by biochar derived from mixture biomass precursors of *Acorus calamus* Linn. and feather waste. *Journal of Analytical and Applied Pyrolysis*, 140, pp. 86-92.
- You, S., Ok, Y. S., Chen, S. S., Tsang, D. C. W., Kwon, E. E., Lee, J. and Wang, C. H., 2017. A critical review on sustainable biochar system through gasification: Energy and environmental applications. *Bioresour. Technol.*, 246, pp. 242-253.
- Yu, H., Zou, W., Chen, J., Chen, H., Yu, Z., Huang, J., Tang, H., Wei, X. and Gao, B., 2019. Biochar amendment improves crop production in problem soils: A review. *Journal of Environmental Management*, 232, pp. 8-21.
- Yu, J., Jiang, C., Guan, Q., Ning, P., Gu, J., Chen, Q., Zhang, J. and Miao, R., 2018. Enhanced removal of Cr(VI) from aqueous solution by supported ZnO nanoparticles on biochar derived from waste water hyacinth. *Chemosphere*, 195, pp. 632-640.
- Yu, T., Abudukeranmu, A., Anniwaer, A., Situmorang, Y. A., Yoshida, A., Hao, X., Kasai, Y., Abudula, A. and Guan, G., 2019. Steam gasification of biochars derived from pruned apple branch with various pyrolysis temperatures. *International Journal of Hydrogen Energy*.
- Yuan, P., Fan, M., Yang, D., He, H., Liu, D., Yuan, A., Zhu, J. and Chen, T., 2009. Montmorillonite-supported magnetite nanoparticles for the removal of hexavalent chromium [Cr(VI)] from aqueous solutions. *Journal of Hazardous Materials*, 166, pp. 821-829.
- Zhang, M., Gao, B., Yao, Y., Xue, Y. and Inyang, M., 2012. Synthesis of porous MgO-biochar nanocomposites for removal of phosphate and nitrate from aqueous solutions. *Chemical Engineering Journal*, 210, pp. 26-32.

Zhang, Q., Song, Y., Amor, K., Huang, W. E., Porcelli, D. and Thompson, I., 2019. Monitoring Cr toxicity and remediation processes - combining a whole-cell bioreporter and Cr isotope techniques. *Water Research*, 153, pp. 295–303.

Zhang, S., Lyu, H., Tang, J., Song, B., Zhen, M. and Liu, X., 2019. A novel biochar supported CMC stabilized nano zero-valent iron composite for hexavalent chromium removal from water. *Chemosphere*, 217, pp. 686-694.

Zhang, X., Fu, W., Yin, Y., Chen, Z., Qiu, R., Simonnot, M. and Wang, X., 2018. Adsorption-reduction removal of Cr(VI) by tobacco petiole pyrolytic biochar: Batch experiment, kinetic and mechanism studies. *Bioresource Technology*, 268, pp. 149-157.

Zhong, D., Zhang, Y., Wang, L., Chen, J., Jiang, Y., Tsang, D. C. W., Zhao, Z., Ren, S., Liu, Z. and Crittenden, J. C., 2018. Mechanistic insights into adsorption and reduction of hexavalent chromium from water using magnetic biochar composite: Key roles of Fe<sub>3</sub>O<sub>4</sub> and persistent free radicals. *Environmental Pollution*, 243, pp. 1302-1309.

Zhu, N., Yan, T., Qiao, J. and Cao, H., 2016. Adsorption of arsenic, phosphorus and chromium by bismuth impregnated biochar: Adsorption mechanism and depleted adsorbent utilization. *Chemosphere*, 164, pp. 32-40.

Zhu, X., Li, Y. and Wang, X., 2019. Machine learning prediction of biochar yield and carbon contents in biochar based on biomass characteristics and pyrolysis conditions. *Bioresource Technology*, 288, p. 121527.

Zhu, Y., Li, H., Zhang, G., Meng, F., Li, L. and Wu, S., 2018. Removal of hexavalent chromium from aqueous solution by different surface-modified biochars: Acid washing, nanoscale zero-valent iron and ferric iron loading. *Bioresource Technology*, 261, pp. 142-150.